PROGRAMMABLE, ISOTHERMAL DISASSEMBLY OF DNA-LINKED COLLOIDAL PARTICLES

A Dissertation
Presented to
The Academic Faculty

Christopher Kirby Tison

In Partial Fulfillment
Of the Requirements for the Degree
Doctor of Philosophy in Materials Science & Engineering

Georgia Institute of Technology

May, 2009

PROGRAMMABLE, ISOTHERMAL DISASSEMBLY OF DNA-LINKED COLLOIDAL PARTICLES

Approved by:

Dr. Valeria Milam, Advisor
School of Materials Science & Engineering
Georgia Institute of Technology

Dr. Todd McDevitt
Department of Biomedical Engineering
Georgia Institute of Technology

Dr. Barbara Boyan
Department of Biomedical Engineering
Georgia Institute of Technology

Dr. Ken Sandhage
School of Materials Science & Engineering
Georgia Institute of Technology

Dr. Mo Li
School of Materials Science & Engineering
Georgia Institute of Technology

Date Approved: March 26, 2009

“We wish to suggest a structure for the salt of deoxyribose nucleic acid (D.N.A.). This structure has novel features which are of considerable biological interest.”

- J.D. Watson, F.H. Crick

April 25, 1953

"The essence of science lies not in discovering facts, but in discovering new ways of thinking about them."

- W.L. Bragg

Elizabeth.

This thesis is dedicated to you and your support. For your time and energy and love that have pulled me through 5 years of stresses and discoveries. It has been one of the true joys of my life to experience these years with you, and I have neither the words nor the space to thank you for the rock you have been to me. You are my center, when I spin away, and I look forward to a life of returning home to you.

I thank you and love you from the bottom of my heart.

ACKNOWLEDGEMENTS

This thesis has been a collective effort, and I am honored to think of all that have had a part in it. My thanks go first to my advisor, Dr. Valeria Milam, who has gone far beyond her duty to make this project proceed efficiently. She has served as a true mentor, and I appreciate all her time and encouragement. I was the first Ph.D. student to join her lab, and I am thrilled to be the first out – I consider myself lucky to have experienced this adventure with her. I'm also tremendously grateful for the other students within the MSE department that have made this an enjoyable experience – especially Bryan and James. Further, I've had the opportunity to mentor several fantastic undergraduate students, and I am so grateful for all they have taught me about research and mentorship. I lastly thank my committee for their wisdom, time, and kind words. I've spent most of the last decade at Georgia Tech receiving a B.S. and Ph.D., and I am honored to have had the friends, classmates, colleagues and advisors that I have had. This Ph.D. comes from a special commitment that Tech has made to each incoming student – I am grateful to have been one of them.

I was fortunate to have a wonderful childhood, and I place much of the blame for the next 200 or so pages on having family that emphasized knowledge, exploration, and a certain degree of humility. Without the love I had surrounding me throughout my life from family and friends, this thesis would not have been possible. I was always taught that the reward for doing good in school was the chance to do better, to learn more, to explore further – I hope my life will continue in that vein.

TABLE OF CONTENTS

LIST OF TABLES

LIST OF FIGURES

CHAPTER 1

CHAPTER 2

CHAPTER 3

CHAPTER 4

CHAPTER 5

CHAPTER 6

CHAPTER 7

CHAPTER 8

APPENDIX

LIST OF ABBREVIATIONS

DLVO	Derjaguin, Landau, Verwey, Overbeek
vdW	van der Waals
k_B	Boltzmann's constant
PEG	poly(ethylene glycol)
DNA	deoxyribonucleic acid
ssDNA	single stranded DNA
dsDNA	double stranded DNA
A	adenine
T	thymine
C	cytosine
G	guanine
DNase	deoxyribonuclease
RNase	ribonuclease
FCC	face-centered cubic
BCC	body-centered cubic
PEO	poly(ethylene oxide)
TWEEN-20	polyoxyethylenesorbitan monolaurate
FRET	förster resonance energy transfer
DDR	DNA displacement reaction
FSC	forward scattering counts
SSC	side scattering counts
FITC	fluorescein isothiocyanate
MESF	molecules of equivalent soluble fluorophore
HPLC	high performance liquid chromatography
TE or Tris-EDTA	ethylenediaminetetraacetic acid (at pH 7.4 or 8.0)
EDAC	ethyl-3-[3-dimethylaminopropyl]carbodiimide hydrochloride
HCB	house coupling buffer (50 mM MES, 0.05 % Pro-Clin 300, pH 5.2 with 4 M NaOH, NanoPure water)
PBS	phosphate buffered saline
PBS/TWEEN	phosphated buffered saline solution with 0.05% Tween-20
C*	critical concentration for fluid to fluid + aggregate transition
C**	critical concentration for fluid + aggregate to aggregate transition
NEB2	New Englands Biolabs buffer 2 (50 mM NaCl, 10 mM Tris-HCL, 10 mM MgCl2, 1mM dithiothreitol)
MGI	mean gray intensity
SEM	scanning electron microscopy
DLS	dynamic light scattering

SUMMARY

This thesis project investigates using competitive hybridization partners to induce the isothermal redispersion of DNA-linked structures. The overarching goal is to ultimately implement a multiparticle drug delivery vehicle that possesses an intrinsic release mechanism to break apart the particle assembly at the targeted tissue. DNA has previously been used as a reversible assembly tool in colloidal science, but high temperatures are required to melt (and therefore reverse) the structure; our goal of using DNA in biomaterials applications renders melting suboptimal as drug delivery commonly occurs under isothermal conditions. In this work, DNA is first used to assemble a particle-based drug delivery vehicle. Subsequent competitive hybridization with longer secondary hybridization partners or targets is then used to disassemble or redisperse the particles. It was found that altering competitive strand concentration and length can tune the kinetics and extent of competitive hybridization. Further, control over DNA-mediated disassembly can be tuned by titrating the number of DNA linkages holding colloidal particle assemblies together. To the best of our knowledge, this work presents the first report of *programmable*, isothermal disassembly of colloidal assemblies.

This thesis is divided into eight chapters as follows. Chapter 1 will serve to highlight past work on DNA as a materials assembly tool, as well as providing a brief overview of colloidal particles as materials building blocks. Lastly, an extensive outline is provided showing the variety of DNA-based materials technologies that have been developed in the past decade. Chapter 2 will detail results investigating "primary" hybridization between probe strands coupled to microspheres and either soluble or

immobilized targets. Chapter 3 will expand on using primary duplexes to drive DNA-mediated colloidal aggregation, including various techniques we have adopted or developed to minimize the number of DNA-linkages by including diluent strands. Chapter 4 presents a separate approach for modifying surface-immobilized diluent strands using a restriction endonuclease digest. In addition to providing a way to control surface probe presentation, these studies provide some new insights into the nature of the microenvironment at the DNA-particle surface. Chapter 5 outlines the selection and characterization of secondary target strands that displace the original or primary targets. This chapter covers the investigation of the effects of base length differences on displacement of soluble primary targets by longer secondary targets. These studies allow for selection of 1) primary targets with sufficient hybridization avidity to drive DNA-mediated assembly to completion and 2) a secondary target that can effectively displace the primary target to drive disassembly to completion. In Chapter 6 we investigate the kinetics of soluble target displacement in-depth, analyzing the effects of target length and concentration. The data for time-dependent displacement of soluble targets is fit using a first order equation to derive experimental replacement rates. In Chapter 7 the kinetics of nanoparticle release from colloidal "satellite" assemblies through competitive hybridization events are investigated as a function of secondary target concentration. Unsurprisingly, the half-life of the DNA-linked colloidal assemblies can be tuned through choice in the target concentration. Finally, Chapter 8 will outline a new direction for developing colloidal carriers that can be cued to shed a protective stealth coating through competitive hybridization events.

CHAPTER 1

Literature Review

The use of DNA as a programmable assembly tool has been widely investigated for the last decade. Since Chad Mirkin and Paul Alivisatos' pioneering work utilizing complementary DNA sequences to aggregate nanometer-sized gold particles, DNA has been used to assemble a wide variety of colloidal materials ranging from quantum dots to giant lipid vesicles. The great interest in DNA as a materials assembly tool revolves around the unique and customizable properties of the DNA macromolecule itself – specifically the ability to tailor complementarity, melting temperature, length and end-functionalization with great specificity. This literature review will first outline fundamental aspects of colloidal science and pair-wise colloidal interactions that must be considered in directing colloidal assembly via DNA hybridization. The properties of DNA as a biological macromolecule will then be investigated, followed by a detailed description of DNA-mediated assembly. Finally, enzymatic processing of DNA-linked structures and competitive hybridization reactions will be reviewed.

1.1 - Colloidal Particles, Interactions and Aggregation

1.1.1 - Colloidal Particles and Size Regimes

A colloidal particle is typically characterized as possessing a surface area significantly greater than its volume, such that surface-based phenomena are dominant in controlling the behavior and interactions *(1)*. This typically implies that the particle

possesses at least one dimension between 10^{-3} and 1 μm. Not all dimensions must fit in this regime, and the upper limit is loosely defined, as approximately 1.0 μm. Colloids are available in a variety of shapes, compositions, and sizes. The similarity in their behavior is attributed to surface effects. Colloids have many merits as "building blocks" for a variety of different materials since both inorganic and organic-based colloids are available. The clay-water system was the first widely studied colloidal suspension, and was of great interest for ceramic processing *(2)*. In the early 1990's, Lange proposed a new paradigm in ceramic processing, utilizing colloidal particles to induce a "clay-like" response *(3)*. His research proposed using size, morphology, etc. to tailor interparticle control. Through careful control of interparticle interactions, colloidal suspensions can exist in aggregated, weakly aggregated, or fluid-like stable suspension phases *(4)*. Many characterization tools are available for the study of colloidal suspensions and assemblies, including fluorescence microscopy, confocal microscopy, rheology, flow cytometry and spectroscopy. These techniques allow researchers to analyze colloidal structures within suspensions, and some such as flow cytometry can even investigate the presence of surface-immobilized functionalities on the particle surfaces *(5)*.

1.1.2 - The Importance of the Colloid Surface

There are two important consequences of the colloidal particle size range: one, colloidal materials have enormous surface areas and surface energies and two, the properties of the colloidal materials are not always identical to those of their bulk material *(1)*. Therefore, in developing a system for the controlled stability or aggregation of colloidal particles, it is mandatory that a level of surface control be obtained. Colloidal structures, aggregate formation, and stability depend strongly on pairwise interactions

between particles *(2)*. These pairwise interactions are non-specific forces that lack directionality. Rather, dipole attractions and electrostatic repulsions are continuously acting between all particles. These non-specific interactions have traditionally been the central focus of colloidal scientists, who hope to modulate the attractions and repulsions to generate suspensions that are either stabilized or nonspecifically aggregated by these forces *(1, 6-9)*. Colloidal stability is dictated by the total interparticle potential energy, and is largely controlled by the van der Waals (vdW) attractions and electrostatic repulsions accounted for in Derjaguin, Landau, Verwey and Overbeek (DLVO) theory *(4)*. This pioneering theory predicts the stability of colloidal particles in polar liquids, and has been upheld by numerous experimental studies that followed.

1.1.3 - Nonspecific Colloidal Interactions

The range and degree of net attractive or repulsive colloidal interactions depend on the chemical composition, presence of surface functionalities (e.g., charged groups, adsorbed or grafted macromolecules, etc.) and solution conditions. In the 1940's, two groups simultaneously developed what is now known as the DLVO theory, which is used to calculate interaction potentials between pairs of bare, homogeneous, spherical particles based on the attractive vdW and repulsive electrostatic forces *(4)*:

$$V_{total}(r) = V_{vdW}(r) + V_{elec}(r) \tag{1}$$

where r is the separation distance, V_{total} is the total interaction potential, V_{vdW} is the attractive van der Waals potential, and V_{elec} is the repulsive electrostatic interaction potential between particles. This equation relies on the Derjaguin approximation that

geometrically relates the interaction between two spheres to that between two plates. At small separation distances, the vdW attractive interactions can easily dominate. Thus, including surface charge groups can provide the necessary long-range repulsive interactions to stabilize suspensions and prevent aggregation (due to vdW interactions). Figure 1.1.1 shows a representative schematic illustrating the DLVO interaction potential energy curves and their effect on particle attraction or repulsion.

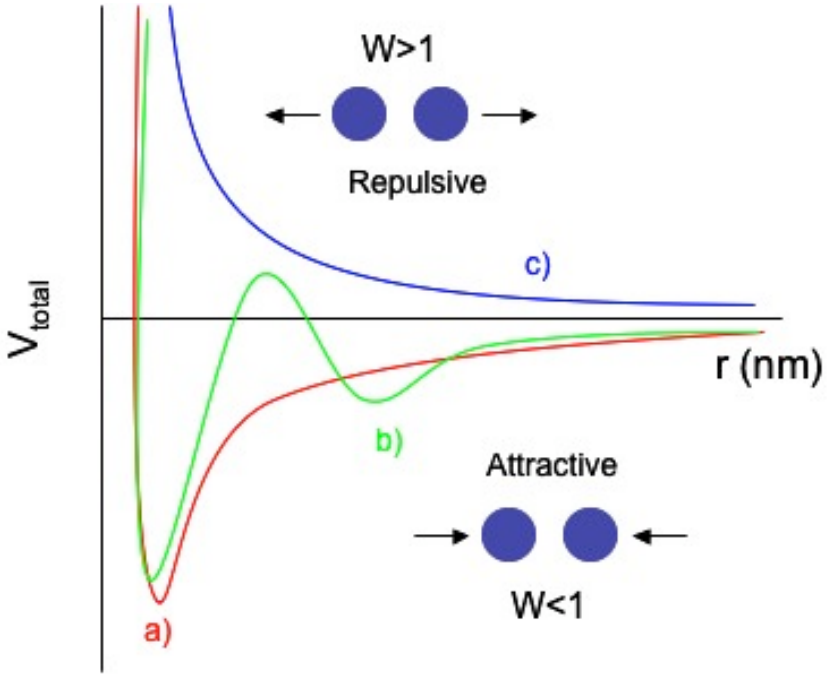

Figure 1.1.1: Schematic of DLVO interaction potential energy curves with a) large primary attractive well, resulting in irreversibly aggregated particles, b) secondary attractive well allows for weaker thus, reversible attractions between particles, and c) completely repulsive interaction potential, resulting in stable or dispersed particles. Here, W refers to the stability ratio in which aggregation is only favored when W is less than 1. (Modified image from *(1)*)

Van der Waals attractions are the dominant contributor to non-specific attractive interactions, and arise from dipole-dipole interactions in which there is a separation of positive and negative charge. The electric field that is created by a dipole can attract or repel a neighboring dipole depending on its orientation; because dipoles tend to align themselves, these dipole interactions lead to a net attractive force. There are three relevant vdW attractions: the London dispersion force, the Debye force, and the Keesom force. The London dispersion force arises from fluctuating dipoles due to electron cloud movement in molecules, when nearby dipoles "communicate" with one another, the dipoles correlate orientation and produce a net attractive force. The Keesom forces are similar but arise from permanent dipoles, not fluctuations. Finally, Debye forces arise between permanent and fluctuating dipoles that again align to produce a net attractive force. In most all cases, the London dispersion force is dominant, and the dispersion attractive interaction is proportional to the polarizabilities of the two molecules:

$$V_{vdW} \propto -\frac{\alpha_1 \alpha_2}{r^6} \tag{2}$$

where α_1 and α_2 are the polarizabilities and always positive. This results in an attractive interaction that is always negative and falls off quite steeply with the sixth power of the separation distance.

Electrostatic repulsive interactions are present in all materials possessing like charges in polar solvents that contain ions from salt additions. In colloidal suspensions, ion concentrations near a charged surface deviate from bulk values, and decay exponentially as the distance from the particle surface is increased with a decay "length"

of κ^{-1}. This scale is known as the Debye length and corresponds to the distance over which electrostatic forces influence particle behavior. The value of the Debye length defined by the Guoy-Chapman diffuse double layer model, which for a 1:1 electrolyte (e.g., NaCl) is:

$$\kappa^{-1} = \frac{0.304}{\sqrt{[NaCl]}} \quad \text{(nm)} \tag{3}$$

This reveals that the thickness of the double layer is highly dependent upon the electrolyte concentration of the suspension. Changing the ionic conditions to modulate electrostatic forces can therefore stabilize colloidal particles *(10)*.

The stability of colloidal suspensions can be described using the kinetic stability ratio, *W*, which is defined as:

$$W_{ij} = \frac{K_{rapid}}{K_{measured}} \tag{4}$$

where *K* is the rate constant of diffusion, K_{rapid} specifies the calculated aggregation rate based purely upon particle diffusion with no energy barriers present, and $K_{measured}$ is the rate constant of aggregation determined experimentally *(2)*. A stability ratio (*W*) of unity implies diffusion limited aggregation in which particle stick upon first contact, whereas a stability ratio of greater than one indicates some measures of particle stability that prevents aggregation upon particle-particle collisions. With knowledge of the interaction potential, the theoretical stability ratio is calculated as:

$$W = \exp\left(\frac{V_{\max}/k_B T}{2\kappa a}\right) \quad (5)$$

where V_{max} is the maximum repulsive barrier height, k_B the Boltzman constant, and T is the temperature in Kelvin. The stability ratio is exponentially dependent upon the repulsive energy and linearly dependent upon the electrostatic double layer thickness, κa^{-1}. This equation allows one to use the interparticle interaction potential to determine the stability of a particle suspension.

1.1.4 - Colloidal Aggregation via Nonspecific Interactions

1.1.4.1 Other Nonspecific Forces

By tuning nonspecific forces that control interparticle interactions one can modify the phase behavior of colloidal suspensions. These nonspecific interactions include the above-mentioned van der Waals attractive and electrostatic repulsion interactions *(11)*. In addition, steric, electrosteric, and depletion interactions can be introduced by adding, for example, polymeric chains or macromolecules to suspensions *(8, 12)*. Steric forces provide an alternative route for the stabilization of colloidal particles *(13)*. Here, adsorbed macromolecules are used to induce a repulsion based upon entropic interactions of the adsorbed layers with one another (in terms of steric, or space-dependent interference effects). These repulsions are based on adsorbed layers (adlayers) preventing particles from closely approaching one another and falling into attractive potential wells due to vdW attractions. A variety of polymeric adlayers have been investigated, and stability depends on the solvent quality, molecular architecture, number of anchoring groups, the density of adsorbed polymer and the volume fraction of colloidal particles *(2)*.

Electrosteric stabilization also occurs due to the introduction of adlayers on a particle surface, though for this case, the adlayers must possess charged groups *(8)*. This charged adlayer provides both steric stabilization due to adlayer thickness, and electrostatic stabilization due to the presence of repulsive charges on the particle surface. The design of an electrosterically stabilized colloidal system often requires the adsorbed polyelectrolyte be oppositely charged to the particle surface, favoring increased adsorption. The surface density of the polyelectrolyte plays a large role in determining the behavior of the system. At lower adsorbed amounts, "patchy" areas of charge exist, often leading to particle aggregation. Typically, increasing the density of the polyelectrolyte results in more stable colloidal suspensions.

Finally, depletion forces can be introduced to promote either stabilization or aggregation of the colloidal particles. Depletion forces arise between larger colloidal particles suspended with non-adsorbing smaller species (depletants) such as polymers, polyelectrolytes, or smaller colloidal particles *(12)*. Depletion occurs when a negative depletant concentration exists near the larger, primary particle surfaces. This concentration gradient of the smaller molecules induces a depletion layer thickness on the order of the depletant diameter. At low depletant concentrations, aggregation of the larger particles results. At higher concentrations, however, this concentration gradient is altered resulting in stable colloidal suspensions. This behavior has been confirmed by several studies that revealed depletion forces depend strongly on the initial stability of the colloidal suspension as well as the size and concentration of the depletant species *(2, 14, 15)*.

1.1.4.2 Controlled Aggregation via Nonspecific Interactions

Multiple groups have investigated the controlled stabilization or aggregation behavior of colloidal systems using nonspecific interactions. A variety of different polymers and polyelectrolytes have been adsorbed to particle surfaces to induce steric or electrosteric stabilization, among these poly (ethylene glycol) (PEG) *(16)* and even DNA *(17, 18)*, which can be used as a highly charged adlayer to provide electrosteric stability. Kim et al. *(16)* have developed a swelling-based method of incorporating PEG into polystyrene microspheres, which provides exceptional stability, as the adlayer is not adsorbed to the surface, but rather impregnated within the polystyrene particle matrix. Gilchrist et al. *(19)* have investigated the phase behavior of strongly attractive microsphere-nanoparticle mixtures by mixing silica microspheres with polystyrene nanoparticles. The binary suspension is tuned to cause strong repulsion between like particles, and strong attraction between opposing particles. By modifying the nanoparticle concentration in solution, they create a system that is either highly flocculated at low nanoparticle concentrations due to bridging, or restabilized as the larger silica particles are coated with a layer of the nanoparticles. By sedimenting the aggregates with gravity, they control the range in morphologies of the colloidal aggregates from compact particle arrangements to highly fractal colloidal gels. Sedimentation has also been used to create aggregates with well-defined shapes and sizes. Yin et al. *(20)* allowed monodisperse colloidal spheres to sediment on "holes" in a thin film of photoresist that were created by lithography. Depending on the hole size and particle size, a variety of single or double layer clusters were created, including triangles, squares, pentagons, octahedrons and bi-square pyramids. This aggregation process was extremely well controlled, and was

primarily governed by the hole size to particle size ratio. Controlling the hierarchical assembly, however, of these small building blocks was left unexplained, and thus challenges remain in using nonspecific interaction to finely control the "assembly" of colloidal particles with this approach.

1.1.5 - Colloidal Aggregation via Specific Interactions

Though the above examples indicate the wide-variety of non-specific interactions that can be controlled for colloidal aggregation or stability, there is significant interest in introducing programmable assembly of colloidal particles into the arena. Using particular pairs of biological macromolecules called receptors and ligands provides the ideal pathway. Since the early 1990's, multiple groups have investigated the use of specificity in programmed colloidal assembly, including the use of lock-and-key interactions found in a variety of biological macromolecules such as proteins *(21)*. In these cases, various ligand-receptor interactions are exploited to program aggregation between particles with "complementary" functionalities on the surface. These lock-and-key interactions include antibody-antigen interactions, carbohydrate-selectin interactions, and biotin-avidin binding. Though these lock-and-key interactions provide extreme specificity in their interactions, they possess only fixed affinity values.

Shenton et al. developed a biomolecular-derived route to self-assembly using surface attached antibodies *(22)*. They attached IgE or IgG antibodies to one population of nanoparticles, while immobilizing the matching antigen to another nanoparticle population. Particle aggregation was observed, while particles remained dispersed in control experiments. It was determined that one antibody-antigen interaction is sufficient to cause the cross-linking required for particle aggregation. Similar work by Connolly

utilized the biotin-avidin interaction for the programmed assembly of gold nanoparticles *(23)*. In this case, biotin immobilized nanoparticles were incubated with free streptavidin protein. Since streptavidin possesses four binding sites for biotin, it acted as a cross-linker to induce particle aggregation. They found that directed nanoparticle aggregation occurred, and proposed that biotin analogues with a wide range of rate and equilibrium constants could pave the way for other novel streptavidin-linked systems. Finally, carbohydrate-selectin interactions have been used to mediate formation of binary colloidal structures *(21)*. By tuning the ratio of small, selectin-immobilized particles to large, sialyl-Lewis^x (tetrasaccharide carbohydrate) particles, a variety of structures were formed including colloidal micelles, colloidal clusters, rings and elongated chains. The use of selectins that exhibit low affinity binding poses the promise of reversible interactions, or the ability of fractal structures to anneal, as dissociation times for the carbohydrate-selectin bond are on the matter of seconds. Further, the specificity of this system allows excess particles to be removed from the aggregate, and therefore from the suspension itself. Though the biotin-avidin and selectin systems reveal the ability to tune the interaction energy across a wide-range of rate constants, each ligand-receptor pair possesses a fixed affinity value. In order to change the overall avidity resulting from the collective binding events between colloidal particle surfaces, an entirely different protein system is required, which will also require a separate immobilization procedure, etc. For these reasons, DNA offers a promising alternative as will be shown below. DNA can be immobilized to surfaces through a variety of protocols, and also offers the ability to change the interaction energy by altering sequence characteristics such as length or base

composition. Thus, one can retain the specificity of the above systems, while allowing for tunability of the interaction energy.

1.2 - Deoxyribonucleic Acid as a Biological Macromolecule

1.2.1 - Deoxyribonucleic Acid and its Properties

Oligonucleotides are polymeric chains composed of a series of nucleotides as their repeat units *(24)*. Each nucleotide consists of an alternating deoxyribose sugar and phosphate along the backbone and a base side group that is adenine (A), guanine (G), cytosine (C), or thymine (T). Figure 1.2.1 illustrates a hybridized DNA duplex and the specific hydrogen bonding that occurs to cause duplex formation.

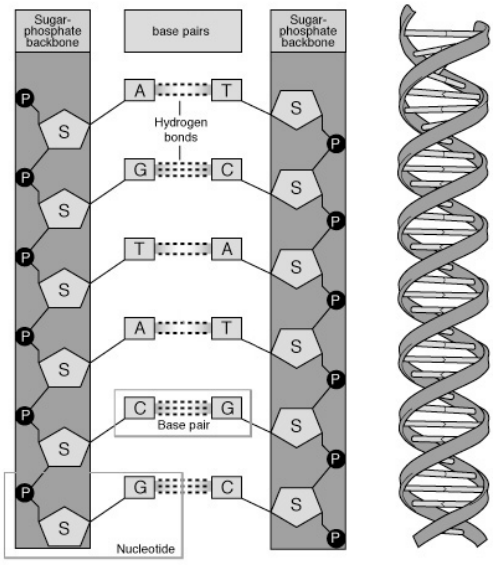

Figure 1.2.1 – Schematic of deoxyribose nucleic acid backbone and helical structure *(25)*.

In order for single oligonucleotide strands (single stranded DNA, or ssDNA) to link or hybridize to form a double-stranded DNA helical coil or duplex, pairs of complementary bases must sequentially line up, so that adenine binds with thymine via two hydrogen bonds and cytosine binds with guanine via three hydrogen bonds. This specific pairing of matching, or complementary, bases is known as Watson-Crick base pairing (Figure 1.2.2), and is the basis for the dissemination of genetic traits from one cell generation to the next.

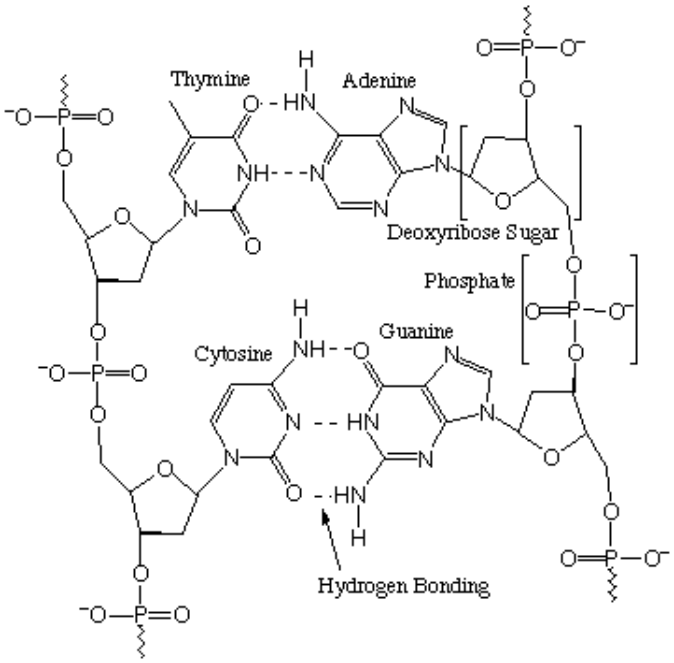

Figure 1.2.2 - Chemical structure and hydrogen bonding of all four nucleotides in Watson Crick base pairing. Deoxyribose sugar and phosphate backbone are shown on each side and labeled on the right *(26)*.

DNA has a miniscule size and regular structural characteristics on the nanometer length scale that makes it particularly promising for the programmed assembly of colloidal particles. It has a diameter of 18 Å and a structural repeat (single helical turn) of 3.4 nm. In 1953, Watson and Crick discovered the double helix structure of DNA, which is generally in a right-handed coil formation. Two first-order effects cause this helical coiling: exclusion of the hydrophobic bases from water, and the geometry of the sugar-phosphate bond as compared to the base length. Since bases must be separated by 3.3 Å while phosphate residues are 6 Å apart, the adoption of a helical coil is the thermodynamically preferred position that doesn't force neighboring atoms into close contact (such as a skewed ladder orientation would). There are several second order effects that also affect the type of helical coil that forms, as well as the relationships between adjacent bases. These effects include propeller twist to exclude as much of the base from the water environment as possible, base pair stacking that depends on the order of the bases, and small motions of base-pairs which accumulate to modulate the helical structure. In addition, B-form DNA (the traditional, right-hand duplex orientation that exists under physiological conditions) is an extensible molecule and capable of stretching up to 1.7 times its native state *(27, 28)*. This behavior allows DNA to bind between particle surfaces that are separated by varying distances due to particle curvature. It also indicates the robust nature of the hybridized duplex structure.

Other forms of DNA hybridization exist beyond the typical Watson Crick base-pairing. At low pH, Hoogsteen base pairing can occur where the purines (A and G) are rotated 180° about the sugar bond, and hydrogen bonding occurs on deprotonated nitrogen. Hoogsteen base pairing is less stable than the Watson-Crick counterpart, as both

the A-T and C-G bonds have only 2 hydrogen bonds present. Since the deprotonation of the nitrogen only occurs below pH 5, these are not duplex structures that are found under *in vivo* conditions. However, Hoogsteen base pairing can be important when DNA triplexes are formed, or in complexes of DNA with anticancer drugs *(24)*.

In addition to the specific coiling of double-stranded oligonucleotide strands, one must also consider the possibility of single-stranded oligonucleotides forming self-loops or hairpins via intrastrand hybridization. This phenomenon whereby a single stranded oligonucleotide folds back upon itself and undergoes self-hybridization can compromise the efficiency of *inter*strand hybridization and is thus an important consideration when selecting a sequence for particle assembly. In order to select a strand that does not undergo self-hybridization at a specific temperature, melting analysis is performed; this is discussed in the following section.

1.2.2 - Thermodynamics of DNA in Solution

1.2.2.1 - Duplex Melting Behavior

The melting temperature, T_m, of oligonucleotide duplexes plays an important role in understanding the hybridization of single stranded oligonucleotides to form double stranded duplexes. The melting temperature is calculated as the temperature at which half of the duplexes have been dissociated. Thus, T_m is a measure of the thermal stability of the helix itself against dissociation into single strands, and therefore represents the affinity that the two complementary strands have for one another. The value of the melting temperature of a DNA duplex depends on the number of base pair matches, the sequence composition (i.e., percentage of G/C vs. A/T), strand concentration, and the ionic strength of the solution *(29, 30)*. Thus, the melting temperature can be adjusted by

varying the ratio of G/C to A/T base pairs, as G/C base pairs possess three hydrogen bonds compared to two for the A/T case. The longer the strand, the higher the melting temperature is as well (for similar ratios of G/C to A/T). The higher the melting temperature for a strand sequence, the higher the temperature required to break sufficient hydrogen bonds between matching bases to cause dissociation of the helical structure into ssDNA. Thermodynamic analysis of sequences allows for calculations of theoretical melting temperatures using nearest neighbor considerations *(31)*. Here, Gibbs free energy values for all 10 possible nearest neighbors are used to calculated the total Gibbs free energy for a sequence:

$$\Delta G^{\circ}(total) = \Sigma n_i \Delta G_i(i) + \Delta G^{\circ}_{initG-C} + \Delta G^{\circ}_{initA-T} + \Delta G^{\circ}_{sym} \quad (4)$$

where $\Delta G°(i)$ is the standard free-energy changes for the 10 possible nearest neighbors, n_i, is the number of occurrences of each nearest neighbor, $\Delta G°_{init}$ are the initiation parameters for the sequence end pairs, and $\Delta G°_{sym}$ is a term for self-complementary sequences (this is equivalent to 0 for all non-self-complementary sequences). Appendix A shows the results of nearest-neighbor free energy analysis for the 10 base-long duplex formed in our studies. Ionic strength dependence can also be included, where salt concentration effects are greatly dependent on oligonucleotide length (because of the increasing number of negatively charged phosphate groups which are shielded by counterions) but not on sequence.

1.2.2.2 - Single Stranded DNA Self Melt Behavior

The self-melt temperature (T_m^{self}) is an indicator of the stability of ssDNA in solution against hairpin or loop formation. Because DNA hybridizes in an antiparallel fashion, it is possible for ssDNA that is long enough to fold back upon itself and have complementary segments hybridize. This phenomenon can compromise the efficiency of interstrand hybridization and thus is an important consideration when selecting a sequence where fidelity of hybridization is important. Nadrian Seeman has performed many studies using sequences with low self-melt temperatures in order to build complicated DNA constructs (without particles) as discussed in section 1.3.1 *(32-37)*. Self-melt temperatures can be calculated using programs such as Michael Zuker's Mfold web-server *(38)* and Integrated DNA Technologies OligoAnalyzer *(39)*, which utilize thermodynamic parameters to calculate the temperature at which self-folding can occur. In general, strands with a self melt temperature below 0 °C are desired to avoid hairpin formation at room temperature or 37 °C.

1.2.3 – Biological Function of DNA

Watson and Crick formally proposed the double helical structure formed of hybridized complementary strands in 1953 *(40)*. They end their one-page report stating, "it has not escaped our notice that the specific pairing we have postulated immediately suggests a possible copying mechanism for the genetic materials." *(40)* In the last 6 decades, the work built on this premise is astounding – resulting in the first fully sequenced human genome in 2001 *(41)*. DNA serves not only as the carrier of genetic information, but also as the director of multiple systems which control the replication, transmission, and silencing of cellular behavior *(42)*. DNA is packaged in the cell's

nucleus in tightly wound packages known as "nucleosomes." These nucleosomes are composed of extremely long sequences of DNA wound around histones; a protein that can very tightly pack methylated DNA.

There are also multiple enzymes capable of acting on DNA *in vivo*, which play an important role in both the copying and transmission of information within the cell, as well as the destruction of foreign or viral DNA. Restriction endonucleases, which are present in a variety of bacteria, are capable of cleaving specific double stranded sequences to prevent contamination of host DNA *(43)*. These specific double stranded sequences are known as recognition sequences, and hundreds of different endonucleases with defined recognition sequences are known to exist. Further, the use of restriction enzymes in biotechnology is a common and powerful tool, used for inserting specific sequences into plasmids, performing DNA sequencing, and manipulating DNA length for other purposes.

Deoxyribonucleases such as DNase I and DNase II are found in the human body, and can digest single and double stranded DNA that invades the body. There are also dozens of ribonucleases (RNase), which act to clip and digest any foreign RNA *in vivo*. These enzymes play important roles in replication and defense from foreign oligonucleotides *(42)*.

1.2.4 - Summary of DNA as a Macromolecule

The properties of DNA described above reveal five important points for the selection of DNA as a colloidal assembly tool, laid-out elegantly by Gothelf and LaBean and summarized here *(44)*:

i. DNA is the biological building block with the highest information content.
ii. DNA is constructed with only four, almost identical, building blocks.
iii. DNA's self-assembly behavior is far more predictable than other biological macromolecules.
iv. Microgram quantities of DNA can be easily and inexpensively obtained.
v. A diverse infrastructure exists for the biotechnological manipulation of DNA.

Together, these characteristics reveal that DNA is a powerful and promising tool for the controlled manipulation of material structures. The use of DNA as an assembly tool will be discussed below.

1.3 - DNA as an Assembly Tool

1.3.1 - DNA for Self-Assembling Novel Structures

Nadrian Seeman pioneered the use of DNA alone to drive assembly of 2D and 3D objects. By carefully selecting specific "designer" sequences, Seeman was able to drive the assembly of DNA into novel duplex-based forms *(32-34, 36)* such as tiles *(37)*, junctions *(33)*, knots *(35)*, branched junctions *(36)*, and so on. His work also pioneered the idea of using algorithms to design sequences with low self-melt temperatures and negligible affinity to non-complementary sequences. Recently, groups have used similar

techniques to design dynamic and moveable DNA structures, and even DNA complexes that form more intricate three-dimensional structures in solution. Hanadi Sleiman has designed three-dimensional DNA complexes that are capable of responding to the presence of longer target strands within solution *(45, 46)*, creating a set of dynamic three-dimensional structures within solution. Several groups have also investigated the use of DNA as a tool for computation *(47, 48)*. In those cases, DNA sequences are used to carry "information," though as representative bits, not genetic code. Frutos et al. *(47)* develop a word-design strategy in which 16 base oligonucleotides possess a 4 base "word" specific to the sequence, an 8 base hybridizing segment which is of equivalent thermodynamics for each sequence, and a 4 base mismatch with each of the other 108 "words." This strategy allows selection at a surface with extreme specificity, allowing the controlled presentation of 108 "words." Enzymatic manipulation on non-marked strands allows for further code control and signal processing.

Combined, research in soluble DNA assembly has shown that great specificity exists with the DNA molecule. By manipulating base-pairing schemes, a variety of three-dimensional structures can be created, many of which are dynamic and responsive to the solution environment. The use of this specificity and control in conjunction with materials assembly is discussed next.

1.3.2 - DNA as an Assembly Tool for Colloidal Particles

In 1996, Chad Mirkin *(49)* and Paul Alivisatos *(50)* simultaneously demonstrated the use of DNA as a programmable tool for the controlled aggregation of gold nanoparticles. Alivisatos designed long, linear segments of single stranded oligonucleotides capable of hybridizing to short, target segments immobilized on

colloidal gold nanoparticles. Upon hybridization, linear chains of particles with controlled spacing were formed. Mirkin utilized a different approach, relying on short linker molecules to hybridize to surface immobilized probes with eight base-pair complementary segments to the linker as seen in Figure 1.3.1. Upon addition of the linker oligonucleotide (a duplex with two – eight base-pair sticky ends), hybridization occurs and particle aggregation is observed. Because gold nanoparticles were used, a red to blue color shift due to plasmon resonance changes was observed, indicating specific hybridization and particle aggregation. Controls indicated that when a non-complementary linker sequences was added, the particles remained in a stable suspension, as the non-complementary surface immobilized targets did not undergo hybridization. Since this revolution in controlled colloidal assembly, dozens of groups have begun research on the use and control of DNA as a materials assembly tool. Over time, a "toolbox" of techniques and manipulation pathways has been developed which allow greater specificity and even manipulation of the strands on particle surfaces.

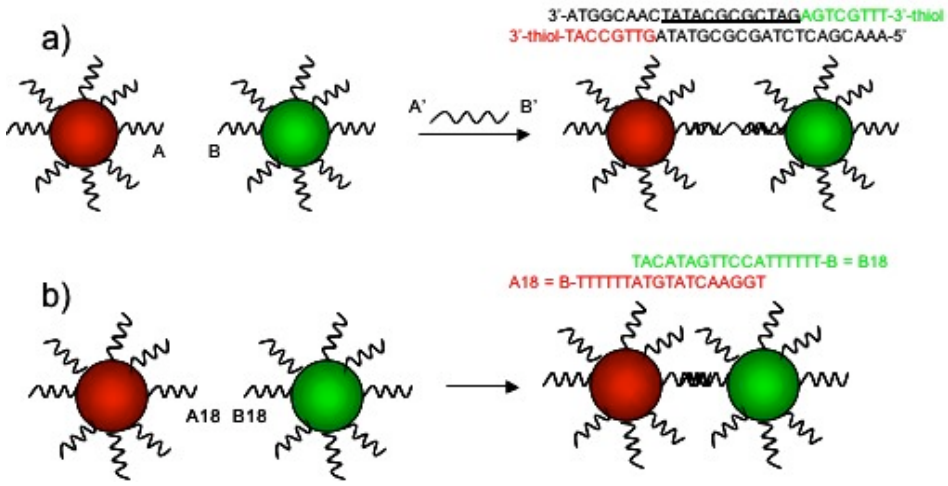

Figure 1.3.1 - DNA assembly schemes of a) Mirkin and b) Milam. Mirkin's approach involves a third linking strand with two sticky ends complementary to the surface-immobilized strands. Milam's approach involves immobilizing complementary oligonucleotide strands on two populations of colloidal particles (Adapted from *(49)* and *(51)*).

A wide variety of materials have now been assembled using specific DNA hybridization including nanoparticles *(49, 50)*, quantum dots *(52)*, polystyrene microspheres *(51, 53, 54)*, lipid vesicles *(55)*, carbon nanotubes *(56)*, and even diatom templates *(57)*. Milam et al. *(51)* first assembled polystyrene microspheres via DNA hybridization in 2003, as shown schematically in Figure 1.3.1. Her work utilized a biotin-avidin linkage for immobilizing DNA strands on particle surfaces, and revealed that DNA hybridization at the surface was sufficient to cause programmed aggregation of 1.0 μm colloidal particles to form various binary structures. More recent work has investigated the thermal reversibility of micron-sized colloidal particles *(54, 58)*, as well as controlling the extent of aggregation by changing the number of surface immobilized strands or the ionic concentration of the solution *(53)*. They have also modified a carbodiimide linking process previously used for coupling DNA to magnetic beads *(59)*

for immobilizing aminated DNA on carboxylated polystyrene surfaces *(54)*. The carbodiimide coupling process results in surfaces with increased DNA density and strong covalently bound strands.

Theoretical work has been performed to calculate the various phase transitions and structures that could form upon DNA hybridization between various particles. Tkachenko's group has outlined the theory behind DNA-programmed colloidal crystallization in several papers *(60-62)*, and elucidated the factors that could lead to morphological diversity upon DNA-hybridization. In their work, DNA is a source of both repulsion and attraction, as highly negative non-complementary strands are not seen to undergo hybridization and serve rather to stabilize the particles. They find that this system exhibits a surprisingly diverse array of morphologies, including the diamond lattice *(60)*. In more recent work *(62)*, Tkachenko et al. have outlined the theory behind DNA-coded nanoclusters, in which building blocks are composed of specific sequences of DNA immobilized on nanoparticles. These building blocks can then be used to create hierarchical assemblies. In order to induce recognition-based assembly of the building blocks (triangular pyramids, octahedrons, etc.) they propose the use of "markers" which distinguish each particle *as well as* each assembled building block. These markers (specific oligonucleotide sequences) are able to hybridize to a linker with multiple linking sites on it (up to four, as opposed to the two sticky ends seen in Mirkin's work). In this way, small, compact aggregates with specific shape can be assembled while still presenting some strands for controlled assembly of the building blocks. Frenkel's group has also done considerable modeling on the phase behavior and design of ordered DNA-linked nanoparticle assemblies *(63, 64)*. In an early paper, they predict the phase-

separation temperature for nanocolloids covered with varying amounts of DNA. They find that the higher the ssDNA coverage, the sharper and higher the dissolution profile becomes. Their analysis suggests that it may be possible to map microscopic DNA sequences onto macroscopic phase behavior; indeed, this theory has led to a variety of DNA-linked detection systems *(65-67)*. In a later paper, Lukatsky and Frenkel develop a lattice model to represent spherical DNA-coated colloids with a variety of complementary DNA linkers in solution *(63)*. They investigate the ability to form low-symmetry phases (such as diamond cubic) and reveal that weak attractions and competitive binding (which allows for a type of kinetically controlled assembly) lead to the staged ordering of nanoparticle superstructures. Their modeling reveals that DNA linkers of *non-equal* lengths form bonds of different spacing – this spacing is key to allow for competitive binding and staged ordering of the suspension, allowing for the creation of multicomponent superstructures. Indeed, controlling the spacing has proven key for the creation of programmed colloidal crystal structures *(68, 69)*.

The combination of theoretical modeling and experimental understanding resulted in the first reported three-dimensional colloidal crystal structures that were programmed by DNA hybridization. Crocker demonstrated the successful colloidal crystallization of 1.0 μm microspheres driven by DNA hybridization and finds that reducing the number of strands present between particle surfaces using a PEG spacer is required *(54)*. Recently, both Gang *(68, 70)* and Mirkin's *(69)* groups have developed different but comparable approaches for mediating colloidal crystallization via DNA hybridization. Both groups rely upon variable linker lengths and oligonucleotide concentrations between hybridizing segments and the nanoparticle surfaces, as seen in Figure 1.3.2. By increasing the

distance between the surface and the hybridizing segment, greater conformational freedom is obtained. Further, the decreased number of linkers caused hybridization reactions to proceed slowly, allowing for particles to find the most favorable packing state – typically a crystal. The key to obtaining these equilibrium structures was decreasing the number of linkages to 4 or 6, as opposed to 20 or 30 between particles as seen in earlier work by Mirkin, in which the structures became kinetically trapped due to strong, irreversible attractions between nanoparticles. Both face-centered cubic (FCC) and body-centered cubic (BCC) structures have been formed, with particle volume fractions of only a few percent – the structure is primarily open to solution. These examples of programmed crystallization fulfill earlier promises of DNA assembly, and illustrate that programmed diamond lattices predicted in early theoretical studies might one day be obtained. However, recent work by Kim et al. has further detailed the complications with using DNA to program colloidal crystal structures *(71)*. They perform an equilibration study and modeling for micron-sized particles and introduce a mismatch to monitor impurity segregation. Interestingly, they find that even in optimized cases, some energetically favored structures may not be kinetically accessible due to inadequate surface equilibration and incorrect binding with mismatched strands. This work further reveals the detail that must be incorporated into designing DNA sequences for use in programmed assembly.

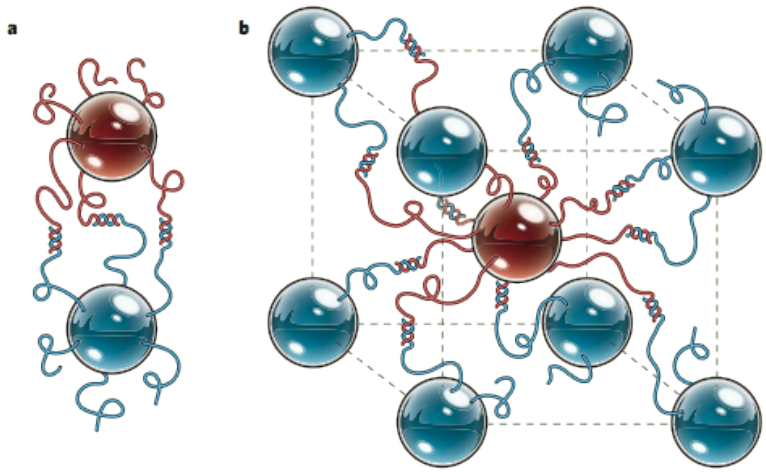

Figure 1.3.2 – Schematic of colloidal crystallization as developed by Nykpanchuk and Park. Long DNA strands at low concentrations allow for annealing of the structure as the bridges dynamically dissociate *(68)*.

1.3.3 - Phase Transitions in DNA-Linked Aggregates

Similar to DNA-driven colloidal crystallization, modulating DNA-induced aggregation behavior is highly dependent upon the ability to "tune" the number of linking duplexes that participate in the aggregation process. Tuning the linkages involves changing the number and affinity of active hybridizing strands that are present on the particle surfaces. One approach involves changing the salt concentration to effectively vary the Debye length screening of the phosphate groups *(63, 72)*. Biancaniello et al. investigated the phase behavior of microsphere suspensions as a function of both salt and duplex number *(53, 73)*. The number of DNA duplexes capable of participating in hybridization between complementary 1.0 μm particles was varied by titrating the surface with a nonsense strand that is not complementary to any other immobilized strand. Salt concentration is tuned from 25 to 200 mM by the addition of NaCl.

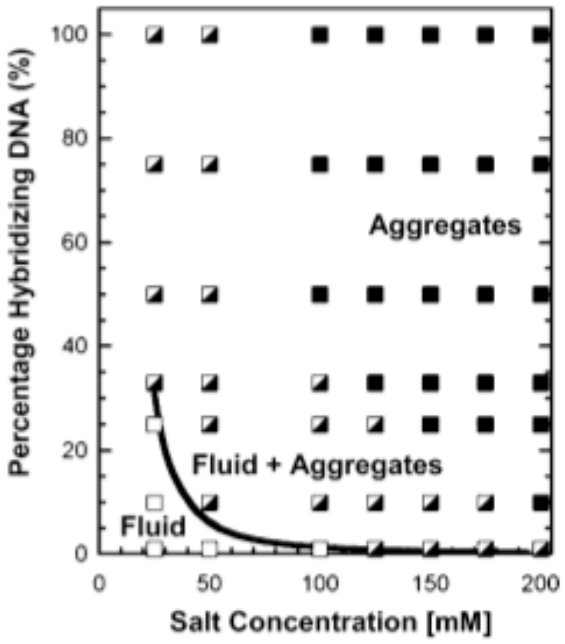

Figure 1.3.3 – Experimental phase diagram for DNA-mediated adhesion between polystyrene microspheres showing fluid (open squares), fluid + aggregates (half-filled squares) and aggregates (filled squares) as a function of salt concentration and percentage of linking oligonucleotides *(53)*.

They find that aggregates form at higher hybridizing DNA concentrations and higher salt concentrations, as expected. Further, a fluid + aggregates regime is reported for all but the lowest DNA and salt concentrations. Of greater interest, they find that at concentrations of salt greater than 50 mM, no fluid phase exists with as low as 1% hybridizing oligonucleotide present. This indicates that at higher salt concentrations, a single duplex may be sufficient to cause some particle aggregation, as indicated in Figure 1.3.3. Using line optical tweezers, Crocker's group separately reported the first direct measurement of DNA-induced interactions between colloidal microspheres *(74)*. By modeling the interactions measured with the optical tweezers, a pair potential energy

between DNA-linked particles was determined. It was found that the interaction energy is simply the number of bridges that form at equilibrium multiplied by k_BT. The DNA density used in the study permitted about 50 strands to span between the spheres, but it was determined that only a few percent of these needed to hybridize in order to cause particle aggregation.

1.4 - Reversing DNA-Linked Assemblies and Aggregates

1.4.1 - Reversing DNA-Linked Aggregates by Melting

1.4.1.1 - Melting Gold Nanoparticle Aggregates

DNA-linked particle suspensions are perhaps most recognized for their characteristic cooperative melting profiles *(29, 75)*. In aggregates linked by multiple DNA-duplexes, a sharp melting profile is observed at higher temperatures than observed for the same duplexes in solution (solution melting is discussed in section 1.2.2.1). Jin et al. have investigated the temperature-induced melting transitions of DNA-linked gold nanoparticle aggregates as a function of four variables: particle size, the surface density of oligonucleotides immobilized on the surface, the salt concentration of the medium, and the separation distance between the nanoparticles *(29)*. They attributed the sharp melting profiles observed for DNA-linked nanoparticles (compared to oligonucleotide solutions in the absence of nanoparticles) to a "cooperative" mechanism in which the local salt concentration decreases as the first duplexes melt to favor the subsequent dissociation of neighboring duplexes. Schatz has since elaborated on this cooperative behavior in several papers *(75-78)*. This melting behavior not only outlines the basis for the reversibility of

DNA-linked structures, but also lends insight into the thermodynamics of DNA-mediated particle assembly.

In DNA-linked aggregates, multiple duplexes exist between particle surfaces. According to the cooperative melting model, as the solution temperature is increased above the effective duplex melting temperature for DNA-linked particles, strands begin to dissociate. Once melting has occurred, the counterions associated with the linked duplexes are released, lowering the effective ionic concentration between particle surfaces, thus weakening the affinity between remaining duplexes *(29)*. This release of salt ions accelerates the melting process as indicated by a sharp melting transition which can occur over 1-2 °C. Schatz reports that the proposed cooperative melting model does correspond with predicted ion concentrations *(75)*. This sharp melting trend provides the basis for the use of DNA-linked nanoparticles in a variety of detection schemes. Cooperative melting has also been observed in the aggregation behavior of micron-sized particles *(58)*, again due to the presence of multiple, often more, linkages between microspheres.

Several variables affect the melting temperature of DNA-linked duplexes including duplex length, duplex concentration, salt concentration, and particle size. Since the salt type and concentration need to remain constant for biomaterials applications, duplex length and concentration are key parameters to investigate in the current study. It has been found that increasing the base-pair length of the linking duplex increases the melting temperature (and therefore stability) of the aggregate structure. However, previous studies on surface hybridization have also found that beyond a certain length, normally around 20 base pairs, hybridization efficiency decreases due, most likely, to

electrostatic repulsion. Thus, a balance between stability and aggregation or assembly (due to sufficient hybridization behavior) must be struck. Consequently, this work focuses on employing shorter linking duplexes between 8 and 16 bases long. Jin also finds that an increase in duplex density results in increasing melting temperature *(29)*. This is again explained by an increased avidity between particle surfaces, as well as increased local salt concentration that further stabilizes the linking duplexes. As we wish to redisperse DNA-linked aggregates as a final goal, the duplex concentration will require tuning - enough avidity will be required to allow particle aggregation or assembly to go to completion; however, the net adhesion must be weak enough to allow for subsequent particle redispersion or disassembly to proceed.

1.4.1.2 – Reversing DNA-Mediated Aggregation

Valignat et al. were the first to report thermal dissociation of aggregates comprised of micron-sized polystyrene particles by limiting the number of oligonucleotide linkages between particle surfaces *(58)*. They utilized DNA-immobilized surfaces that were "blocked" with either a solution of poly (ethylene oxide) (PEO) or an amphiphilic diblock copolymer. They found that the presence of blocking polymers allowed for micron sized particles to be aggregated via DNA hybridization, while still preventing the particles from falling into the deep primary attraction well in which aggregation is irreversible. Steric repulsion from the "adsorbed" polymer alone was insufficient to prevent aggregation. The key is putting a tight limit of one to three DNA linkages present between particles. Crocker employed a similar approach of carefully limiting the number of DNA linkages and controlling the cyclic thermal annealing conditions to report the first colloidal crystals mediated by reversible DNA hybridization

events *(54)*. In this research, PEG polymers were also used to reduce the number of DNA linkages between particles. Of further interest, they found that the addition of a second blocking agent called Tween-20 allowed the complete dissociation of the DNA-linked aggregate upon heating.

1.5 - Enzymatic Processing of DNA

1.5.1 - Restriction Endonuclease Clipping

1.5.1.1 - Clipping of Immobilized Sequences

The use of enzymes such as restriction endonucleases is an exciting tool for manipulating the presentation of oligonucleotides for hybridization events both on planar and particle surfaces. Restriction enzymes are capable of cleaving double stranded DNA at a specific recognition site, typically a four base-long sequence *(79)*. They are used extensively in a wide variety of biotechnology-related processes, but have only recently been adopted for modifying surface-immobilized DNA strands. Previously, Brust reported using various restriction endonucleases to clip strands immobilized on gold nanoparticles *(80)*. Using electrophoresis assays to measure oligonucleotide length following clipping and displacement from the nanoparticle surface, groups have recently reported digest efficiencies of up to 90% *(81)*, dramatically more efficient than earlier work showing only approximately 65% clipping. These studies using restriction endonuclease clipping on DNA-functionalized surfaces have relied on strands of length 40 to 100 bases in length *(80-82)*. In them, the recognition site for the endonuclease is typically separated from the surface by 16 to 36 base pairs. In prior work *(43, 83-85)*, for

example, the start of the recognition sequence is located at 16 (*EcoRV*), 22 (*EcoRI*), 32 (*MapI*), 34 (*StyI*), and 36 (*EcoRV*) bases away from the surface of gold nanoparticles. A wide array of clipping schemes such as these have been investigated; this is only a representative list.

1.5.1.2 - Enzymatic Clipping for Particle Redispersion

Recently, Kanaras et al. employed restriction endonuclease digests to redisperse DNA-linked gold nanoparticles by clipping the DNA duplexes at a particular recognition segment *(84)*. By placing recognition segments in the linking duplex that forms between particles, they found it was possible to redisperse aggregates of DNA-linked gold nanoparticles. This enzyme-based approach thus provides an alternative way to redisperse DNA-linked assemblies or aggregates. Lim et al. use a similar technique to intervene in the processes of assembly and disassembly of DNA modified nanoparticles causing programmed redispersion of DNA-linked particles with the restriction enzyme *Msp I (86)*. However, both of these enzymatic approaches require a buffer exchange that is not feasible for many biotechnology applications. Further, the rate of clipping appears to depend solely on the enzyme choice – our competition-based approach allows control over the replacement rate constant.

1.5.2 – Other Enzymes Used to Modify Immobilized Sequences

As opposed to enzymatic cleavage of DNA, Keating employed DNA ligases to *extend* immobilized strands *(87)*. In these studies, the gold nanoparticle bound oligonucleotides serve as primers for enzymatic extension reactions. They found that using low DNA surface coverage and incorporating spacers to achieve greater separation distances between the particle surface and recognition site led to increased enzymatic

activity. Steric interactions were again found to play a tremendous role in modulating the activity of oligonucleotide probes at particle surfaces. Kanaras has since adopted this approach to develop site-specific ligation protocols *(88)*, whereby the sticky-ends of cleaved strands (clipped with the non-palindromic endonuclease *StyI*) can then be extended by T4 DNA ligase. This technique produces a bifunctional surface with oligonucleotides of varying length.

1.6 - Competitive Hybridization

Competitive binding of secondary oligonucleotide targets to drive the redispersion of DNA-linked aggregates presents a unique alternative to thermal melting and restriction endonuclease processing and does not require changes in buffer or temperature conditions. Competition between active and inhibitory ligands for the binding pocket of a receptor is known to play a significant role in cellular signaling *(89)*. In fact, the equilibrium dissociation rates for receptor-ligand pairs in biological systems are often determined experimentally using competition assays without temperature or buffer adjustments *(90)*. Typically, a fluorescent marker distinguishes the original and competitive ligands from each other for experimental purposes but otherwise the ligands do not possess any affinity differences for binding to the receptor. The affinity between oligonucleotide targets and probes, on the other hand, can greatly differ depending on sequence characteristics such as base-length and fidelity in base-pair matching. Oligonucleotide-based competition assays are used to monitor polymerase chain reaction-based DNA amplification *(91)* as well as real-time FRET events *(92)*. Hybridization

events allow nucleic acid probes called molecular beacons to report the presence and activity of targets through the activation of a fluorescence signal as duplexes form *(93-97)*. Molecular beacons are initially present in a loop-stem configuration in which a single-stranded loop is closed by a short duplex formed between the two ends labeled with quencher and dye molecules. The close proximity between the two ends in the hairpin conformation thus prohibits detectable fluorescence emission. Unfolding of the original loop, however, occurs as the target strand is added to form a longer, and thus more stable duplex that can now fluoresce. Tsourkas et al. investigated the kinetics and thermodynamics of these molecular beacon hybridization reactions *(96)*, and developed a design framework for efficient unfolding of the single-stranded loop as duplexes form with the target. They reported that increasing the length of the stem hybridization segment (in the loop) decreases the rate of beacon-target hybridization, but does increase the ability to discriminate among different targets. A similar situation is evident in our studies whereby a balance must be struck between sufficient, but weak hybridization activity to induce complete, but ultimately reversible DNA-mediated adhesion between microsphere surfaces. Further, work on shared-stem molecular beacons has shown that displacing a previously hybridized stem segment (in a true DNA displacement reaction, or DDR) offers greater sensitivity and specificity of hybridization *(95)*.

Competitive hybridization events on planar surfaces have also been studied *(98, 99)*; typically using single base mismatches to induce affinity differences (as opposed to the increased secondary target lengths used in our studies). Bishop et al. use real-time dual-color fluorescence detection to experimentally track target species during competitive hybridization at a surface and monitor the displacement of the lower affinity

species over time *(98)*. Reynaldo et al. describe the kinetics of competitive or secondary target hybridization in terms of dissociative and sequential displacement pathways as seen in Figure 1.6.1 *(100)*. Their studies focus on replacing one hybridization partner with another of equivalent length in DNA solutions (in the absence of colloidal particles). The dissociative pathway involves a complete melting and removal of the primary target, followed by hybridization of the secondary target with the unoccupied probe. Sequential displacement, on the other hand, involves opening a three or four base-long nucleation site during transient melting events to allow the secondary target to first hybridize to this short single-stranded segment and then complete duplex formation by displacing the original target. They report that the displacement pathway tends to dominate at lower temperatures, while the dissociative pathway, with significantly higher activation energy, prevails at temperatures near the T_m of the duplex. Since the displacement pathway dominates at room temperature conditions used in our experiments, it is the more likely mechanism for secondary hybridization events for our system.

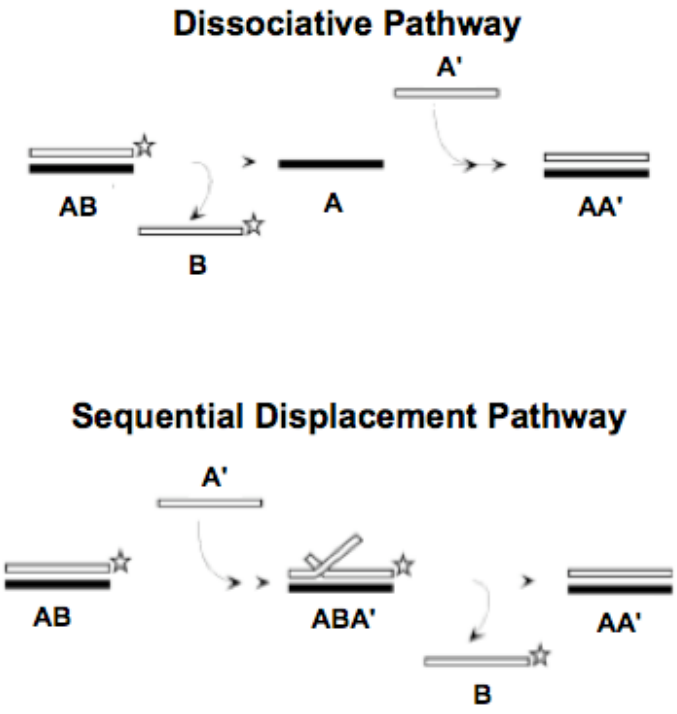

Figure 1.6.1 – Schematic of dissociative and sequential displacement pathways. The dissociative pathway shows complete primary target removal (**B**) before secondary target (**A'**) hybridization occurs. Sequential displacement shows the secondary target forming a toehold duplex and then competing with the primary target for the probe (**A**). Modified from *(100)*.

Aldaye et al. have applied DDR reactions to control the geometry of three dimensional gold nanoparticle assemblies *(101, 102)*. In their work, competitive hybridization with longer secondary targets is used to modify linkages between particles and therefore induce conformational change. Recently, Zhang et al. built on the work described herein and developed a technique for selective removal of DNA-labeled nanoparticles from a planar surface *(103)*. They utilize the specificity of competition described herein to cause specific removal of heterogeneous DNA-linked particles individually from a planar surface.

1.7 – Summary and Impact of Research

The above literature review detailed the colloidal science field, specific interactions for controlled colloidal aggregation, and the use of DNA as a colloidal assembly tool. Various techniques for the control of nano to micron-sized particles via DNA hybridization were outlined. The use of various enzymes to manipulate these structures was discussed, and competitive hybridization reactions are introduced last.

This thesis reports the use of soluble competitive oligonucleotides to restabilize DNA-linked microsphere aggregates. Though competition plays a key role in many oligonucleotide and non-nucleotide-based binding events and assays, to the best of our knowledge this study is the first to report using competitive DNA hybridization events to mediate reversible adhesion between colloidal particles. We begin by developing a DNA-linked structure with weak, but sufficient, attractive interactions to drive microsphere aggregation to completion. We next investigate several schemes to modulate the number of DNA linkages that exist between particles, including a novel enzyme based protocol which will further reveal the importance of steric effects at the surface of colloidal particles. After selection of a DNA-mediated aggregation system, we then quantify the ability of competitive strands to displace primary target strands, and investigate the ability of these competitive strands to restabilize aggregates back into dispersed singlets. In order to completely restabilize the particles, however, the number of DNA linkages between pairs of microspheres must be reduced to allow for efficient competitive displacement of the shorter target. The kinetics of the competitive system is next investigated, and soluble and immobilized cases are compared. The kinetic research is of

great importance for a variety of bead-based and microarray detection techniques currently being investigated. Finally, a novel use of the competitive hybridization reaction is shown which allows for sheddable coatings, of great interest in drug delivery vehicles. We believe this work presents an important first step towards extending DNA as a reversible assembly tool in physiological systems. Further, as opposed to prior research in which groups have utilized DNA hybridization to program assembly of colloidal particles, here we program *disassembly* of similar structures by optimizing affinity differences between primary and competitive strands.

References

1. Hiemenz, P.C. and Rajagopalan, R., *Principles of Colloid and Surface Chemistry*. Third ed. 1997, New York: Marcel Dekker, Inc.

2. Lewis, J.A. *J. Am. Ceram. Soc.*, **2000**. *83*. 2341-59.

3. Lange, F.F. *J. Am. Ceram. Soc.*, **1989**. *72*. 3-15.

4. Larson, R.G., *The Structure and Rheology of Complex Fluids*. First ed. 1998, USA: Oxford University Press.

5. Cram, L.S. *Methods in Cell Science*, **2003**. *24*. 1-9.

6. Anderson, V.J., de Hoog, H., and Lekkerkerker, H.N. *Phys. Rev. E*, **2001**. *65*. 011403.

7. Anderson, V.J. and Lekkerkerker, H.N. *Nature*, **2002**. *416*. 811-5.

8. Fritz, G., Schädler, V., Willenbacher, N., and Wagner, N.J. *Langmuir*, **2002**. *18*. 6381-90.

9. Pusey, P.N. and Megen, W.v. *Nature*, **1986**. *320*. 340-2.

10. Chan, A.T. and Lewis, J.A. *Langmuir*, **2005**. *21*. 8576-9.

11. Gatica, S.M., Cole, M.W., and Velegol, D. *Nano Lett.*, **2005**. *5*. 169-73.

12. Liu, J. and Luijten, E. *Phys. Rev. Lett.*, **2005**. *93*. 247802.

13. Kleshchanok, D. and Lang, P.R. *Langmuir*, **2007**. *23*. 4332-9.

14. Ogden, A.L. and Lewis, J.A. *Langmuir*, **1996**. *12*. 3413-24.

15. Mao, Y., Cates, M.E., and Lekkerkerker, H.N. *Physica A*, **1995**. *222*. 10-24.

16. Kim, A.J., Manoharan, V.N., and Crocker, J.C. *J. Am. Chem. Soc.*, **2005**. *127*. 1592-3.

17. Storhoff, J.J., Elghanian, R., Mirkin, C.A., and Letsinger, R.L. *Langmuir*, **2002**. *18*. 6666-70.

18. Walker, H.W. and Grant, S.B. *J. of Colloid and Int. Sci.*, **1996**. *179*. 552-60.

19. Gilchrist, J.F., Chan, A.T., Weeks, E.R., and Lewis, J.A. *Langmuir*, **2005**. *21*. 11040-7.

20. Yin, Y. and Xia, Y. *Adv. Mater.*, **2001**. *13*. 267-71.

21. Hiddessen, A.L., Rodgers, S.D., Weitz, D.A., and Hammer, D.A. *Langmuir*, **2000**. *16*. 9744-53.

22. Shenton, W., Davis, S.A., and Mann, S. *Adv. Mater.*, **1999**. *11*. 449-52.

23. Connolly, S. and Fitzmaurice, D. *Adv. Mater.*, **1999**. *11*. 1202-05.

24. Calladine, C.R., Drew, H.R., Luisi, B.F., and Travers, A.A., *Understanding DNA: The Molecule and How it Works*. Third ed. 2004, San Diego: Elsevier Academic Press. 334.

25. Leja, D. *DNA - a more detailed description*. Accessed 11/12/2008; Available from: http://www.accessexcellence.org/AB/GG/dna2.html.

26. Materials Research Science & Engineering Centers. *DeoxyriboNucleicAcid*. Accessed 2/13/2009; Available from: http://mrsec.wisc.edu/Edetc/background/DNA/images/DNAcolor.JPG.

27. Cluzel, P., Lebrun, A., Heller, C., Lavery, R., Viovy, J.L., Chatenay, D., and Caron, F. *Science*, **1996**. *271*. 792-4.

28. Smith, S.B., Cui, Y.J., and Bustamante, C. *Science*, **1996**. *271*. 795-9.

29. Jin, R., Wu, G., Li, Z., Mirkin, C.A., and Schatz, G.C. *J. Am. Chem. Soc.*, **2003**. *125*. 1643-54.

30. Park, S.Y. and Stroud, D. *Phys. Rev. B*, **2003**. *67*. 212202.

31. SantaLucia, J. *Proc. Natl. Acad. Sci. U.S.A.*, **1998**. *95*. 1460-5.

32. Chen, J.H. and Seeman, N.C. *Nature*, **1991**. *350*. 631-3.

33. Du, S.M., Zhang, S., and Seeman, N.C. *Biochemistry*, **1992**. *31*. 10955-63.

34. Mathieu, F., Liao, S., Kopatsch, J., Wang, T., Mao, C., and Seeman, N.C. *Nano Lett.*, **2005**. *5*. 661-5.

35. Mueller, J.E., Du, S.M., and Seeman, N.C. *J. Am. Chem. Soc.*, **1991**. *113*. 6306-08.

36. Wang, Y.L., Mueller, J.E., Kemper, B., and Seeman, N.C. *Biochemistry*, **1991**. *30*. 5667-74.

37. Winfree, E., Liu, F., Wenzler, L.A., and Seeman, N.C. *Nature*, **1998**. *394*. 539-44.

38. Zuker, M. *Mfold Web Server*. **2003**; Available from: http://mfold.bioinfo.rpi.edu/.

39. IDT. *SciTools Oligo Analyzer*. **2009**; Available from: http://www.idtdna.com/analyzer/Applications/OligoAnalyzer/.

40. Watson, J.D. and Crick, F.H. *Nature*, **1953**. *171*. 737-8.

41. Venter, J.C., et al. *Science*, **2001**. *291*. 1304-51.

42. Alberts, B., Johnson, A., Lewis, J., Raff, M., Roberts, K., and Walter, P., *The Cell*. Fourth ed. 2002, New York: Garland Science.

43. Wang, Z.X., Kanaras, A.G., Bates, A.D., Cosstick, R., and Brust, M. *Journal of Materials Chemistry*, **2004**. *14*. 578-80.

44. Gothelf, K.V. and LaBean, T.H. *Org. Biomol. Chem.*, **2005**. *3*. 4023-37.

45. Aldaye, F.A. and Sleiman, H.F. *J. Am. Chem. Soc.*, **2007**. *129*. 4130-1.

46. Aldaye, F.A. and Sleiman, H.F. *J. Am. Chem. Soc.*, **2007**. *129*. 13376-7.

47. Frutos, A.G., Liu, Q., Thiel, A.J., Sanner, A.M., Condon, A.E., Smith, L.M., and Corn, R.M. *Nucleic Acids Res.*, **1997**. *25*. 4748-57.

48. Bashir, R. *Superlattices and Microstructures*, **2001**. *29*. 1-16.

49. Mirkin, C.A., Letsinger, R.L., Mucic, R.C., and Storhoff, J.J. *Nature*, **1996**. *382*. 607-9.

50. Alivisatos, A.P., Johnsson, K.P., Peng, X., Wilso, T.E., Loweth, C.J., Bruchez, M.P., and Schultz, P.G. *Nature*, **1996**. *382*. 609-11.

51. Milam, V.T., Hiddessen, A.L., Crocker, J.C., Graves, D.J., and Hammer, D.A. *Langmuir*, **2003**. *19*. 10317-23.

52. Mitchell, G.P., Mirkin, C.A., and Letsinger, R.L. *J. Am. Chem. Soc.*, **1999**. *121*. 8122-3.

53. Biancaniello, P.L., Crocker, J.C., Hammer, D.A., and Milam, V.T. *Langmuir*, **2007**. *23*. 2688-93.

54. Kim, A.J., Biancaniello, P.L., and Crocker, J.C. *Langmuir*, **2006**. *22*. 1991-2001.

55. Beales, P.A. and Vanderlick, T.K. *J Phys Chem A*, **2007**. *111*. 12372-80.

56. Jung, D.H., Kim, B.H., Ko, Y.K., Jung, M.S., Jung, S., Lee, S.Y., and Jung, H.T. *Langmuir*, **2004**. *20*. 8886-91.

57. Rosi, N.L., Thaxton, C.S., and Mirkin, C.A. *Angew. Chem. Int. Ed. Engl.*, **2004**. *43*. 5500-3.

58. Valignat, M.P., Theodoly, O., Crocker, J.C., Russel, W.B., and Chaikin, P.M. *Proc. Natl. Acad. Sci. U.S.A.*, **2005**. *102*. 4225-9.

59. Lund, V., Schmid, R., Rickwood, D., and Hornes, E. *Nucleic Acids Res.*, **1988**. *16*. 10861-80.

60. Tkachenko, A.V. *Phys. Rev. Lett.*, **2002**. *89*. 148303.

61. Licata, N.A. and Tkachenko, A.V. *Phys. Rev. E*, **2006**. *74*. 041406.

62. Licata, N.A. and Tkachenko, A.V. *Phys. Rev. E*, **2006**. *74*. 040401.

63. Lukatsky, D.B. and Frenkel, D. *Phys. Rev. Lett.*, **2004**. *92*. 068302.

64. Lukatsky, D.B., Muler, B., and Frenkel, D. *J. of Physics*, **2006**. *18*. S567-80.

65. Elghanian, R., Storhoff, J.J., Mucic, R.C., Letsinger, R.L., and Mirkin, C.A. *Science*, **1997**. *277*. 1078-81.

66. Park, S.J., Taton, T.A., and Mirkin, C.A. *Science*, **2002**. *295*. 1503-6.

67. Taton, T.A., Mirkin, C.A., and Letsinger, R.L. *Science*, **2000**. *289*. 1757-60.

68. Nykypanchuk, D., Maye, M.M., van der Lelie, D., and Gang, O. *Nature*, **2008**. *451*. 549-52.

69. Park, S.Y.T.L., Lytton-Jean …, A.K.R., Lee, B., Weigand, S., Schatz, G.C., and Mirkin, C.A. *Nature*, **2008**. *451*. 553-6.

70. Xiong, H., van der Lelie, D., and Gang, O. *J. Am. Chem. Soc.,* **2008**. *130.* 2442-3.

71. Kim, A.J., Scarlett, R., Biancaniello, P.L., Sinno, T., and Crocker, J.C. *Nature Materials*, **2009**. *8*. 52-5.

72. Sun, Y., Harris, N.C., and Kiang, C.H. *Plasmonics*, **2007**. *2,* 193-9.

73. Nykypanchuk, D., Maye, M.M., Lelie, D.V., and Gang, O. *Langmuir*, **2007**. *23*. 6305-14.

74. Biancaniello, P.L. and Crocker, J.C. *Review of Scientific Instruments*, **2006**. *77*. 113702.

75. Long, H., Kudlay, A., and Schatz, G.C. *J. Phys. Chem. B*, **2006**. *110*. 2918-26.

76. Gibbs-Davis, J.M., Schatz, G.C., and Nguyen, S.B.T. *J. Am. Chem. Soc*, **2007**. *129*. 15535-40.

77. Kudlay, A., Gibbs, J.M., Schatz, G.C., Nguyen, S.T., and Cruz, M.O. *J. Phys. Chem. B*, **2007**. *111*. 1610-9.

78. Park, S.Y., Gibbs-Davis, J.M., Nguyen, S.T., and Schatz, G.C. *J. Phys. Chem. B*, **2007**. *111*. 8785-91.

79. *New England Biolabs Catalog and Technical Reference*. 2007-2008: Ipswich, MA. p. 400.

80. Kanaras, A.G., Wang, Z., Bates, A.D., Cosstick, R., and Brust, M. *Angew. Chem. Int. Ed. Engl.*, **2003**. *42*. 191-4.

81. Qin, W.J. and Yung, L.Y. *Biomacromolecules*, **2006**. *7*. 3047-51.

82. Qin, W.J. and Yung, L.Y. *Langmuir*, **2005**. *21*. 11330-4.

83. Kanaras, A.G., Wang, Z., Bates, A.D., Cosstick, R., and Brust, M. *Angew. Chem. Int. Ed. Engl.*, **2003**. *42*. 191-4.

84. Kanaras, A.G., Wang, Z., Brust, M., Cosstick, R., and Bates, A.D. *Small*, **2007**. *3*. 590-4.

85. Qin, W.J. and Yung, L.Y.L. *Langmuir*, **2005**. *21*. 11330-4.

86. Lim, I.S., Chandrachud, U., Wang, L., Gal, S., and Zhong, C. *Anal. Chem.* **2008**. *80.* 6038-44.

87. Nicewarner Peña, S.R., Raina, S., Goodrich, G.P., Fedoroff, N.V., and Keating, C.D. *J. Am. Chem. Soc.*, **2002**. *124*. 7314-23.

88. Kanaras, A.G., Wang, Z., Hussain, I., Brust, M., Cosstick, R., and Bates, A.D. *Small*, **2007**. *3*. 67-70.

89. Li, P., Selvaraj, P., and Zhu, C. *Biophys. J.*, **1999**. *77*. 3394-406.

90. Scheuermann, J., Viti, F., and Neri, D. *J. Immunol. Methods*, **2003**. *276*. 129-34.

91. Cheng, J., Zhang, Y., and Li, Q. *Nucleic Acids Res.*, **2004**. *32*. e61.

92. Ho, F.M. and Hall, E.A. *Biosensors & bioelectronics*, **2004**. *20*. 1001-10.

93. Tyagi, S. and Kramer, F.R. *Nature Biotech.*, **1996**. *14*. 303-8.

94. Bonnet, G., Tyagi, S., Libchaber, A., and Kramer, F.R. *Proc. Natl. Acad. Sci. U.S.A.*, **1999**. *96*. 6171-6.

95. Tsourkas, A., Behlke, M.A., and Bao, G. *Nucleic Acids Res.*, **2002**. *30*. 4208-15.

96. Tsourkas, A., Behlke, M.A., Rose, S.D., and Bao, G. *Nucleic Acids Res.*, **2003**. *31*. 1319-30.

97. Santangelo, P., Nitin, N., and Bao, G. *Annals of biomedical engineering*, **2006**. *34*. 39-50.

98. Bishop, J., Wilson, C., Chagovetz, A.M., and Blair, S. *Biophys. J.*, **2007**. *92*. L10-2.

99. Zhang, Y., Hammer, D.A., and Graves, D.J. *Biophys. J.*, **2005**. *89*. 2950-9.

100. Reynaldo, L.P., Vologodskii, A.V., Neri, B.P., and Lyamichev, V.I. *J. Mol. Biol.*, **2000**. *297*. 511-20.

101. Aldaye, F.A. and Sleiman, H.F. *J. Am. Chem. Soc.*, **2007**. *129*. 4130-1.

102. Aldaye, F.A. and Sleiman, H.F. *J. Am. Chem. Soc*, **2007**. *129*. 13376-7.

103. Zhang, Z., Cheng, Q., and Feng, P. *Angew. Chem. Int. Ed.*, **2009**. *48*. 118-22.

CHAPTER 2

Primary Hybridization Events between Immobilized Probes and Either Soluble or Immobilized Targets

This chapter will detail the initial investigations into probe immobilization and primary hybridization for select oligonucleotide sequences. First, an EDAC coupling procedure will be detailed, and several variables that affect coupling density are investigated by hybridizing probes to soluble fluorescently-labeled targets to measure probe duplex densities on the particle surfaces. In these studies, the effect of changing the hybridizing base-pair overlap and time of incubation are investigated. Modest but sufficient hybridization activity is desirable for DNA-mediated assembly or aggregation, thus the shortest target with moderate hybridization activity is chosen for subsequent colloidal assembly and aggregation experiments. Numeric calculations allow us to approximate the maximum number of DNA-duplex linkages required for driving DNA-mediated particle assembly or aggregation to completion.

2.1 – Experimental Setup

2.1.1 - Oligonucleotide Selection

Aminated and FITC-tagged single-stranded oligonucleotides were purchased from Invitrogen. Strands were purified by the supplier using HPLC and were aliquoted upon arrival to 100 μM concentration in Tris-EDTA (TE) (Fisher Scientific) and stored at -20 °C until used. FITC-labeled oligonucleotides are stored in TE pH 8.0, while all other strands are stored in TE pH 7.4. The hybridization segment of all sequences was chosen

based on the work of Seeman and coworkers *(1)*. Selected strands have a moderate calculated duplex melting temperature as shown in Table 2.1.1 as well as a low self-melt temperature (less than 0 °C) as calculated through Zuker's Mfold web server *(2, 3)*.

Together, the moderate duplex melting temperature and the low self-melt temperatures indicate that duplex formation between two complementary strands is more favorable than the formation of intra-strand loops or hairpins within a single strand. In addition, this low self-melt temperature indicates that the affinity between identical sequences is low. For Chapters 2 through 5, the strand nomenclature will be as follows: complementary strands employed for primary hybridization events are labeled as **A** and **B** (with **A** being complementary to **B**), followed by the total number of bases. All bases in the soluble strands (i.e. not immobilized on microsphere surface) are intended for hybridization events. For oligonucleotides immobilized on microspheres, the first four to twelve bases are included as a spacer segment between the microsphere surface and the hybridization segment (eight to sixteen bases in length). Multiple copies of an identical sequence (**A20** or **B20**) are immobilized on one of two populations of microspheres for aggregation experiments. To allow for coupling of DNA to carboxylated microspheres of varying size and fluorescence functionality, surface-functionalized strands possess an amine functionality on their 5' end *(4-6)*. For flow cytometry, **A20**-immobilized nonfluorescent microspheres are used. Soluble **B** sequences are employed as primary target strands for flow cytometry. These soluble stands are fluorescently labeled with fluorescein isothiocyanate (FITC) on the 5' end for quantifying primary hybridization activity.

Table 2.1.1. Candidate sequences and theoretical melting temperatures for flow cytometry-based primary hybridization experiments *(7)*.

function	sequence	T_m
immobilized probe	**A20** = 5'-TTTTTTGGATTGCGGCTGAT-3'	NA
noncomplementary soluble target	**NC20** = 5'- TTTTTTGGATTGCGGCTGAT-3'	NA
soluble 1° targets	**B6** = 3'-CGACTA-5'	41.4 °C
	B8 = 3'-GCCGACTA-5'	61.5 °C
	B10 = 3'-ACGCCGACTA-5'	72.0 °C
	B12 = 3'-TAACGCCGACTA-5'	72.6 °C
	B14 = 3'-CCTAACGCCGACTA-5'	75.2 °C
	B16 = 3'-AACCTAACGCCGACTA-5'	76.6 °C

2.1.2 - Particle Preparation

Nonfluorescent 1.04 μm and 5.01 μm carboxylated polystyrene particles (Bangs Laboratories, Fishers, IN) and 1.1 μm red fluorescent carboxylated polystyrene particles (Molecular Probes, Eugene, OR) are used for aggregation experiments (Appendix B shows details of all microsphere populations). The carboxyl surface functionality allows for covalent coupling with aminated probe strands using 1-ethyl-3-[3-dimethylaminopropyl]carbodiimide hydrochloride (EDAC) chemistry *(8)*. Coupling is performed in a buffer that is identical to the PolyLink Coupling Kit (Bangs Laboratories) *(8)*. This house coupling buffer (HCB) is composed of 50 mM MES (Acros Organics), 0.05% Pro-Clin 300 (Supelco), adjusted to pH 5.2 using 4 M NaOH solution. Following one hour of mixing, the buffer is filtered through a 0.2 μm syringe tip filter. To immobilize aminated probes on the surface of carboxylated beads, the following protocol is used. First, 10.0 μL of carboxylated particles are washed twice in 100 μL HCB. Following the second wash, the particles are resuspended in HCB to a volume of 150 μL. 50 μL of HCB is then added to 10.0 mg of pre-weighed EDAC (Sigma) which has been

previously aliquoted and stored in a septa-topped vial backfilled with Nitrogen. The EDAC/HCB mixture is then briefly mixed, and a varying amount is added to the particle suspension (typically 25 µL, or 5.0 mg EDAC). All work performed with EDAC is done with expediency, as EDAC is highly reactive in aqueous environments. Aminated DNA is then added to the suspension at 10.0 µM concentration. The suspension is again mixed, and incubated for 1 to 24 hours. PBS/Tween buffer (1x PBS, Nanopure water, 0.05% Tween-20) is then used to wash the suspension three times. Figure 2.1.1 shows a schematic of the EDAC coupling procedure. Following conjugation, particles are resuspended in 100 µL of PBS/Tween for storage as a 0.01 volume fraction suspension.

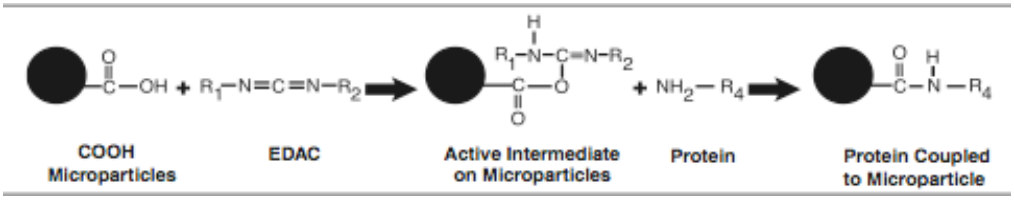

Figure 2.1.1 – Schematic of EDAC coupling procedure. Carboxylated microparticles converted to active intermediate after introduction of EDAC agent. Aminated species (here, a protein) are then immobilized on the microparticles through amide bond formation *(8)*.

Prior to flow cytometry or aggregation, particles were re-suspended in a hybridization buffer consisting of PBS with 0.05% Tween 20 (PBS/TWEEN). To prepare the hybridization and storage buffer, TWEEN 20 (or Polysorbate 20, Calbiochem) and PBS (Phosphate Buffered Saline, Sigma-Aldrich) are mixed for one hour at room temperature and then filtered through a 0.2 µm syringe-tip filter. The non-fluorescent microspheres

(5.0 μm microspheres were used for select assembly experiments in Chapter 2, the remainder of the experiments in this chapter were run solely with 1.0 μm particles) are functionalized with **A20** strands, while the fluorescent microspheres are functionalized with the complementary **B20** strands.

2.1.3 - Flow Cytometry

Using FITC-labeled target strands, the primary hybridization activity of **A20** probe strands immobilized on nonfluorescent microspheres is quantified via flow cytometry. To investigate the effect of base-pair overlap and incubation time on the resulting surface density of hybridized probe strands, FITC-labeled target strands of varying overlap length (**B8/FITC, B10/FITC, B12/FITC, B14/FITC, B16/FITC)** were incubated with the **A20**-functionalized nonfluorescent microspheres (two different coupled batches) for 1 to 48 hours in hybridization buffer of (PBS/TWEEN). Flow cytometry samples are prepared as follows. Briefly, 2.5 μL of probe-functionalized microspheres are washed one time in 100 μL of PBS/TWEEN and resuspended to a total volume of 100 μL. A 100 μL volume of 10 μM FITC-labeled DNA target is then added and incubated with the microspheres for the designated time. The samples are then washed three times in PBS/TWEEN buffer to remove any unassociated target strands. Flow cytometry samples are prepared by diluting the suspension to 1.0 mL, resulting in a suspension concentration of approximately 10^6 microspheres/mL. Flow cytometry is run on a Becton Dickinson FACS II flow cytometer. Each run of samples consisted of (a) DNA-functionalized microspheres alone (negative), (b) DNA-functionalized microspheres incubated with FITC-labeled targets identical in sequence to the **A20** probe strands (negative-**NC20)**, and (c) DNA-functionalized microspheres incubated with

complementary, FITC-labeled target strands (**B8/FITC** – **B16/FITC**) with varying number of base-pair matches to the **A20** probe strands. A total of four sets split between two coupled batches were run. BDFacs DIVA software was used for data acquisition, and collection was performed with both forward scatter counts (FSC) and side scatter counts (SSC) on a linear scale, while the mean fluorescence intensity (FITC-A) was collected on a logarithmic scale. This method allows for consistent gating of the singlet population between runs by monitoring the population of singlets on the FSC vs. SSC dot-plot. Because FSC and SSC data detail the size and irregularity of particle shape, and it is known through microscopy that the sample is a fairly homogeneous singlet population, it is possible to "gate" the dominant singlet population be monitoring the percent of the sample in each regime. Figure 2.1.2 shows a representative dot-plot for the 1.04 μm microsphere system with a gate on the singlet population. The FITC values are plotted on a logarithmic histogram as the number of counts at each FITC intensity. These peaks are then analyzed for the mean intensity *within the singlet population*. To calculate the surface density of hybridized target strands, mean fluorescence intensity values were compared to calibration curves generated with Quantum MESF FITC Medium calibration standards (Bangs Labs).

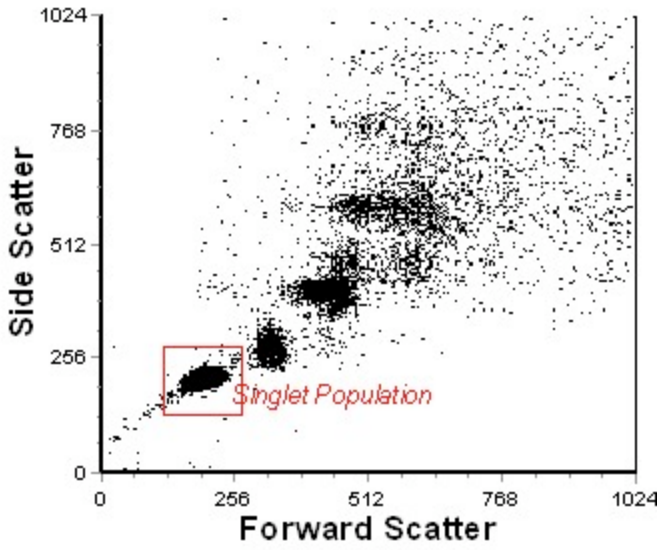

Figure 2.1.2 – Representative dot-plot for forward scatter counts (FSC) vs. side scatter counts (SSC). Gated region shown in red is the singlet population that accounts for approximately 85% of the sample. Doublets, triplets, and larger size clusters or aggregates can be observed by progressively moving towards higher FSC and SSC values.

2.1.4 - Duplex Number and Concentration Calculations

Using data collected from flow cytometry experiments on primary targets hybridized to surface-bound probes, it is possible to calculate the maximum number of DNA strands present for hybridization between particles, the maximum number of duplexes formed, and the concentration of DNA in a volumetric shell surrounding each particle using geometrical arguments *(9)*. These calculations are based on average surface densities derived from the four individual sets tested. To calculate the concentration of DNA in a volumetric shell surrounding each particle for oligonucleotide melting calculations, the effective radius due to a brush-like layer of single-stranded oligonucleotides on the surface of the particle is determined, as shown in Figure 2.1.3. For single-stranded DNA, the distance between neighboring nucleotides along the

phosphate backbone is 0.59 nm *(10)*; for a 20 base DNA strand, this results in an extended particle radius of 11.21 nm, or an effective radius of 511.21 nm for particles with a reported (by the manufacturer) physical radius of 502 nm. Using the volume of the sphere spanned by the effective radius and subtracting the physical volume of the particle itself, the result is the volume of the DNA "shell," V_{shell} as shown in equation 2.1.1.

$$V_{shell} = \frac{4}{3}\pi\left(r_{eff}\right)^3 - \frac{4}{3}\pi\left(r_{part}\right)^3 \tag{2.1.1}$$

It is then possible to determine the molar concentration of DNA using the definition of molarity, shown below in equation 2.1.2.

$$M_{DNA} = \frac{n_{strands}}{N_A \times V_{shell}} \tag{2.1.2}$$

Geometrical arguments are again made for the calculation of the maximum number of DNA-strands present between spheres which can participate in hybridization by calculating the projected contact zone area between two curved surfaces, as shown in Figure 2.1.4. This approach takes into account the stretching possible between DNA-duplexes that can extend up to 1.7 times their unstretched length, but assumes that single-stranded segments act as stiff rods *(11)*. This stretching approximation will allow the determination of the contact zone over which hybridization can occur, as the particle surfaces become more separated and their curved surfaces bend away from one another. The important parameters are as follows: r_{part}, the particle radius, s, the calculated

difference between the length of the unstretched (l_{hyb}) and the stretched (l_{str}) hybridization segments; and y, the calculated radius of the contact zone area. The determination of these variables is shown in equations 2.1.3 through 2.1.6.

$$l_{hyb}^{str} = 1.7 \times l_{hyb} \tag{2.1.3}$$

$$s = l_{hyb}^{str} - l_{hyb} \tag{2.1.4}$$

$$y = \sqrt{{r_{part}}^2 - \left(r_{part} - \frac{s}{2}\right)^2} \tag{2.1.5}$$

$$A = \pi y^2 \tag{2.1.6}$$

In relating s to the contact zone diameter, it is assumed that the midpoint of all duplexes will fall equidistant from both particle surface, and therefore half the total stretching, or $s/2$, will fall on either side of this midpoint. Equation 2.1.5 is therefore used to calculate the contact zone radius, y. The circular contact area is then calculated in equation 2.1.6, and duplex data from flow cytometry is used to determine the maximum possible number of strands present within this area that can participate in hybridization – assuming that conditions for a maximum surface density from flow cytometry (closely) corresponds to a saturated number of surface-bound probes. To determine the number of duplexes that are actually formed during aggregation, an equivalent approach is used, but surface densities

from the base-pair overlaps used for aggregation experiments (**B10**) are used (for reasons explained below).

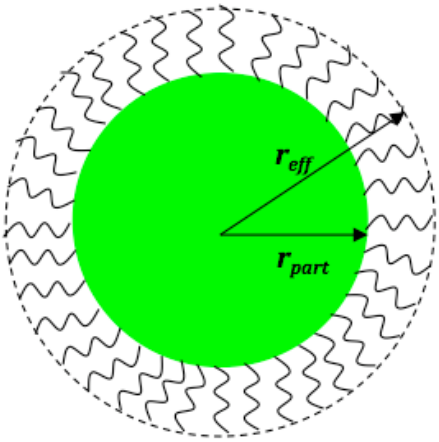

Figure 2.1.3 - Schematic of volumetric shell surrounding microsphere due to immobilized single-stranded oligonucleotide layer. The radius of the particle, r_{part}, and the effective radius due to this layer, r_{eff}, are both illustrated. The volumetric shell of interest is shown filled with single-stranded oligonucleotide rods.

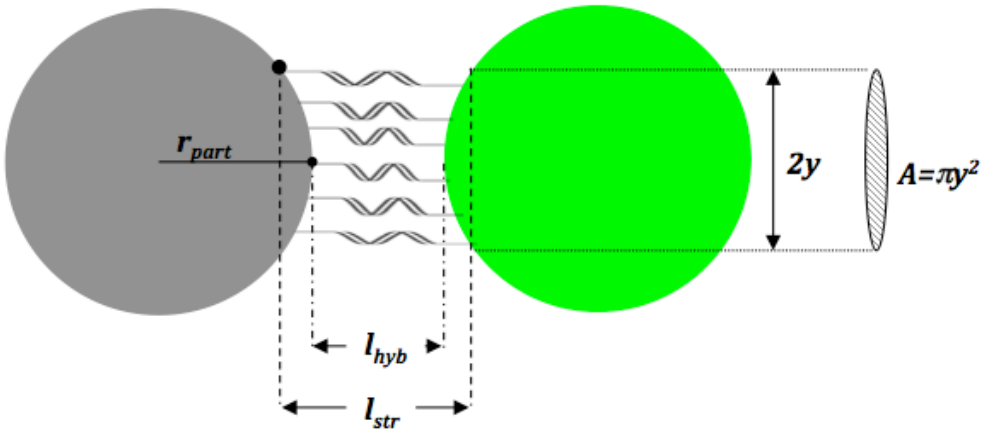

Figure 2.1.4 - Schematic illustrating our approach to calculate the contact zone area, A, between two curved surfaces. It is assumed that the distance between surfaces at their nearest points is equivalent to the length of a hybridized duplex, l_{hyb}. The furthest point at which hybridization can occur is equivalent to the stretched length of duplex DNA, l_{str}, which is equal to 1.7 times l_{hyb}. This results in a radius of y for the contact zone area.

2.1.5 - Particle Aggregation and Image Analysis

Confocal microscopy (Zeiss LSM 510) was used to investigate the ability of DNA-functionalized microspheres to reversibly assemble or aggregate. For 1.04 μm aggregation experiments, a phosphate buffered solution with 0.2% bovine serum albumin (PBS/BSA) solution was prepared by first dissolving BSA in PBS, heating the solution in a water bath for 45 minutes at 57.5°C to denature the BSA protein, and then filtering the solution through a 0.2 μm syringe tip filter to remove large BSA aggregates and debris. Separate suspensions of fluorescent and nonfluorescent microspheres were re-suspended in PBS/BSA at a total initial volume fraction of 10^{-3}. To prepare sample chambers for aggregation experiments, 20 μL wells were formed using Mμlti* Hybridization Slides (Sorenson Bioscience) which possess an adhesive top and bottom. Within the well, 10 μL of PBS/BSA is added, and allowed to coat the surface for 10 minutes to help prevent nonspecific adhesion of particles to the glass slide surface. In a separate 0.5 mL centrifuge tube, 2.0 μL of each microsphere suspension (the 5.0 μm particles were used for select assembly experiments) are added to 11.0 μL of PBS/BSA. This 15.0 μL suspension is briefly centrifuged to consolidate the suspension, sonicated to disperse the microspheres, and then added to the hybridization well resulting in a 25.0 μL total volume suspension on the slide. A glass cover slip is mounted on top forming a tightly sealed well that minimizes evaporation. All samples are incubated at room temperature for 24 hours and then imaged. DIC mode is used to investigate morphology and phase transitions of the suspensions associated with primary and secondary hybridization events. Confocal microscopy was used to investigate specificity of aggregation. A minimum of two different samples is tested for each case to confirm results.

For aggregation/assembly involving bidisperse colloidal particle suspensions, the following assembly protocol is performed. 5.0 μL of 5.01 μm particles at 0.01% immobilized with **A20** are incubated with an excess (25 μL, 0.01%) of **B20** immobilized red fluorescent particles of 1.0 or 200 nm diameter. 70 μL of PBS/ buffer is added to dilute the solution and allow efficient mixing during incubation. PBS/BSA is not needed in this situation, as assembly is occurring in a mixable centrifuge tube not on a glass slide (where sticking and particle sedimentation are issues). Samples are incubated for 48 hours on a rotomixer at low speed. The suspension is the washed up to 8 times at speeds capable of removing the assembled colloidal micelles from suspension, while leaving the excess satellite particles suspended. As all 5 μm template particles are removed (as singlets or assemblies colloidal micelles), the particles are resuspended to 50 μL PBS/, resulting in a 0.01% suspension. The samples are imaged as discussed above.

2.2 - Results and Discussion

2.2.1 – Optimizing Coupling and Hybridization Protocols

In order to optimize the EDAC coupling procedure developed initially by Bang's Labs for coupling proteins to carboxylated particles, we investigated several variables in the DNA coupling procedure. These variables included the amount of EDAC linking agent added and the concentration and amount of probe **A20** DNA used. To quantify the changing number of surface-immobilized probes, we selected a 14 base long fluorescently labeled primary target, **B14/FITC**, to test and measure hybridization activity using flow cytometry. Following coupling with **A20** probes, the different particle

populations were incubated for 24 hours with the **B14/FITC** target. Flow cytometry was run on the samples and a surface density of hybridized targets was calculated. Because we used the same target for all samples, we attribute any changes in the surface density to changes in the number of immobilized probes.

The effect of coupling time on the surface density of hybridized targets was not investigated. All coupling is performed in 100 μL aliquots of particles at 0.1% loading. Previous research showed that approximately 90 minutes was required for the coupling reaction to come to equilibrium *(8)*. As EDAC is a highly reactive species in aqueous environments, longer time periods do not increase the coupled quantity of probes (or proteins). We therefore decided to use 2 hours as our standard coupling time. 90 minutes of incubation during the coupling reaction is also suggested by Bang's laboratories protocol.

After selecting two hours as the required coupling time, the amount of EDAC added during coupling was explored. To do this, we added different volumes of EDAC/HCB mixture that was mixed at 1 mg EDAC / 5μL solution ratio. The total amount of EDAC added varied from 1 mg to 20 mg. It was seen that the amount of EDAC added does not play a dramatic role, with all volumes of EDAC added resulting in approximately the same density of immobilized probe. We therefore selected the suggested amount from Bang's Labs of 5.0 mg (25.0 mL solution) EDAC for all subsequent DNA coupling to colloidal particles *(8)*.

Finally, the amount and concentration of probe DNA added is analyzed by adding a variety of different volumes and molarities of **A20** to the suspension during coupling. These experiments reveal that differences in volume and molarity do play a *slight* role in

determining the number of animated probes immobilized on the surface. Interestingly, even in cases in which the same *overall* amount of DNA is added, higher volumes at lower molarities always result in higher duplex densities for all targets tested. For example, Figure 2.2.1 shows the hybridized surface densities of various targets (along the x-axis) at different coupling conditions. It is observed that using 100 µL of **A20** at 10 µM results in higher surface densities for all targets tested than a coupling solution of 10 µL **A20** at 100 µM, though the two have the same *number* of aminated oligonucleotide strands present. Though using 100 µL at 100 µM results in slightly higher surface densities for the **B14** case, this condition is cost-prohibitive and does not pose significant benefits. For this reason, coupling will be performed using 100 µL of probe strand at 10 µM, diluted in Tris EDTA pH 7.4 to ensure an excess of DNA.

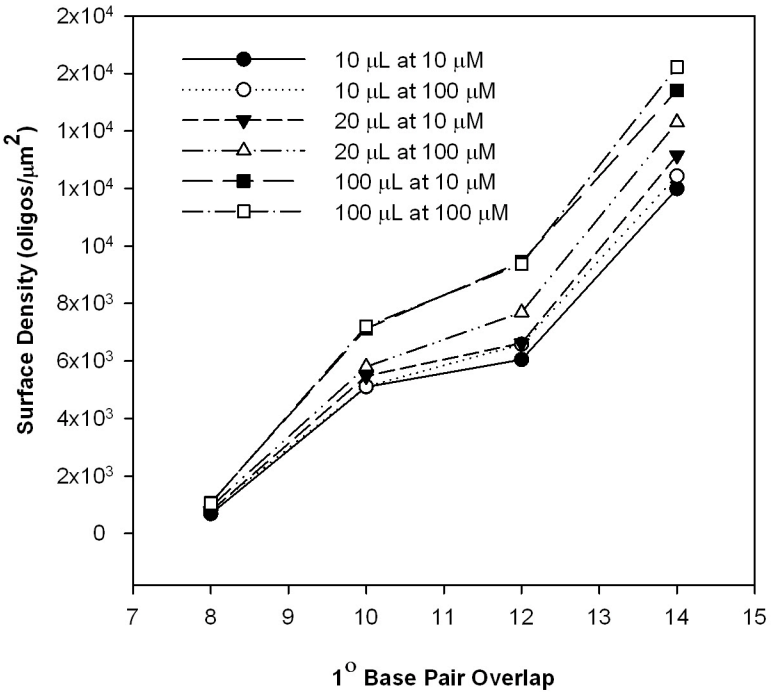

Figure 2.2.1 – Surface density of hybridized targets utilizing various amounts and concentrations of probe during coupling.

After selecting the optimal coupling conditions, we next explored the optimal hybridization time. The results for **B14** show an increased surface density over time of hybridization, up to approximately 4 hours. The surface density then plateaus, indicating that the surface has either been saturated, or FITC-labeled targets occupy all *available* probes, blocking hybridization to a certain fraction of the probes. All future hybridization experiments will be carried out with a minimum of 6 hours of primary target hybridization.

2.2.2 - Quantitative Analysis of Primary Hybridization Events on 1.04 μm Particles

The choice in sequences for DNA-mediated aggregation and redispersion of microspheres (discussed in later sections) is based upon quantitative flow cytometry analysis of primary and secondary hybridization events, respectively. A list of candidate sequences is shown in Table 2.1.1 for primary hybridization (secondary hybridization targets will be discussed in Chapter 5). Flow cytometry results for primary hybridization events between immobilized probe and soluble target sequences will be addressed first. Figure 2.2.2 and 2.2.3 show representative fluorescence histograms of nonfluorescent microspheres functionalized with **A20** probe strands and incubated with FITC-labeled target strands of varying length (or base pair overlap) with the probe sequence. The peak fluorescence intensity of probe-functionalized microspheres alone (negative) and incubated with noncomplementary target strands (negative - **NC20/FITC**) are both low and nearly identical in value in Figure 2.2.2. This close match in fluorescence intensity values indicates that fluorescence in both cases is due only to microsphere autofluorescence with negligible nonspecific association between noncomplementary target strands and either the probe strands or microsphere surface. Since the

noncomplementary target strands are identical in sequence to the probe strands, this result also indicates that affinity between neighboring probe strands on the microsphere is low. In cases involving complementary target and probe strands, however, Figure 2.2.3 shows a continuous increase in fluorescence intensity as the number of base-pair matches increases from 8 to 14. This increase or rightward shift in fluorescence intensity indicates an increasing number of fluorescently labeled oligonucleotide targets associated with the DNA-functionalized microspheres. The exception to this trend is the 16 base-pair case, which possesses a lower fluorescence intensity peak value than the 14 base-pair case.

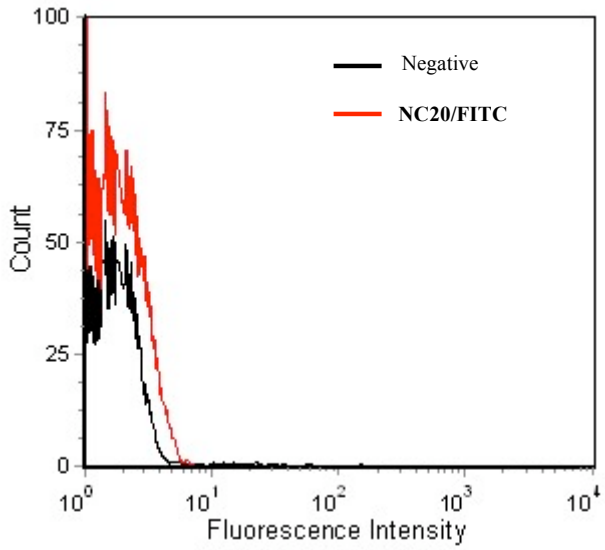

Figure 2.2.2 – Representative fluorescence histogram showing negligible target hybridization by the noncomplementary target **NC20/FITC**.

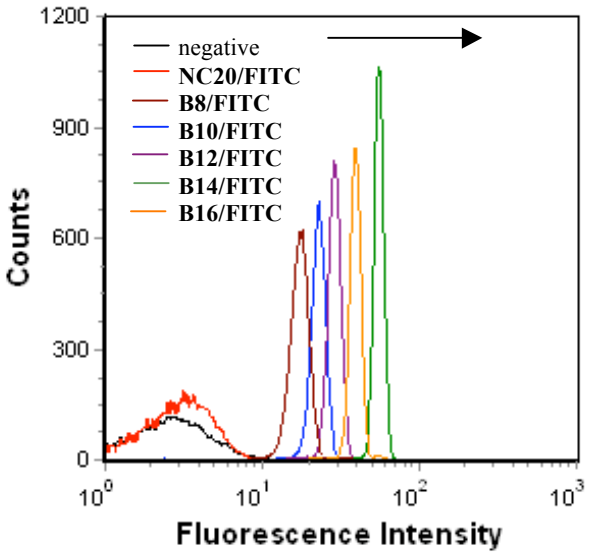

Figure 2.2.3 – Representative histogram showing increased fluorescence intensity (as indicated by the arrow) due to increased hybridization affinity as target length increases *(12)*.

Figure 2.2.4 shows quantitative analysis of hybridization activity of primary targets from multiple flow cytometry runs for each tested target. Each point is an average of four runs amongst two coupled sets, with 30,000 individual particles analyzed in the gated population for each run resulting in approximately 120,000 microspheres analyzed for each primary target case. Below 10 base pairs, hybridization activity appears very low though the calculated duplex melting temperatures for all target sequences in Table 2.1.1 exceed the room temperature conditions used for experiments. Similar to previous reports by Milam *(9, 13)*, a solution melting temperature value above the room temperature is not necessarily sufficient to cause significant hybridization activity between immobilized probes and either soluble or immobilized targets. A relatively continuous increase in density of hybridized probes strands is observed with increasing target sequence length for targets with 8-14 base-pair matches for the probe strands. This general rise in

hybridization activity with sequence length is attributed to the gradual increase in duplex affinity as indicated by the continuous increase in melting temperature (T_m) value shown in Table 2.1.1. Only a modest increase in surface density from 5,548 to 6,900 hybridized oligos/μm^2 is observed as the target length increases from 10 to 12 nucleotides. This modest difference is again predicted by the small difference in T_m value of 0.6 °C between these target lengths. The surface density of hybridized probe strands peaks at 13,661 oligos/μm^2 for the 14 base-pair case, and then drops to 9,039 oligos/μm^2 for the 16 base-pair case. Though the 16 base-pair sequence has the highest duplex affinity of all the target sequences studied, the decrease in hybridization activity for the longest target in this study is attributed to the increasing electrosteric repulsion with strand length that must be overcome for matching strands to overlap and hybridize. In addition, the short four-base spacer length may allow the particle surface to interfere with strand hybridization (these effects on DNA behavior near a particle surface will be discussed in greater detail in Chapter 4). Thus, despite the greater affinity, access to the surface-bound probes appears to become increasingly difficult as longer complementary targets are used and the drive for duplex formation is compromised. As a result, for longer targets, there appears to be a trade off between the higher affinity favoring duplex formation and the greater steric hindrance prohibiting duplex formation with probe strands immobilized on a surface. For the 8-16 base long targets shown in Table 2.1.1, this trade-off results in a peak hybridization activity for 14 base-long hybridization segments. Note that this maximum duplex density value was used to estimate the number of probe strands available for hybridization activity between microspheres.

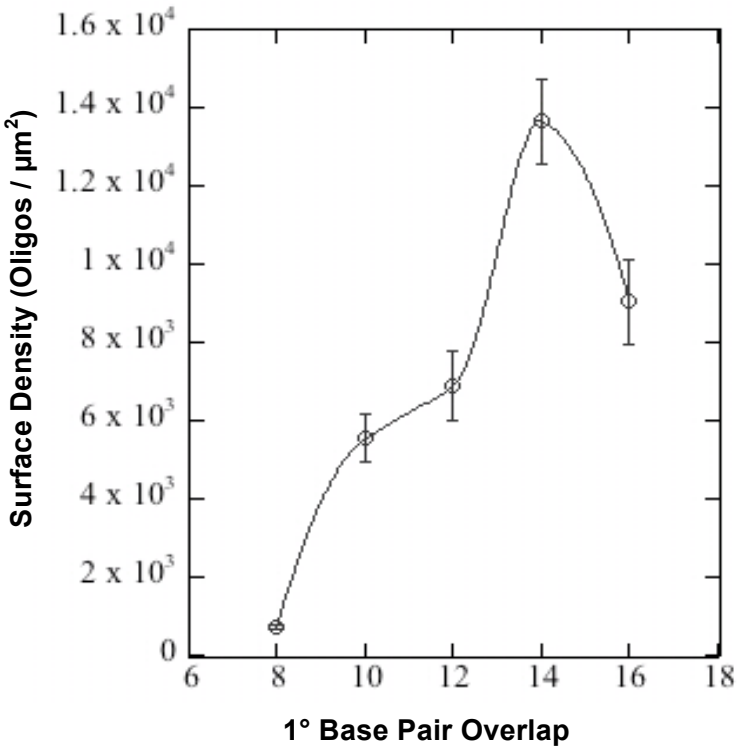

Figure 2.2.4 – Surface density of primary targets hybridized to **A20**-functionalized 1.04 μm particles as a function of base-pair matches.

2.2.3 - Quantitative Analysis of Primary Hybridization Events on 5.01 μm Particles

Identical analysis as described in section 2.2.2 was performed for primary target hybridization on the larger **A20**-functionalized 5.01 μm particles. Flow cytometry was again used to monitor the fluorescence signal associated with hybridized soluble targets on surface immobilized probes. Figure 2.2.5 shows the results for these experiments with surface density versus base-pair overlap again plotted. For comparison, this data is overlaid with the 1.04 μm data previously discussed in Figure 2.2.4. It is observed that the hybridized surface density of all targets is lower on 5.01 μm particles as compared to the 1.04 μm case. The **B14** target is again shown to have the highest hybridization

affinity, here with a surface density of approximately 2,500 oligonucleotides/μm^2. Though the surface densities on the 5.01 μm particles are indeed lower, the overall number of hybridized targets per microsphere is higher. This result corresponds with the reported parking area of carboxyl groups on the particles. The parking area describes the area occupied by each carboxyl group and is reported by the particle supplier based on titration experiments to determine the μeq/g of COOH present *(14)*. This area on the 5.01 μm particle is 44.5 $Å^2$, which is significantly larger than 9.0 $Å^2$ on the 1.04 μm particles. This means that oligonucleotide strands should be immobilized at decreased densities on the 5.01 μm particles, which is confirmed by our results. Further, the decreased duplex density on the 5.01 μm particles should result in more efficient hybridization with the 16 base-long target.

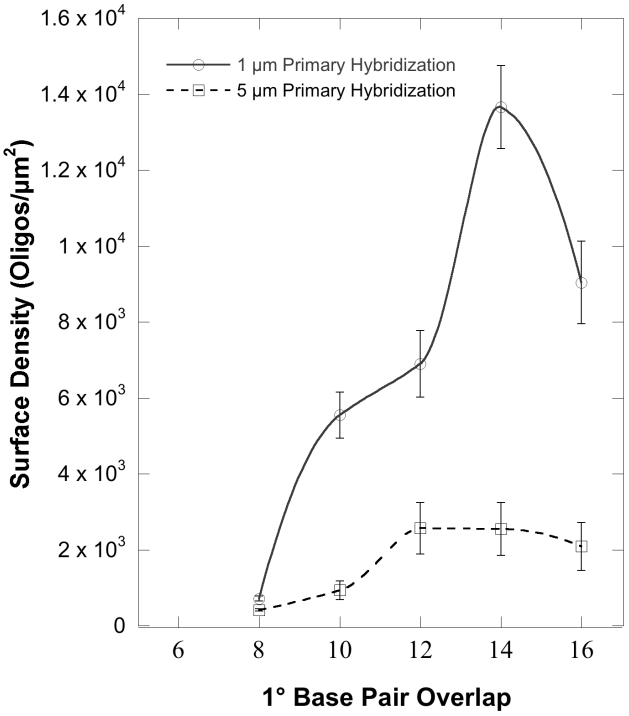

Figure 2.2.5 – Surface density of various length primary targets hybridized to **A20** probes immobilized on 1.04 μm or 5.01 μm particle surfaces.

2.2.4 - Colloidal Aggregation via Primary Hybridization Events

As the ultimate goal of this study is to induce the reversible adhesion of DNA-linked microspheres, we wish to select a duplex system with weak but sufficient affinity to drive complete, but ultimately reversible, colloidal aggregation via primary hybridization events. Based on flow cytometry results, the 10 base-pair target is the shortest sequence exhibiting significant hybridization activity on both 1.04 and 5.01 μm particles and was thus selected for subsequent colloidal aggregation studies. For aggregation experiments to mimic the length of the immobilized **A20** probe strands, the immobilized hybridization partner **B20** is comprised of a 10 base-long thymine spacer and a 10 base-long hybridization segment identical in sequence to the soluble strand **B10**.

To calculate the maximum number of linkages between pairs of 1.04 μm microspheres functionalized with **A20** and **B20** respectively, the geometric approach reported by Biancaniello and discussed in 2.1.4 was used *(9)*. The calculated contact area of 0.0034 μm^2 between the curved surfaces of 1.04 μm spheres containing **A20**:**B20** duplex linkages contains approximately 46 **A20** probe strands in the contact zone as shown in Table 2.2.1. For the 10 base-pair case involving approximately half of the probe strands in hybridization activity, this means the calculated maximum number of duplexes present in the contact area between two spheres is approximately 19. Subsequent studies in Chapter 4 explore reducing the number of strands in the contact area that participate in hybridization events.

Table 2.2.1 – Estimates of probe concentration (in the volumetric "shell" of grafted DNA on particles), probe number in the contact zone, **A20**:**B10** duplexes in the contact zone, and the theoretical melting temperature as calculated using Biancaniello's approach *(9)*. The maximum number of **A20** probe strands is calculated from flow cytometry data with **B14** and the maximum number of duplexes from flow cytometry data involving **B10** targets. The melting temperature is determined as previously described.

percent **A20** probe strands	molar concentration of **A20** probe strands	maximum number of **A20** probe strands in contact area	maximum number of **A20** duplexes with 10 base-long target	T_m
100%	2.140 nM	46	19	72.0 °C

DNA-mediated aggregation between complementary microspheres containing 10 base-pair matches is schematically illustrated in Figure 2.2.6. Unlike flow cytometry that employed soluble target strands, aggregation involves only surface-immobilized strands.

Experiments were performed to determine the ability of 10 base-long duplexes to induce complete DNA-mediated aggregation via primary hybridization events. First, control samples were run using mixtures of **B20** probe-functionalized microspheres and microspheres functionalized with only **T20**, the noncomplementary sequence of 20 thymine nucleotides. As shown in Figure 2.2.7(a), the suspension consisted almost entirely of dispersed microspheres with only a few dimers present after 24 hours. The lack of colloidal clusters in this case indicates that nonspecific attractions do not drive colloidal aggregation. Figures 2.2.7(b and c) show the results of including only **A20** or only **B20** particles in a homogenous suspension. Again, only singlets are observed, indicating that hybridization between identical sequences is negligible, and aggregation due to nonspecific interactions (i.e., vdW) does not occur. Figure 2.2.7(d) shows the results of incubating **B20**-functionalized microspheres with microspheres functionalized with the complementary **A20** strands that possess a 10 base-long overlap. It is observed that after 24 hours of mixing under static conditions, large, fractal like colloidal aggregates are formed. These aggregates can be seen with the naked eye.

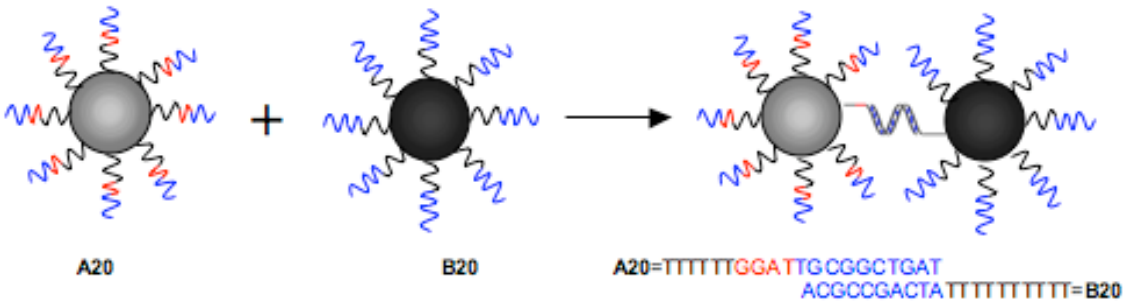

Figure 2.2.6 – Schematic of DNA-mediated colloidal aggregation showing hybridization between a 10 base-long complementary segment (shown in blue) *(12)*. For simplicity, only one duplex is shown though many duplexes are estimated to occur as shown in Table 2.2.1.

To further characterize the specificity of the binding, a binary colloidal structure was formed using an excess of **B20**-functionalized 200 nm red fluorescent particles and **A20** functionalized 5.01 µm non-fluorescent particles. Figure 2.2.8 shows representative micrographs of this system. Because of the size difference, the specificity of the system is more evident, as a ring of 200 nm particles is seen to adhere to the surface of the 5.01 µm template particle. When non-complementary **T20** oligonucleotides are immobilized on the 200 nm particle as seen in Figure 2.2.8(a), no satellite structures are formed. These results, combined, show that the 10 base-long hybridizing segments is indeed sufficient to drive the programmed aggregation of 1.04 µm particles or the assembly of colloidal satellites comprised of 5.01 µm (core) particles with either 200 nm or 1.04 µm (shell) particles.

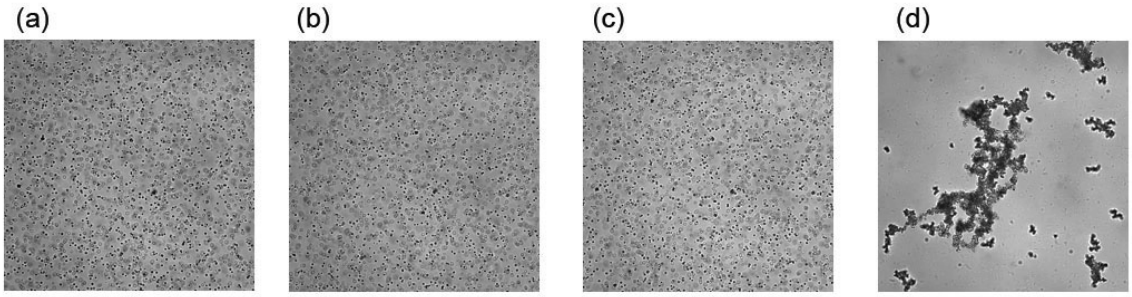

Figure 2.2.7 – Representative confocal micrographs taken at 40x in phase-contrast mode showing DNA-mediated particle aggregation. Aggregation is negligible for (a) non-complementary suspensions of **A20** and **T20**-functionalized particles and homogeneous suspensions of (b) **A20** and (c) **B20**-functionalized particles. Suspension of complementary particles in (d), however, resulted in significant aggregation.

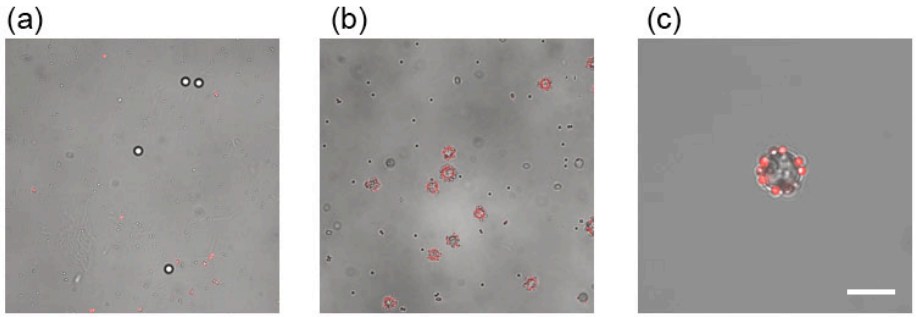

Figure 2.2.8 – Representative confocal micrographs at 63x (a, b) or 63x with zoom (c) illustrating DNA-mediated assembly for satellite structures. Incubation of **A20**-functionalized 5.01 μm template particles with noncomplementary 200 nm shell particles (a) shows no specific aggregation. When template particles are incubated with complementary shell particles (b, c), aggregation is observed and satellite structures are formed. Scale bar in (c) is 5.0 μm.

2.3 – Conclusions

Combined, the results from coupling and primary hybridization experiments reveal that DNA-linkages can be used to drive recognition-based aggregation or assembly of polystyrene microspheres. An optimized coupling procedure has been developed for linking aminated **A20** probes to the surface of particles, using 5 mg of EDAC and 2 hours of coupling time. A 10 base-long hybridization segment is shown to be sufficient both to drive modest soluble target hybridization, as well as the DNA-mediated assembly of aggregate structures. Again, as we wish to generate a weakly adherent assembly, the 10 base-long duplex is chosen. Combined, this chapter introduced the coupling and primary hybridization conditions required for inducing moderate hybridization behavior for both soluble and immobilized targets. In the next two chapters, we further explore the tuning of particle aggregation by introducing diluent strands that will serve to minimize the number of 10 base-long duplexes that can exist between particle surfaces.

References

1. Du, S.M., Zhang, S., and Seeman, N.C. *Biochemistry*, **1992**. *31*. 10955-63.

2. Zuker, M. *Nucleic Acids Res.*, **2003**. *31*. 3406-15.

3. Zuker, M. *Mfold Web Server*. **2003**; Accessed 12/01/2006. Available from: http://mfold.bioinfo.rpi.edu/.

4. Biancaniello, P.L., Kim, A.J., and Crocker, J.C. *Phys. Rev. Lett.*, **2005**. *94*. 058302.

5. Ivanova, E.P., Papiernik, M., Oliveira, A., Sbarski, I., Smekal, T., Grodzinski, P., and Nicolau, D.V. *Smart Materials and Structures*, **2002**. *11*. 783-91.

6. Lund, V., Schmid, R., Rickwood, D., and Hornes, E. *Nucleic Acids Res.*, **1988**. *16*. 10861-80.

7. IDT. *SciTools Oligo Analyzer*. **2009**; Accessed 12/11/2006. Available from: http://www.idtdna.com/analyzer/Applications/OligoAnalyzer/.

8. *PolyLink Protein Coupling Kit for COOH Microspheres*, I. Bangs Laboratories, Editor. 2007: Fishers, IN.

9. Biancaniello, P.L., Crocker, J.C., Hammer, D.A., and Milam, V.T. *Langmuir*, **2007**. *23*. 2688-93.

10. Calladine, C.R., Drew, H.R., Luisi, B.F., and Travers, A.A., *Understanding DNA: The Molecule and How it Works*. Third ed. 2004, San Diego: Elsevier Academic Press. 334.

11. Cluzel, P., Lebrun, A., Heller, C., Lavery, R., Viovy, J.L., Chatenay, D., and Caron, F. *Science*, **1996**. *271*. 792-4.

12. Tison, C.K. and Milam, V.T. *Langmuir*, **2007**. *23*. 9728-36.

13. Milam, V.T., Hiddessen, A.L., Crocker, J.C., Graves, D.J., and Hammer, D.A. *Langmuir*, **2003**. *19*. 10317-23.

14. Whybrew, J. "GA1108/GaTech/Tison - Covalent Coupling." Email to C.K. Tison. 11/08/2005

CHAPTER 3

Employing Diluent Strands to Titrate the Number of DNA Linkages between Colloidal Particles

As determined in the previous chapter, a ten base-long linking duplex between complementary particles is sufficient to induce DNA-mediated adhesion for 1.04 μm red fluorescent/nonfluorescent, 5.0 μm/1.04 μm, and 5.0 μm/200 nm mixtures of complementary colloidal particles. Since the ultimate goal is redispersion or disassembly of these DNA-linked colloidal particles under isothermal conditions, we wish to aggregate particles with the minimum avidity (or, number of duplexes) required. In this chapter, diluent surface strands are investigated to decrease the number of **A20** probes immobilized on one particle population. These diluent strands decrease the number of linkages possible between complementary particles, and thus may serve to increase the efficiency of particle redispersion. Here, two different diluent strands will be investigated; **T20**, a 20 base-long strand of equivalent length to the **A20** probe, and **T10**, a 10 base-long strand half the length of **A20**. The shorter **T10** strand is used to elucidate the effect of electrosteric repulsion on DNA-mediated aggregation. By titrating the ratio of **A20/T20** or **A20/T10**, phase transitions are observed in mixtures of 1.04 μm particles, and the critical concentration of **A20** probe required for aggregation is determined. Studies with labeled targets (complementary only to **A20** probe strands) allow us to measure the density of **A20**-based duplexes at varying diluent-to-probe strand ratios and relate these density values to the experimentally determined phase transitions.

3.1 – Experimental Setup

3.1.1 - Oligonucleotide Selection

Aminated and FITC-labeled strands are purchased, aliquoted, and stored as described in 2.1.1. Soluble **B10** and **B14** FITC-labeled targets are used for flow cytometry experiments in order to measure the surface duplex density and compare the affinity of targets for immobilized **A20** probes. Probes and diluent strands are simultaneously immobilized on particle surfaces using EDAC-based conjugation as detailed in Chapter 2. Multiple copies of an identical sequence (**A20** or **B20**) are immobilized on one of two populations of microspheres for aggregation experiments. Diluent strands labeled as **T20** or **T10** are either equal in sequence base length (**T20**) or half the base length (**T10**) of **A20** and **B20.** These diluent strands are not complementary to either **A20** or **B20**. These nonhybridizing strands are intended to dilute the concentration of **A20** immobilized on one population of microspheres.

3.1.2 - Particle Preparation

Nonfluorescent 1.04 μm and 5.01 μm carboxylated polystyrene particles (Bangs Laboratories) and 1.1 μm and 200 nm red fluorescent carboxylated polystyrene particles (Molecular Probes) were used for aggregation experiments involving mixtures of hybridizing and diluent strands. The carboxyl surface functionality again allows for covalent EDAC coupling of aminated probe and diluent strands to all colloidal particle surfaces. As opposed to the **A20** immobilized particles in Chapter 2, the non-fluorescent particles are now immobilized with mixtures of **A20** probes and either **T20** or **T10** diluent strands at varying ratios. To control the ratio of diluent to probe strands, the DNA

is mixed in specific ratios prior to coupling. The large 5.01 μm colloidal particles were similarly prepared with varying probe to diluent ratios. The red fluorescent particles (200 nm and 1.04 μm) are immobilized with 100% **B20** probes, complementary to the **A20**. Following conjugation, particles are resuspended in 100 μL of PBS/Tween buffer for storage as a 0.01 volume fraction suspension.

3.1.3 - Flow Cytometry to Investigate Primary Hybridization

Flow cytometry studies on probe/diluent strand-functionalized particles incubated with either **B10** or **B14** FITC-labeled targets are carried out in a similar manner as described in 2.1.3. Again, two sets of two coupled batches are investigated, for a total of four samples at each loading. Surface density results are plotted as an average surface density over each of the four runs with error as the standard deviation. Two negative controls (**A20** or **A20**/diluent-functionalized particles alone and incubated with FITC-labeled noncomplementary targets) are included and surface densities are again determined using Bang's MESF FITC Medium standards. For the diluent strand cases investigated here, only 10 and 14 base-long targets are used to investigate the surface density of hybridized **A20** probes. The 10 base-long targets were selected for their modest hybridization activity with **A20** that promotes DNA-mediated particle aggregation and assembly (as described in Chapter 2). The 14 base-long targets were selected for the greatest hybridization activity (of the 8 to 16 base-long targets studied) as described in Chapter 2.2.2.

3.1.4 - Particle Aggregation, Duplex Calculations, and Image Analysis of Phase Transitions

Confocal microscopy is used to investigate the phase transitions as microspheres functionalized with varying ratios of **A20** to **T20** or **T10** are mixed with **B20**-functionalized particles. Suspension samples are prepared as described in 2.1.5, and again mixed for 24 hours. DIC mode is used to investigate the resultant morphology and phase transitions, while fluorescence mode is used to again confirm that heterogeneous aggregation between complementary particles occurs. Phase transitions are qualitatively described by comparing the extent of aggregation, if any, and the presence of singlets or dispersed particles at each loading ratio. The nomenclature for the phases is as follows: a fluid consists only of dispersed particles; fluid + aggregates consist of a mixture of singlets and clusters; aggregates consist only of clusters of particles. At least two samples (from two different coupled batches) are run to confirm all qualitative observations.

To calculate the number of duplexes present between particle surfaces at each **A20** loading, calculations are performed as described in 2.1.4. Particles functionalized with 100% **A20** (no diluent strands) and hybridized to **B14** targets exhibited the highest duplex densities and are thus used to determine the maximum number of **A20** probes that may exist in the contact zone between particles. Particles functionalized with mixtures of diluent strands and **A20**:**B10** duplexes are used to determine the range in value of 10 base-long linkages that may form in the contact zone between particles. Combined with aggregation experiments, these density values are then correlated with the critical concentration (***C**** and ***C*****) of duplexes required for inducing key phase transitions.

3.2 - Soluble Target Hybridization on Diluent Strand Titrated Surfaces

3.2.1 - Quantitative Analysis of Soluble Targets on T20 Diluent Strand-Titrated Surfaces

In addition to selecting the shortest sequence for which modest, but sufficient, hybridization activity occurs, it is possible to further tune the net attraction between DNA-linked particles by decreasing the number of duplex linkages holding particles together. Previous studies have shown that it is possible to reduce the number of DNA linkages between surfaces by titrating the particle surface with nonsense (i.e., noncomplementary) sequences or short PEG strands while still maintaining sufficient hybridization activity between complementary strands to drive DNA-mediated colloidal aggregation *(1, 2)*. Further, several groups have determined that changing surface densities of probes on planar surfaces greatly affects the kinetics and extent of target hybridization as well as the specificity of target capture *(3, 4)*. Here, diluent strands are used to reduce the number of linking duplexes for the purpose of reducing the avidity between particles. Quantitative flow cytometry analysis was used to determine whether the number of **A20** probe strands could be reduced in a controlled manner using **T20** or **T10** diluent strands as lateral spacers on the microsphere surface. The diluent strands are 10 or 20 base-long thymine (dT) strands that are either equal base length (and similar molecular weight) to the active **A20** probe (**T20**) or half the length and molecular weight of the active **A20** probe (**T10**). After incubating bare (i.e. carboxylated) microspheres with a fixed molar percentage ratio of **T20** or **T10** and **A20**, the hybridization activity of the microspheres with soluble, FITC-labeled **B10/FITC** and **B14/FITC** targets was then

quantified. The **T20** equivalent length case will be discussed first. Figure 3.2.1 and 3.2.2 show histograms for the **B10** and **B14** targets, respectively, in which an increase in fluorescence intensity (along the x-axis) occurs as the ratio of **A20** to **T20** increases (these histograms show one of the four tested sets). This trend indicates hybridization increasingly occurs on surfaces with increasing percentage **A20**. The quantitative results are plotted in Figure 3.2.3 using x- and y-axes of equivalent scale in order to check the correlation between the percentage of **A20** in the initial oligonucleotide mixture and after immobilization to the nonfluorescent microspheres. For microspheres functionalized with 0% **A20** (and therefore 100% **T20**) no hybridization activity is observed with the **B10/FITC** and **B14/FITC** soluble target. As the ratio of hybridizing **A20** probe is incrementally increased to 100%, an approximately linear increase in the surface density of probes hybridized to either **B10/FITC** or **B14/FITC** target is observed, reaching its maximum of approximately 5,500 and 13,000 oligos/μm^2 respectively at 100% **A20**. Here, linear curve fits are used **only** to illustrate the general trend in behavior and for comparison to results in the following chapters. The dependence of fluorescence intensity on the percentage of **A20** for both targets, especially at high **A20** percentages, also demonstrates that no fluorescence quenching between neighboring duplexes occurs.

Interestingly, the **B10** case appears to show a "lag" in surface density at low **A20** probe loadings. For these cases, the surface density of the **B10** primary targets is slightly *lower* than would be predicted on the nearly linear behavior of **B14**. This lag may be explained by the probability of collision between targets and the complementary **A20** probe. As the number of **A20** probes decreases (and the number of equivalent length **T20** diluent strands increases), the hybridization time may need to be increased to account for

decreased probability of target collision with complementary probes. The longer, higher affinity **B14** targets may not require this increase in hybridization time due to the increased binding affinity. Further elucidation of this unexpected trend warrants more experiments involving, for example, spacers of varying base-length and particles with lower *total* DNA densities (i.e., lower COOH densities to allow for greater lateral spacing between neighboring, immobilized DNA strands). These additional experiments, however, are beyond the scope of the current study.

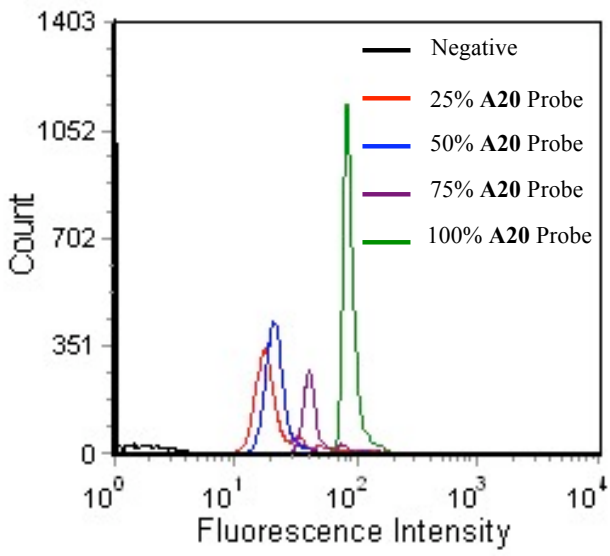

Figure 3.2.1 – Representative fluorescence for particles functionalized with varying percentages of **A20** and **T20** and then incubated with **B10/FITC** targets.

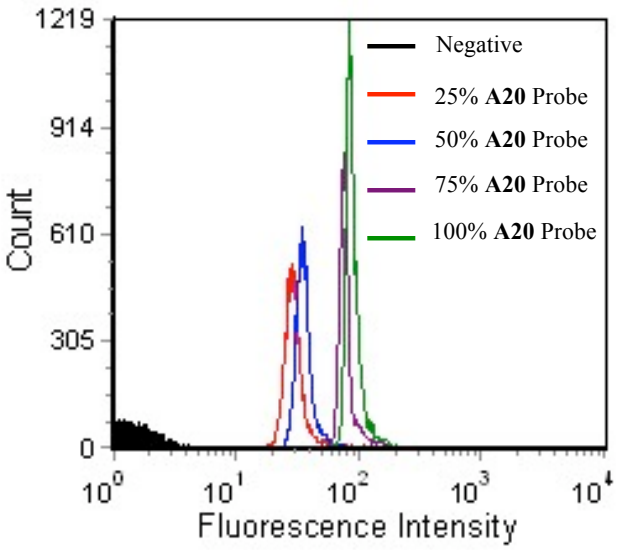

Figure 3.2.2 - Representative fluorescence for particles functionalized with varying percentages of **A20** and **T20** and then incubated with **B14/FITC** targets.

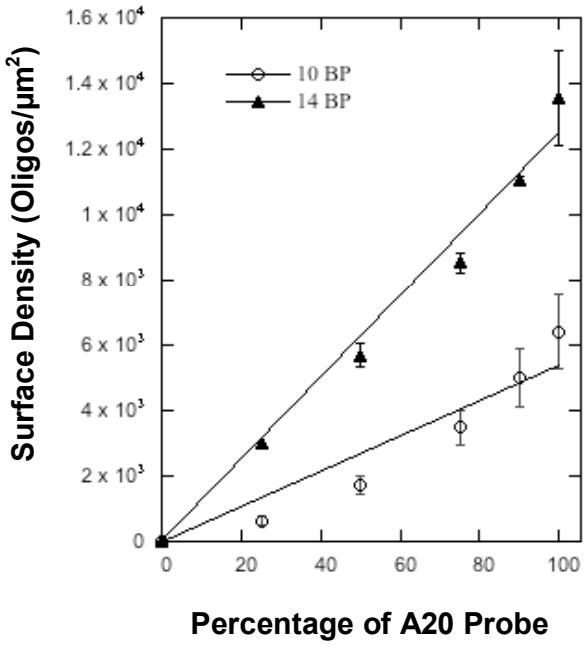

Figure 3.2.3 - Surface density of immobilized **A20** probe strands hybridized to targets **B10/FITC** or **B14/FITC** at varying percentages of **A20**. The concentration of **A20** on the microspheres was titrated using non-hybridizing diluent strand **T20** *(5)*.

3.2.2 - Quantitative Analysis of Soluble Targets on T10 Diluent Strand-Titrated Surfaces

After characterizing the primary target hybridization activity with **A20/T20**-functionalized surfaces, we investigated the behavior of the **A20/T10** system. **T10** is a thymine oligonucleotide that is half the length of the 20 base-long **A20** probe. Since we wish to drive the disassembly of these structures using secondary target hybridization in subsequent studies, we originally hypothesized that using shorter diluent strands may allow greater access for secondary targets or may even further reduce the critical number of duplexes required to cause DNA-mediated aggregation. In this section, we first investigate the effect shorter diluent strands have on primary hybridization activity. To analyze the hybridization activity of **B10** or **B14** targets to **A20** probes on **T10** diluent strand surfaces, flow cytometry was again performed as for the **T20** case in 3.2.1. Controls show negligible hybridization of either **B10** or **B14** on surfaces immobilized with 100% **T10**, indicating that hybridization activity is restricted to the **A20** probe strands. Histograms again show increased fluorescence intensity as the ratio of **A20** to **T10** increases. To facilitate comparison amongst the **T20** and **T10** cases, we compare the measured duplex densities for the **T10** cases with that of the **T20** cases by plotting them on the same graph. Figure 3.2.4 shows the surface density of **A20** probes hybridized to FITC-labeled targets as a function of initial **A20** loading. In general, a larger number of duplexes form with longer **B14** targets than with shorter **B10** targets at a given **A20** loading. The overall increase in density of hybridized **A20** strands with probe loading indicates that simultaneous coupling of probe strands with either **T20** or **T10** strands does affect the resulting hybridization activity of the microspheres as seen in 3.2.1. As

compared to the **T20** case, however, a significantly different hybridization behavior and deviation from linearity is observed for the **T10** case. Below 25% **A20** loading, a sharper increase in hybridization activity of **A20** with loading is observed for the **A20/T10** system compared to the **A20/T20** system. At probe loadings of 25% or more, the number of **A20**:**B10** duplexes in the **T10** system remains relatively constant, matching that of the 100% loading case. For the **B14** target, a relatively fixed number of duplexes form at probe loadings of 20-80%, but does not match the highest number of duplexes formed for the 100% **A20** case. Together, results with either **B10** or **B14** targets indicate that at low probe loadings, overall higher surface densities of hybridized strands are achieved for the **A20/T10** system than for the **A20/T20** system. It is believed that the increased hybridization activity for **T10** cases involving low (initial) probe concentrations may be due to increased access of the soluble targets to the hybridization segment on the **A20** probe. Since **T10** is half the length of the probe, the hybridization segment may more easily extend past shorter neighboring diluent strands for easier target access, unlike the **T20** cases in which probes and diluent strands "stand" at comparable heights next to one another. While quantifying the number of **A20**-based duplexes is straightforward, quantifying the concentration of **T10** and **T20** strands present on the surface is experimentally difficult, however, since the length and T_m of duplexes formed with their "homopolymer" (adenine only) target can easily vary. Though quantifying the number of **T10** strands is not possible, the presence of these diluent strands shows a marked effect on the hybridization activity of **A20** with either **B10** or **B14** targets. Further, the lag in hybridization behavior observed in the **T20** case is not observed for **T10**, lending further

credence to the hypothesis that this lag is caused by a decreased probability of contact when the **T20** diluent strands dominate the surface.

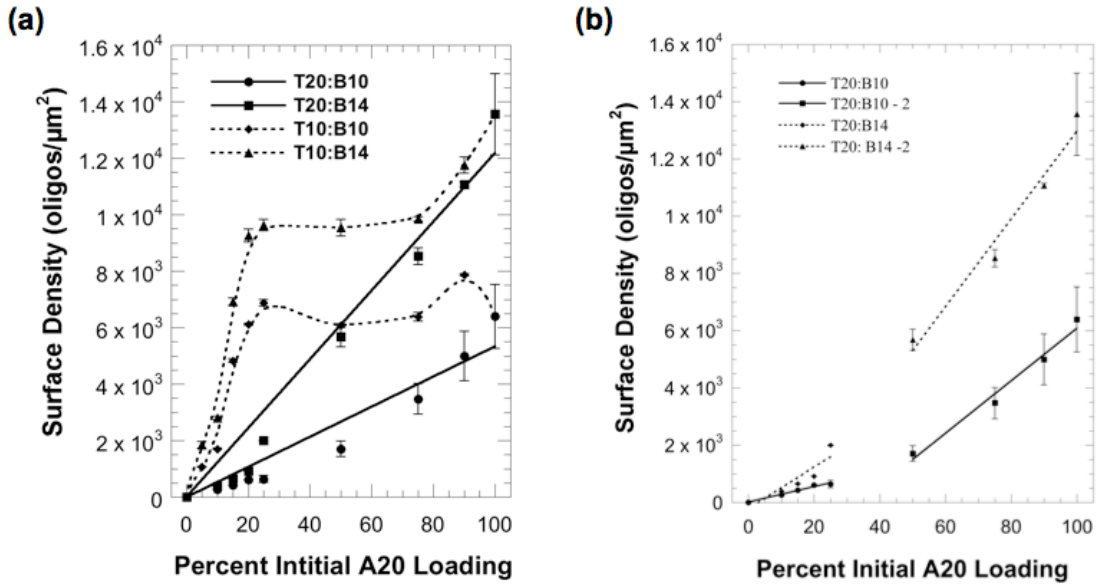

Figure 3.2.4 - Surface density of immobilized **A20** probe strands hybridized to targets **B10/FITC** or **B14/FITC** at varying concentrations of **A20**. The concentration of **A20** on the microspheres was titrated using non-hybridizing diluent strand **T20** or **T10** *(6)*. Plot (A) shows a strictly linear fit for the two **T20** cases. Dotted lines for both **T10** cases are intended only to serve as guidelines for each set. Plot (B) shows a linear fit for two ranges (low and high) of **A20** for **T20:B10** and **T20:B14** only.

3.2.3 - Discussion of Target Hybridization on Surfaces with Diluent Strands

As compared to primary hybridization studies presented in Chapter 2, the differences in hybridization activity of **B10** and **B14** with **A20** can now arise both from affinity differences between the two targets as well as differences in the accessibility of the probes to the targets (due to the neighboring diluent strands). The resulting

hybridization activity of the soluble targets is therefore a balance between the number of **A20** probes present on the surface, the availability of these probes to the target species, and the affinity of the targets for the probe. As the surface is likely to be nearly saturated with shorter **T10** strands at low **A20** loadings, the reduced steric interference of these diluent strands appears to enhance the ability of the targets to find and hybridize to probes resulting in elevated hybridization activity compared to the **A20/T20** system. As the initial **A20** loading increases, the plateau in hybridization activity may be due to negligible changes in the immobilized probe concentration. Alternatively, if the effective probe density does increase with initial probe loading, the longer, and more numerous, probes may sterically inhibit additional hybridization events. Regardless of the reason for this shift in hybridization activity, the data indicates that maintaining a one-to-one correlation between the initial (prior to immobilization) and final (following immobilization) ratio of different sequences is difficult unless the probe and diluent sequences are identical in length. For this reason, we will explore first coupling diluent probe strands of equivalent length and then clipping the diluent strands using a restriction enzyme in Chapter 4. This approach will better preserve the 1:1 correlation before and after coupling, while still allowing us to explore the effect of shorter diluent strands on hybridization and aggregation. We first investigate the effects of **T20** and **T10** on aggregation in the following section.

3.3 - Particle Aggregation and Phase Transition Analysis

3.3.1 - T20 Diluent Strand Aggregation and Phase Transitions

Aggregation experiments were carried out with **T20** as the diluent strand to determine the minimum concentration of **A20** probes required to drive DNA-mediated aggregation to completion via primary hybridization events. First, control samples were run using mixtures of **B20** probe-functionalized microspheres and microspheres functionalized with only **T20**. As shown in Figure 3.3.1, the suspension consisted entirely of dispersed microspheres with only a few dimers present after 24 hours incubation. The lack of colloidal clusters in this case indicates that nonspecific attractions do not drive colloidal aggregation, and that **T20** as a diluent strand should not participate in binding to **B20** to cause aggregation. Figure 3.3.2 (a-e) shows the effect of increasing the **A20** probe surface density on the propensity for microspheres to aggregate. Below 15% **A20**, a fluid phase consisting of dispersed microspheres with only occasional small aggregates is found, even after 24 hours. As shown in Table 3.3.1, the maximum number of DNA duplexes that can be present within the contact area between two microspheres is calculated to be less than three for the 15% **A20** case. As the surface density of **A20** is increased to 20%, a phase transition is evident in which dispersed microspheres and small clusters of microspheres coexist in a dual fluid + aggregates phase region. The minimum or critical probe concentration to induce the fluid to fluid + aggregates phase transition occurs between 15 and 20% **A20** and is indicated by ***C**** in Figure 3.3.2. The calculated number of DNA duplexes present in the contact area for 15% **A20** is three, increasing to four at 20% **A20** (Table 3.3.1). As the probe concentration is increased to 25%, a second

phase transition occurs in which only aggregates are observed (These transitions are analyzed quantitatively in Appendix B using mean gray intensity analysis).

Table 3.3.1 – Table of oligonucleotide concentrations and duplex numbers between particle surfaces as calculated using Biancaniello's approach *(1)*. The maximum number of **A20** probe strands is calculated from flow cytometry data involving the **B14** target and the maximum number of duplexes formed between particles is calculated from flow cytometry data involving **B10** targets. The melting temperature is determined as discussed in previous chapters *(7)*, using the molar concentration calculated in column two *(5)*.

percent **A20** probe strands	molar concentration of **A20** probe strands	maximum number of **A20** probe strands in contact area	maximum number of **A20** duplexes with 10 base-long target	T_m
10%	0.214 mM	5	2	60.0 °C
15%	0.321 mM	7	3	66.0 °C
20%	0.428 mM	9	4	66.9 °C
25%	0.535 mM	12	5	67.6 °C
100%	2.140 mM	46	19	72.0 °C

The minimum or critical probe concentration to induce the fluid + aggregates to aggregates phase transition occurs between 20 and 25% **A20** and is indicated by ***C***** in Figure 3.3.2. Further, a continued increase in **A20** loading reveals larger and more fractal aggregates. This trend towards a more fractal nature is largely due to kinetically trapped structures, as complementary probes are more likely (and therefore more quickly) able to find each other and hybridize. These phase transitions allow us to select the critical or lowest **A20** surface density capable of driving DNA-mediated aggregation to completion – seen here for a ten base-pair hybridizing segment at 25% **A20** surface functionalization. For the 25% **A20** case, the calculated maximum number of DNA strands present for

hybridization between the surfaces increases to five. Thus, it appears that each phase transition differs by only one DNA duplex. As mentioned previously, flow cytometry experiments indicate a fairly linear correspondence between percent **A20** probe and surface density of hybridized **B10** targets to the probe was obtained. This indicates that titration with diluent strands does decrease the number of available complementary targets functionalized to the surface and available for hybridization and that this dilution of probe strands is responsible for the phase transitions observed. In addition, the calculated values for the maximum number of DNA duplexes present within the contact area agree well with previous reports which show that approximately three to four DNA linkages are required to induce DNA-mediated colloidal crystallization *(8, 9)* or aggregation *(1)*. Previous research on a similar system revealed that the interaction energy is simply 1 k_BT multiplied by the number of linking duplexes *(8)*. Here, clusters first appear at 15% **A20**, but 25% **A20** is the minimum needed to complete the programmed aggregation of weakly attractive microspheres via primary hybridization events. These correspond with total pair interaction potentials of approximately 4-6 k_BT for weakly adherent aggregation in our samples. Using the free energy of duplex formation, we calculate interaction energies of approximately 25 k_bT per duplex (Appendix A). However, our simplified technique does not account for electrosteric repulsions that occur. Though beyond the scope of this work, modeling of the interaction potential is desirable for future studies.

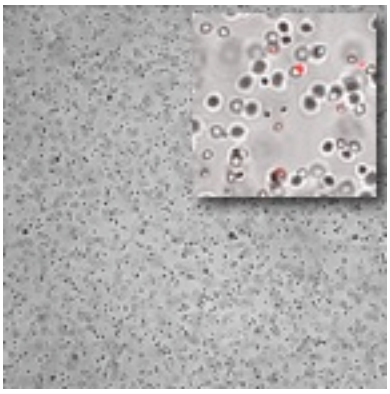

Figure 3.3.1 – Confocal micrograph at 40x reveals nonspecific binding between particles is negligible if complementary strands are not present in suspension. Here, **A20**-functionalized 1.04 μm particles are mixed with **T20**-functionalized 1.04 μm red-fluorescent particles for 24 hours.

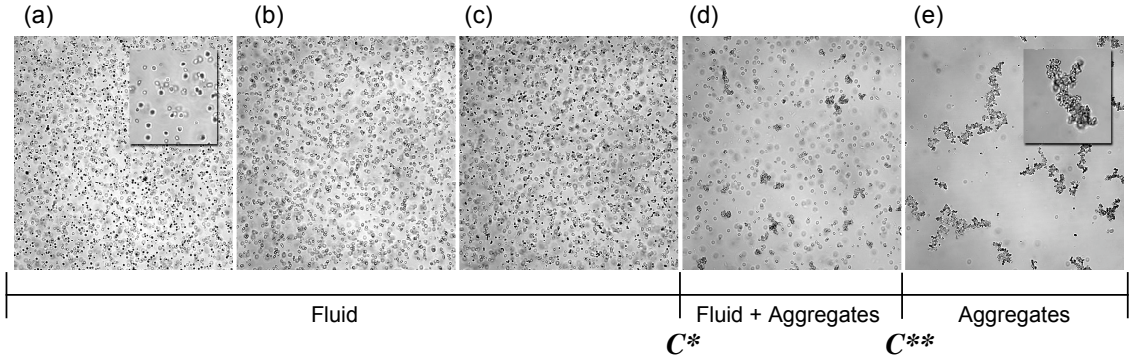

Figure 3.3.2 – Confocal micrographs taken at 40x (insets at 63x) for microsphere suspensions in which one microsphere population is functionalized with (a) 0% (b) 10% (c) 15% (d) 20% and (e) 25% **A20** strands while the other microsphere population is functionalized with 100% **B20** strands. ***C**** indicates the critical concentration of **A20** to induce a fluid to fluid + aggregates phase transition in which small aggregates and singlets are present. Below the ***C**** transition, a fluid phase exists consisting of dispersed microspheres or singlets. ***C*** indicates the fluid + aggregates to aggregates phase transition in which the suspension is primarily comprised of larger aggregates *(5)*.

3.3.2 - T10 Diluent Strand Aggregation and Phase Transitions

DNA-mediated colloidal aggregation studied with 10 base-pair overlap between complementary **A20** and **B20** strands were then carried out with the shorter **T10** diluent strand present. Control samples are first run using mixtures of **B20**-functionalized microspheres and microspheres functionalized with only the diluent strands (0% **A20**). Figure 3.3.3 shows the effect of increasing the **A20** loading in the **A20**/**T10** system. As shown in Figure 3.3.3 (a) the control sample (0% **A20**) suspensions consisted almost entirely of particle singlets (fluid phase) after 24 hours. The lack of aggregates indicates that nonspecific attractions between **T10** and **B20**-functionalized particles are negligible. At 5% **A20** (Figure 3.3.3 (b)), the fluid + aggregates phase is apparent with the suspension consisting of dispersed microsphere singlets and small clusters of microspheres. Together these micrographs indicate that the phase transition from fluid to fluid + aggregates occurs at or below 5% **A20**. At 10% **A20** (Figure 3.3.3 (c)) no dispersed microspheres are observed, and the entire suspension consists of small aggregates. Thus, the key phase transition ***C**** occurs at or below 5% **A20** and ***C**** occurs between 5% and 10% **A20**. Both of these critical probe concentrations are markedly lower for the **A20**/**T10** system than for the **A20**/**T20** system. Using the same geometric approach we employed in Chapter 2.1.4 to calculate the maximum number of duplexes between particle surfaces, we estimate that a maximum of four and six duplexes form at ***C**** and ***C**,*** respectively for the **A20**/**T10** system. The maximum number of duplexes present at the ***C**** and ***C***** for the **T10** system closely matches the values of four and five duplexes, respectively, for the **A20**/**T20** system. Thus, though the initial probe loadings to induce DNA-mediated phase transition are somewhat lower for the **A20**/**T10** system, the

numbers of duplexes at these transitions are essentially identical to that of the **A20**/**T20** system due to greater target access. As **A20** loading increases to 15% (Figure 3.3.3 (d)) aggregates in the **A20**/**T10** system become larger and more fractal-like. These aggregates continue to increase in size as the **A20** loading is further increased to 100%. Thus, it appears that once the critical probe concentration to drive DNA-mediated aggregation is reached, the length of the diluent strand does not affect the overall resultant aggregate structure. Combined, the results for **T10** and **T20** diluent strand particles reveal that the type and presence of diluent strands plays a tremendous role in controlling DNA-mediated aggregation. Perhaps of greatest importance is the number of **A20** probes that must be present to cause complete particle aggregation. For both systems, this is observed at approximately 5 to 6 possible duplexes within the contact area between two particles. Even though primary hybridization behavior varies wildly between the two diluent strands, the *ability* of 5 to 6 duplexes to form is the controlling factor in determining ***C***** in both cases (resulting in a minimum pair interaction potential between 1.04 μm particle surfaces required for aggregation of approximately 5 k_BT). The **T10** strand, by increasing access of both soluble and immobilized complementary **B** strands to the hybridizing segment on **A20**, appears to effectively reduce the number of **A20** *probes* that must be on the particle for aggregation to occur. However, the net attraction in both diluent strand systems is likely to be comparable since a minimum of five to six duplexes is consistently reported across multiple systems for mediating successful aggregation *(8, 10)*.

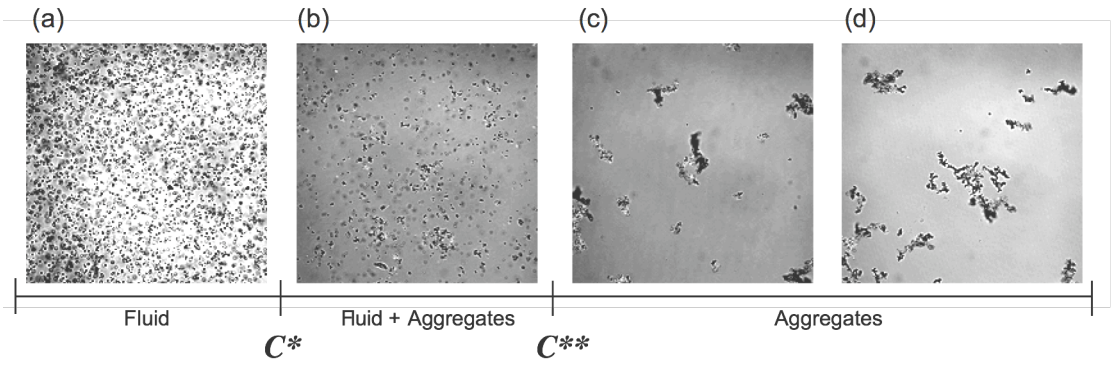

Figure 3.3.3 Confocal micrographs taken in DIC mode at 40x for microsphere suspensions in which one microsphere is functionalized with (a) 0%, (b) 5%, (c) 10%, and (d) 15% **A20** strands (initial **A20** loading) with **T10** as the diluent strand. The other microsphere population is functionalized with 100% **B20**. ***C**** indicates the critical concentration of **A20** to induce a fluid (particle singlets) to fluid + aggregates phase transition in which small aggregates and singlets are present; here it occurs at or below 5%. ***C*** indicates the fluid + aggregates to aggregates phase transition in which the suspension is entirely composed of larger aggregates. This latter transition occurs between 5% and 10% **A20** loading *(6)*.

3.3.3 – Colloidal Satellite Assembly in the Presence of Diluent Strands

To investigate the effect of diluent strands on the programmed DNA-mediated assembly of colloidal "satellites" comprised of a large central or core particle surrounded by a layer of smaller colloidal particles, 5.01 μm particles were conjugated with varying ratios of **A20** probe and **T20** diluent strand. Following coupling, the particles were mixed under static conditions for 24 hours with an excess of 1.04 μm **B20** coupled particles, and imaged using confocal microscopy. Figure 3.3.4 shows the results of this experiment. Again, the control sample in Figure 3.3.4 (a) reveals only singlets in suspension when the template particle consists of the noncomplementary **T20** diluent strands only. When the loading of **A20** is increased to 25% in 3.3.6 (b), the ***C**** for the 1.04 μm aggregate case, no assembly is observed. Interestingly, results in Figure 3.3.4 (c) show that even at 90%

A20 loading, samples showed negligible particle aggregation. Upon increasing the sample to 100% **A20** loading, complete satellite assembly is observed.

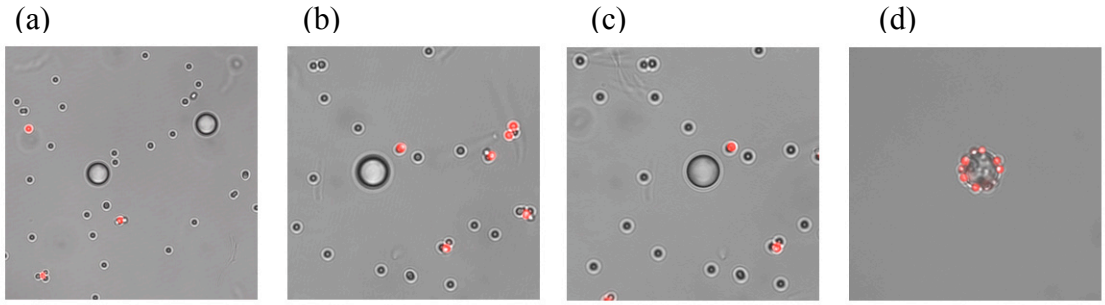

Figure 3.3.4 – Phase diagram for micelle assembly with increasing **A20** strands on the 5.01 µm template surface. Images reveal no assembly occurs at less than 100% **A20** loading. (a) 0% **A20**, (b) 25% **A20**, (c) 90% **A20** and (d) 100% **A20**.

To account for this lack of assembly for all but the 100% **A20** case, it is important to understand the differences in the two systems, primarily the density of probes on the particle surface. Section 2.2.3 discusses the surface density of hybridized targets on the surface of 5.01 µm microspheres. It is observed that the surface density is significantly lower than that seen in the 1.04 µm cases. This result is attributed to the large difference in the COOH parking area for the two colloidal particle populations. Parking area is a term used to describe the "space" occupied by surface functional groups. For the COOH groups on the surface, this therefore correlates to the number of probes it is possible to fit on an individual particle. As the parking area for the 5.01 µm system is significantly larger (44.5 $Å^2$ vs. 9.0 $Å^2$), it is not surprising that the packing of the **A20** probes is less dense than that seen on the 1.04 µm particles. Therefore, though the 5.01 µm particles

have a higher *total* number of probes on the surface, their packing is significantly less dense. The contact area between the 5.01 μm and 1.04 μm particles is calculated and results in a maximum of only 3 duplexes between the particle surfaces (using the same geometric approach as in 2.1.4). Therefore, even at 100% **A20** loading, the system is sitting right at the ***C***** for the 1.04 μm aggregate system. Though fewer linkages may be required for the binary system, even reducing the number of probes in the contact zone by 5% favors fluid phase behavior. Though this means dilution will not be required for subsequent studies with colloidal satellite assemblies involving the 5.01 μm colloidal particles, it does reveal that for a 10 base-long duplex, the colloidal satellites are linked together with the minimum number of duplexes required for complete assembly.

3.4 – Conclusions

In summary, this chapter detailed our investigation into the use of diluent strands to modify the aggregation behavior of DNA-mediated assembly. We selected two thymine oligonucleotides of differing length in order to reduce the number of **A20** probes that could be immobilized on the surface. It was determined that both diluent strands play a large role in modifying the number and hybridization activity of neighboring **A20** strands. The **T20** case was seen to result in a fairly linear correlation between the initial (prior to coupling to colloidal particles) and final (coupled to colloidal particles) ratio of probe to diluent strand. The **T10** case did not result in the same behavior, indicating the difficulty in maintaining a 1:1 correlation when coupling involves varying lengths of oligonucleotides. The phase behavior of both systems was investigated, and the critical

concentration of probes for each diluent strand system required for aggregation was determined. As we wish to program sufficient but modest DNA-mediated attractions in order to allow for subsequent redispersion of DNA-linked structures, we selected the minimum **A20** probe concentration at which complete aggregation (for heterogeneous 1.04 μm particles) or complete assembly (for colloidal satellites) occurs. Thus, following quantitative analysis, subsequent studies of redispersion or restabilization via secondary hybridization events employ the 10 base-long duplex system at 25% **A20** surface coverage. This corresponds to approximately 5 duplexes formed between particles, of which at least one must be dissociated or displaced to drive redispersion via competitive hybridization. For colloidal satellites, 100% **A20** surface coverage on 5.01 μm colloidal particles is used to drive assembly to completion. These results indicated that regardless of the electrosteric environment at the particle surface, a minimum pair interaction potential of approximately 5 k_BT is required to induce complete particle aggregation via DNA hybridization. Unlike prior work, however, we are interested in reducing this interaction potential to aid in competitive redispersion.

References

1. Biancaniello, P.L., Crocker, J.C., Hammer, D.A., and Milam, V.T. *Langmuir*, **2007**. *23*. 2688-93.

2. Jin, R., Wu, G., Li, Z., Mirkin, C.A., and Schatz, G.C. *J. Am. Chem. Soc.*, **2003**. *125*. 1643-54.

3. Halperin, A., Buhot, A., and Zhulina, E.B. *Langmuir*, **2006**. *22*. 11290-304.

4. Peterson, A.W., Heaton, R.J., and Georgiadis, R.M. *Nucleic Acids Res*, **2001**. *29*. 5163-8.

5. Tison, C.K. and Milam, V.T. *Langmuir*, **2007**. *23*. 9728-36.

6. Tison, C.K. and Milam, V.T. *Biomacromolecules*, **2008**. *9*. 2468-76.

7. Zuker, M. *Mfold Web Server*. **2003**; Accessed 12/1/06. Available from: http://mfold.bioinfo.rpi.edu/.

8. Biancaniello, P.L., Kim, A.J., and Crocker, J.C. *Phys. Rev. Lett.*, **2005**. *94*. 058302.

9. Kim, A.J., Biancaniello, P.L., and Crocker, J.C. *Langmuir*, **2006**. *22*. 1991-2001.

10. Milam, V.T., Hiddessen, A.L., Crocker, J.C., Graves, D.J., and Hammer, D.A. *Langmuir*, **2003**. *19*. 10317-23.

CHAPTER 4

Development of an Enzymatic Approach to Control Diluent Strand Presentation on Colloidal Particles

Results for the diluent strand studies in Chapter 3 reveal that maintaining one-to-one correlation in mixtures of different sequences is difficult unless the sequences are identical in base length. In this chapter, in order to surround probes on particle surfaces with shorter diluent strands while still maintaining control of the ratio of immobilized sequences, we have developed an enzymatic protocol for clipping the diluent strands following immobilization. Using the sequence-specific restriction endonuclease *AluI*, we show that between 50 - 70% of surface immobilized diluent strands can be cleaved while nearby **A20** probes are not affected. The development of the multistage digest protocol will be detailed, followed by an investigation into the effect the location of the recognition segment (relative to the particle surface) has on the activity of the enzyme. Next, the effect of shorter, clipped diluent strands *at controlled concentrations* on particle aggregation is investigated. Finally, a comparison of all diluent strands is made regarding coupling to immobilized ratios, effects on primary target hybridization activity, and differing values found for the critical probe concentration to induce phase transitions.

4.1 Experimental Setup

4.1.1 - Oligonucleotide Selection

Aminated and FITC-labeled single-stranded oligonucleotides were purchased from Invitrogen. Strands were purified, aliquoted and stored as previously described in

Chapter 2. Strand nomenclature will be as follows: complementary strands employed for particle assembly are labeled as **A** and **B**, followed by the total number of bases. All bases in the soluble, FITC-labeled target strands (i.e. not immobilized on a microsphere surface) are intended for hybridization events. For aminated oligonucleotides immobilized on microspheres, the first ten bases are included as a spacer segment between the microsphere surface and the hybridization segment (also ten bases in length). Multiple copies of an identical sequence (**A20** or **B20**) are immobilized on one of two populations of microspheres for aggregation experiments. Diluent strands to be clipped by restriction endonuclease *AluI* are labeled as **R6** and **R10** with the number indicating the sequence base-length remaining *immobilized on the surface* after clipping. Initially, both **R6** and **R10** are equal in sequence length to **A20** and **B20** but are complementary to neither. These diluent strands are intended to reduce the number of **A20** probes immobilized on one population of microspheres. For flow cytometry experiments, **A20** or mixtures of **A20** and **R10**, or **R6** are immobilized on nonfluorescent microspheres and are then incubated with dye-labeled, soluble target strands. Soluble **B** sequences are again employed as target strands for active **A20** probes while soluble **R′6** or **R′10** strands are intended to hybridize to unclipped **R6** or **R10** strands to promote subsequent cleavage by the restriction endonuclease *AluI*. Note: The recognition sequence segment (AGCT) must be hybridized to its complementary segment in order for *AluI* to bind to and clip the **R6** or **R10** diluent strands. Soluble stands are again fluorescently-tagged with FITC on the 5' end for quantifying hybridization activity. All strands used in these experiments are listed in Table 4.1.1.

Table 4.1.1 - Sequences and theoretical duplex melting temperatures (with soluble target) *(1)*, T_m, for probes, targets, and diluent strands. The recognition segment for *AluI* cleavage is indicated by bold text for the relevant diluent and target sequences *(2)*.

function	sequence	T_m
immobilized probe	**A20** = 5' - TTTTTTGGATTGCGGCTGAT - 3'	NA
immobilized target (for aggregation only)	**B20** = 3′ - ACGCCGACTATTTTTTTTTT - 5′	NA
immobilized diluent strands	**T20** = 5' - TTTTTTTTTTTTTTTTTTTT - 3'	NA
	T10 = 5' - TTTTTTTTTT - 3'	NA
immobilized diluent strands	**R6** = 5' - TTTT**AGCT**CCCCACCAGTGC - 3'	NA
	R10 = 5' - TTTTTTTT**AGCT**CCCCACCA - 3'	NA
soluble, noncomplementary target	**NC20** = 5' - TTTTTTGGATTGCGGCTGAT - 3'	NA
soluble, complementary targets to probes	**B10** = 3' - ACGCCGACTA - 5'	72.0°C
	B14 = 3' - CCTAACGCCGACTA - 5'	75.2°C
soluble, complementary targets to diluent strands	**R'6** = 3' - AA**TCGA**GGGGTGGTCACG - 5'	82.7°C
	R'10 = 3' - AA**TCGA**GGGGTGGT - 5'	78.5°C

4.1.2 - Particle Preparation

Nonfluorescent 1.04 μm carboxylated polystyrene particles (Bangs Laboratories) and 1.1 μm red fluorescent carboxylated polystyrene particles (Molecular Probes) were coupled to aminated sequences using EDAC chemistry as detailed in Chapter 2. The nonfluorescent microspheres are functionalized with **A20** strands, while the fluorescent microspheres are functionalized with the complementary **B20** strands. For cases involving the digestible diluent strands, nonfluorescent microspheres are incubated with a mixture of aminated diluent strands (**R10**, or **R6)** and aminated **A20** probes in order to simultaneously immobilize multiple copies of both sequences on the microsphere population. The ratio is controlled by mixing the sequences in fixed ratios prior to coupling as discussed in Chapter 3. For all of these studies, the fluorescent particles are only functionalized with **B20** and used only in aggregation experiments.

4.1.3 - Restriction Endonuclease Digest Protocol

Restriction endonuclease *AluI* and required buffers were purchased from New England Biolabs and stored as received at -20 °C until used. The enzyme *AluI* was selected for two main reasons; one, its specific recognition segment required only minor changes to the **A20** probe sequence and two, it is one of relatively few restriction enzymes that cleave to form a "blunt-end" duplex, preventing rehybridization with other sequences in solution as well as other complications which arise from strands which are clipped to form duplexes with "sticky ends." The required digest buffer NEB2 (50 mM NaCl, 10 mM Tris-HCl, 10 mM MgCl2 and 1 mM dithiothreitol) was modified with 0.02% Tween 20 (NEB2/Tween) to maintain consistent surfactant concentrations in all buffers. Control experiments indicate that these low concentrations of Tween 20 do not affect the endonuclease digest ability within the experimental timeframe, though they may serve to degrade the enzyme activity over longer times. Following immobilization of **A20** probes and diluent (single) strands of **R6** or **R10** to the nonfluorescent microspheres at various ratios, the following digest procedure was developed and is illustrated in Figure 4.1.1. First, 37.5 μL of **A20/R6** or **A20**/**R10**-coupled particles at 0.01 volume fraction was centrifuged and the supernatant was removed. Particles were then washed in 100 μL of PBS/Tween buffer and resuspended to 100 μL in the same buffer. A 200 μL volume of **R′6** or **R′10** targets at 10 μM concentration was added and incubated with the suspension for 18 hours to ensure maximum duplex formation. Results in Chapter 2 (Figure 2.2.1) for targets of similar length revealed that maximum hybridization activity occurs after approximately 4 to 6 hours of incubation. Following target incubation, the particles were washed three times in 100 μL PBS/Tween, and 1/15 of the suspension was

removed for characterization via flow cytometry. The remaining suspension was then washed once in 100 μL of NEB2/Tween and resuspended to 50 μL in NEB2/Tween. Following resuspension, 5.0 μL (10 units) of the restriction enzyme *AluI* was added to the sample, and the suspension was placed in a UVP HB-1000 hybridizing oven at 37 °C to incubate for 90 minutes while rotating. The suspension was then removed and 5.0 more μL of *AluI* was added, followed by an additional 90 minutes in the oven. Following the second incubation, the sample was washed twice in 100 μL PBS/Tween, and 1/15 of the sample was again removed for characterization. This procedure involving target hybridization, two additions of *AluI*, and a final washing completes one digest *stage*. During handling, the enzyme is stored on ice, then immediately returned to the freezer after use. Hybridization with **R′6** or **R′10** targets followed by exposure to *AluI* is repeated up to five times resulting in a five-stage digest protocol. Following the fifth digest stage, the remaining samples are washed and then hybridized with **R′10, R′6**, **B10**, or **B14** targets in order to 1) measure the number of unclipped diluent **R6** or **R10** strands remaining and forming duplexes by hybridizing with **R′10** or **R′6** and 2) test if the hybridization activity of **A20** probes was affected by the digest procedure by hybridizing with **B10** or **B14**. This procedure was also carried out for a set of particles in which flow cytometry analysis was only performed after the first and fifth digest stages. This latter set of microspheres was then used for aggregation experiments. Surface density values for hybridized targets indicate that the removal of a small volume of particles (1/15 the original volume) at each stage does not significantly affect the final clipping percentage as compared to the sample for aggregation experiments with only two aliquots extracted.

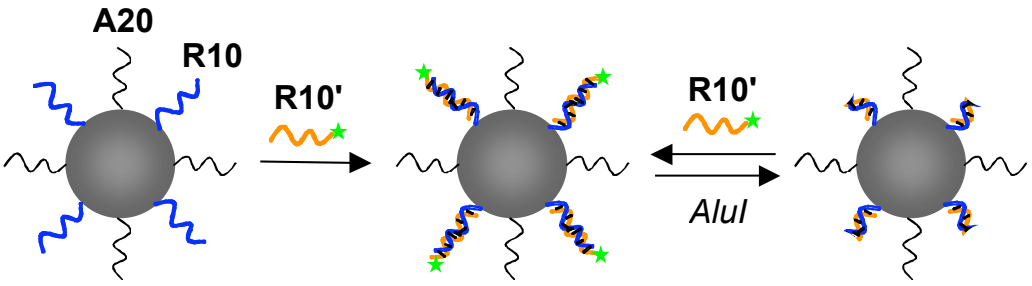

Figure 4.1.1 – Schematic illustrating steps employed to cleave immobilized **R10** diluent strands. Left: Multiple copies of **A20** probes and **R10** diluent strands are immobilized on the microsphere surface. Middle: DNA-functionalized microspheres are then incubated to FITC-labeled **R′10** targets to form **R10**:**R′10** duplexes. Right: Microspheres are incubated with the restriction enzyme *AluI* to cleave 14 base-long duplexes (**R10**:**R′10**) into shorter 4 and 10 base-long duplexes in which the FITC-labeled segment of the target is no longer associated with the microsphere. Following enzyme incubation, microspheres are washed and then incubated with **R′10** targets again as indicated by the opposing arrows. This dual incubation step or digest stage is repeated up to five times *(2)*.

4.1.4 - Flow Cytometry

Using FITC-labeled target strands, the hybridization activity of **A20** probe strands and **R6** or **R10** strands immobilized on nonfluorescent microspheres is quantified via flow cytometry, using our previously outlined protocol in Chapter 2. Each run of samples consisted of (a) DNA–functionalized microspheres alone (negative), (b) DNA-functionalized microspheres incubated with FITC-labeled targets identical in sequence to the **A20** probe strands (negative-**NC20)**, and (c) DNA-functionalized microspheres incubated with FITC-labeled target strands complementary to either the active **A20** probe (**B10**, **B14**) or the diluent strands **R10** or **R6** (**R′10** or **R′6**, respectively). BDFacs DIVA software was again used for data acquisition, with the same FSC, SSC, and FITC gating techniques previously described. To calculate the surface density of hybridized target

strands, the average fluorescence intensity values from three samples were compared to calibration curves for Quantum MESF FITC Medium calibration standards.

4.1.5 - Particle Aggregation Image Analysis

Confocal microscopy (Zeiss LSM 510) was used to investigate DNA-mediated aggregation between **B20**-functionalized red fluorescent microspheres and nonfluorescent microspheres coupled with varying ratios of **A20** and **R10** diluent strands. Samples are prepared as discussed in 2.1.5 for non-digested particles. Here, separate suspensions of fluorescent and nonfluorescent microspheres are again re-suspended in PBS/BSA at a total initial volume fraction of 0.01. For samples subjected to the digest procedure, however, some particles were lost after the multi-step process due to washing and supernatant removal at each step. To account for any loss, particle counting was used to determine the approximate particle concentration following the final digest stage. Briefly, 2.0 μL of the suspension was diluted to approximately 10^{-6} particle volume fraction in NanoPure Water and was loaded into a 2.0 μL Hamilton syringe. The suspension was ejected onto a cleaned glass slide in 0.25 μL increments and the suspension was allowed to dry via evaporation of the water. The slide was then loaded onto a Zeiss fluorescence microscope (Zeiss 200-M) and the particles within each drop were counted at 40x. The concentration of particles in each digested sample was then determined. To ensure an equivalent number of **A20** and **B20** coupled particles present within each sample, the number density of undigested **B20** red fluorescent particles was adjusted to match the number density of digested **A20** nonfluorescent particles for each aggregation experiment.

To prepare sample chambers for aggregation experiments, 20 μL wells are again formed using Mμlti* Hybridization Slides. Within the well, 10 μL of PBS/BSA is added, and allowed to coat the surface for 10 minutes to help prevent nonspecific adhesion of particles to the glass slide surface. In a separate 0.65 mL centrifuge tube, 2.0 μL of the **B20** red microsphere suspension was added along with the volume of **A20/R10** nonfluorescent microspheres required to introduce an equivalent number of particles. PBS/BSA is then added to bring the entire volume in the tube to 15.0 μL. This 15.0 μL suspension is briefly centrifuged to consolidate the suspension, sonicated to disperse the microspheres, and then added to the hybridization well resulting in a 25.0 μL total volume suspension on the slide. A glass cover slip is then mounted on top forming a tightly sealed well that minimizes evaporation. All samples are incubated at room temperature for 24 hours and then imaged using confocal microscopy. DIC mode is used to investigate aggregate morphology and phase transitions of the suspensions associated with hybridization events. Fluorescence mode was used to investigate and confirm aggregation occurred between complementary fluorescent and nonfluorescent particles.

4.2 – Enzymatic Digest with Restriction Endonuclease *AluI*

4.2.1 - Quantitative Analysis of Restriction Endonuclease Digest Efficiency

Restriction enzyme recognition and clipping activity is based upon binding and recognition of a specific sequence segment of an oligonucleotide duplex. For *AluI*, the recognition segment is AGCT:TCGA. As opposed to the **T** diluent strands that existed solely as single-stranded oligonucleotides, immobilized **R** diluent strands were first

hybridized to their complementary target and then exposed to the enzyme repeatedly. Several controls were first run to test for specificity of 1) target hybridization with **R10** and 2) *AluI* activity. First, flow cytometry revealed that noncomplementary target strands (**NC20**) have no affinity for either **R10** or **R6** strands as seen in Figure 4.2.1 in which both the noncomplementary and negative samples have the same fluorescence intensity after incubation. Second, duplexes intended for clipping were incubated in PBS buffer as well as NEB2/Tween buffer at 37 °C without the enzyme and no change in duplex number was observed as seen in Figure 4.2.2. Finally, flow cytometry indicated no hybridization activity occurs between **A20** and either **R′10** or **R′6** target sequences, as shown in Figure 4.2.3. Combined, these control experiments indicate that all changes in the number of **R**-based duplexes before and after exposure to *AluI* must be due to activity of the enzyme itself. In separate experiments, **B10** and **B14** targets were used to monitor any effects that *AluI* had on the hybridization activity of the **A20** probes. Figure 4.2.4 shows that the number of **A20**:**B10** and **A20**:**B14** duplexes was equivalent before and after repeated enzyme exposure, indicating nonspecific clipping of the active **A20** probes is negligible. Finally, flow cytometry was performed to quantify the number of hybridized **R** diluent strands on the microspheres before and remaining after each exposure to restriction endonuclease in order to determine the efficiency of enzymatic cleavage of the diluent strands. For these experiments, FITC-labeled 14 base-long targets (**R′10**) complementary to the first (3′-5′) 14 bases on the immobilized **R10** diluent strand were employed. Any clipping activity of *AluI* on **R10**:**R′10** duplexes removes the FITC-labeled end of the **R′10** target strand, and should thus result in a decrease in the average

fluorescence intensity associated with the microspheres. Figure 4.2.5 shows the decrease in fluorescence intensity for a representative case.

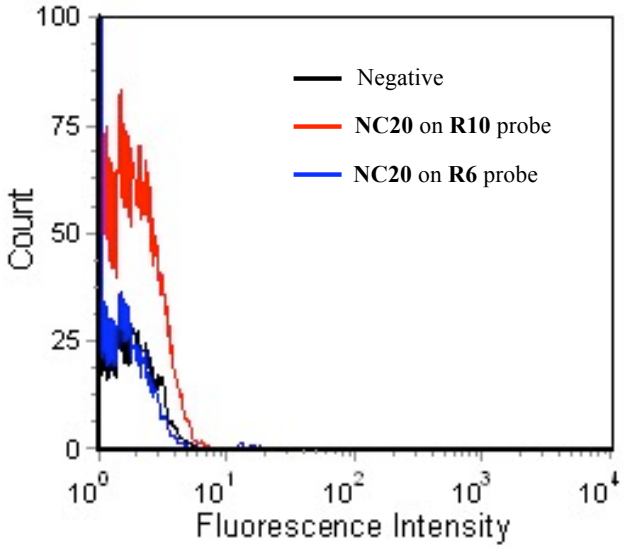

Figure 4.2.1 – Representative histogram of fluorescence intensity associated with DNA-functionalized microspheres incubated with noncomplementary FITC-labeled **NC20** target strands. Here, the immobilized sequences are **R10** (only) or **R6** (only) diluent strands. The negative control is a suspension of 100% **A20**-functionalized microspheres alone.

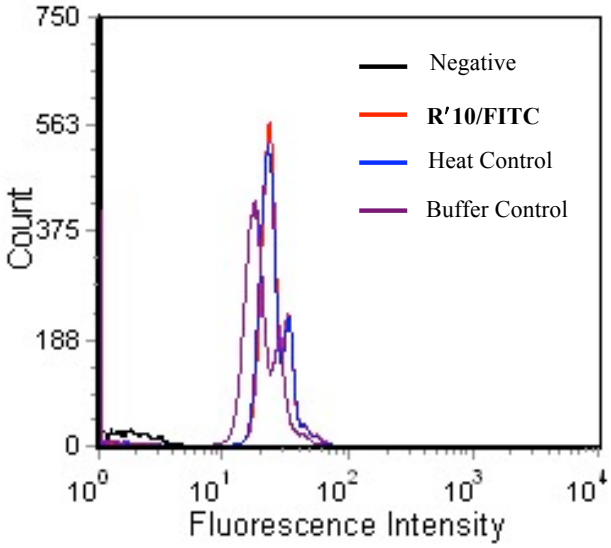

Figure 4.2.2 – Representative histogram of fluorescence intensity associated with DNA-functionalized microspheres incubated with FITC-labeled targets complementary to **R10** diluent strands, then warmed to 37 °C (heat control) or washed with the buffer solution used for the enzyme. The enzyme *AluI* was absent in each of these samples.

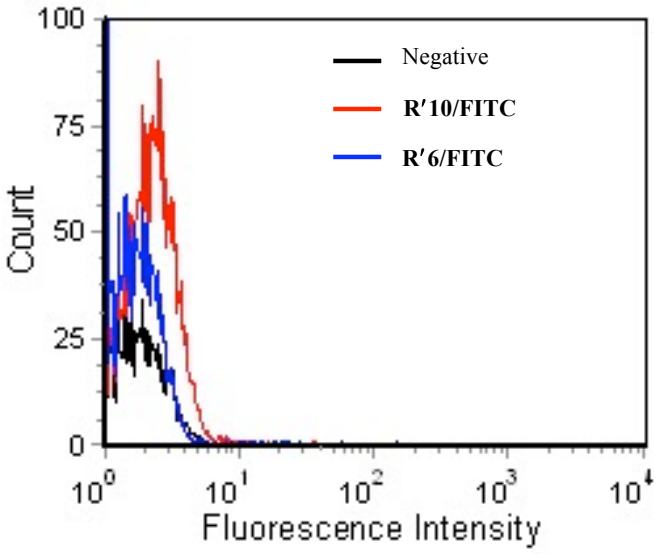

Figure 4.2.3 – Representative histogram of fluorescence intensity associated with **A20**-functionalized microspheres incubated with noncomplementary FITC-labeled **R'10** or **R'6** target strands.

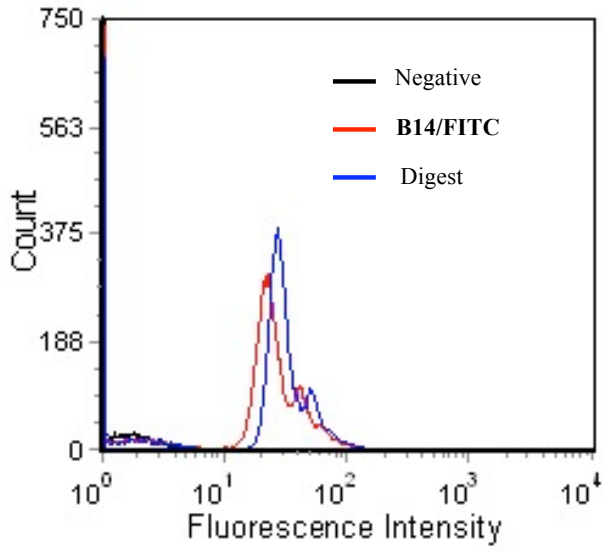

Figure 4.2.4 – Representative fluorescence histogram of fluorescence intensity associated with **A20**:**B14** duplexes that are FITC-labeled (**B14/FITC**) and then incubated with the enzyme (Digest). The negative control is a suspension of **A20**-functionalized microspheres alone.

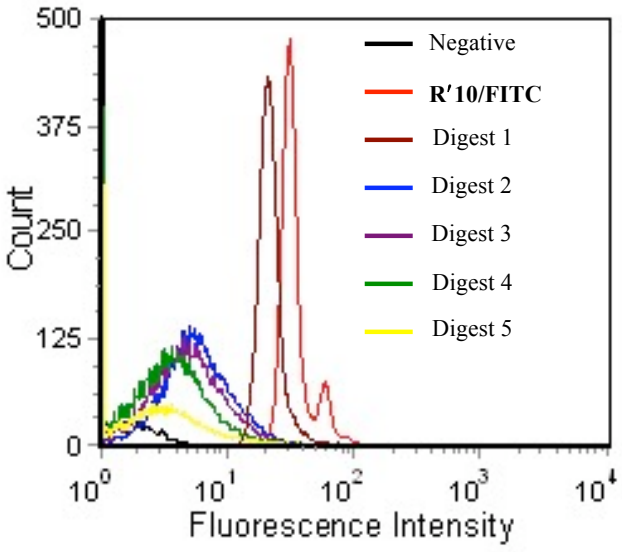

Figure 4.2.5 – Representative histogram of fluorescence intensity associated with **R10**-functionalized beads first incubated with complementary **R'10/FITC** targets and then incubated with the enzyme, *AluI*. The average fluorescence intensity is shown following each of the five separate digests.

Figure 4.2.6 shows quantitative results for the hybridization of **R′10** targets to immobilized **R10** diluent strands before and after each digest stage for various **R10** loading ratios. The 80% **R10** (20% **A20)** case is described here as representative of the samples. Following initial **R′10** hybridization to the 80% **R10** present on the surface, the surface duplex density is 3,845 oligos/μm^2. Despite comparable melting points and identical hybridization segment lengths for **A20**:**B14** and **R10**:**R′10** duplexes, the density of **R10**:**R′10** duplexes is approximately half that observed for the **A20**:**B14** duplexes at 80% **A20** loading (~8,100 oligos/μm^2 in Figure 3.2.3). Since **R10** and **A20** are both amine-terminated sequences of equivalent length, surface coverage differences on the microsphere should not occur during coupling. Thus, assuming no differences in **A20** or **R10** coverage, it appears that only half of the immobilized **R10** strands initially form duplexes with **R′10** targets. This is not completely unexpected, as small sequence differences have been shown to dramatically change hybridization behavior at surfaces *(3)*. Following target hybridization, the sample is then exposed to the restriction endonuclease and the surface duplex density drops to 909 oligos/μm^2. These values indicate that after the first digest stage, approximately 24% of the original hybridized **R′10** targets remain. To repeat the digest procedure, the microspheres undergo a second exposure to the **R′10** target and the duplex density increases to 2,835 oligos/μm^2, but does not return to its higher initial duplex density. Following a second exposure to *AluI*, the duplex density falls to 675 oligos/μm^2. This trend of partial reduction in duplex number with each digest stage is modest, but continuous. Following five digest stages and a final incubation with target, the final surface density of duplexes is 1,350 oligos/μm^2 corresponding to a 65% reduction in the *initial* number of duplexes. Overall,

this trend in enzyme activity is apparent for the other **A20/R10** loadings with total clipping percentages of 69% for the 100% **R10** case, 64% for the 85% **R10** case, 65% for the 80% **R10** case, 57% for the 75% **R10** case, 61% for the 50% **R10** case, and 41% for the 25% **R10** case. This "saw tooth" pattern in duplex number with each digest stage for all loadings suggests first, that upon enzyme exposure, clipping of hybridized duplexes occurs successfully but inefficiently and second, that upon re-exposure to target, new **R10**:**R′10** duplexes form with previously unoccupied **R10** strands. The formation of these new duplexes may be favored by the reduced steric interference of the now shorter immobilized diluent strands, allowing previously unoccupied **R10** strands to more easily hybridize to their complementary targets and thus be susceptible to enzymatic cleavage in the next digest treatment. The lower clipping efficiency for the 25% case is thus likely due to the continued steric interference of the longer and more numerous **A20** probe strands which remain 20 bases long throughout the entire process (unclipped).

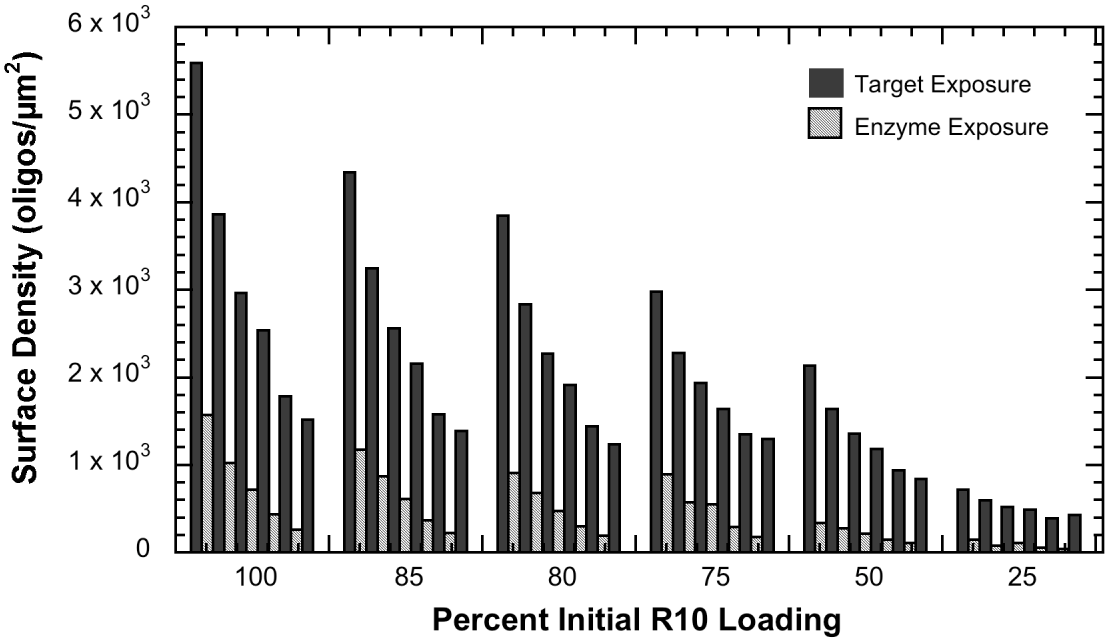

Figure 4.2.6 – Surface density of duplexes formed between immobilized **R10** diluent strands and soluble **R′10** targets before (target exposure) and remaining after (enzyme exposure) sequential exposures to the restriction endonuclease *AluI*. Each diluent loading percentage is shown undergoing a total of five digest stages followed by a final incubation with **R′10** target strands *(2)*.

After five digest stages between 50% and 70% of duplexes are permanently clipped for moderate to high initial loadings of the diluent **R10** strand on the microspheres. Thus, it appears that the digest efficiency for this microsphere system is not as high as some reports of approximately 90% for Au nanoparticles. These previous studies, however, did not report re-exposing the nanoparticles to target strands *following* the enzyme exposure to check for possible duplex formation with remnant or previously unoccupied oligonucleotides. Thus, the reported ranges of 65 to 90% efficiency appear comparable to our clipping of 76% of the original duplexes following the first digest stage for the 80% **R10** case. Our prior results revealed that control of microsphere

aggregation and redispersion is contingent upon minimizing the number of **A20**:**B20** duplexes formed between microsphere surfaces. Thus, subsequent hybridization and assembly experiments focus on employing microspheres with lower initial **A20** loadings in which a significant number of the more numerous diluent **R10** strands can be clipped in length.

4.2.2 - Hybridization Activity of A20 Probes Following Clipping of R10 Diluent Strand

Following the five-stage digest, experiments were performed to compare the hybridization activity of the **A20** probes surrounded by clipped **R10** strands. Figure 4.2.7 shows the surface density of **A20** hybridized to either **B10** or **B14** targets in the presence of clipped **R10** diluent strands. For this case, a continual increase in hybridization activity (illustrated by an increasing density of **A20**-target duplexes) is observed with **A20** loading. Unlike the sharp initial rise followed by a relatively constant number of duplexes with probe loading in the **A20/T10** system discussed in Chapter 3.2.2, the increase in duplex number with probe loading for the **A20/R10** system is relatively linear overall and mimics the activity of probes in the **A20/T20** system. Figure 4.2.7 again shows the **R10** data overlaid with **T20** data for comparison. At low **A20** loadings of 15% and 20%, however, the surface density of duplexes formed in the presence of cleaved **R10** strands is slightly higher than that observed for the **T20** case. In fact, we see for both systems involving asymmetric diluent and probe strands (**A20/R10** and **A20/T10**) that hybridization activity is elevated at low **A20** loadings (or high diluent strand loading) compared to the **A20/T20** system involving sequences of equal length. Interestingly, the use of clipped duplexes as diluent strands appears to negate the “lag” observed for the **T20** case discussed in 3.2.1. It is hypothesized that in the cleaved case, the 1:1 correlation

between solution and immobilized ratios is maintained, but steric interference of diluent strands observed for the **T20** case is reduced *due to* the cleavage after immobilization – the targets are better able to find the hybridization segment of **A20** probes and therefore the probability of successful target hybridization improves at lower probe loadings.

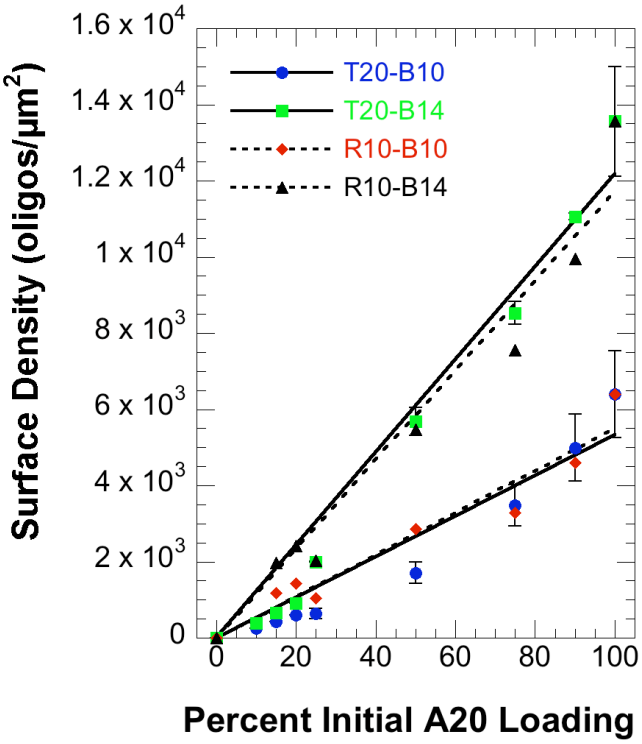

Figure 4.2.7 – Surface density of duplexes formed between immobilized **A20** probe strands and soluble **B10** or **B14** targets as a function of initial loading of **A20** probe on microspheres with either **T20** strand (solid) or clipped **R10** (dashed) as the immobilized diluent strands *(2)*.

For the cases involving low loadings of **A20**, clipping approximately 60 - 70% of the surrounding diluent strands appears to reduce their steric interference with target strands accessing and hybridizing to the **A20** probes and results in slightly elevated probe

hybridization activity. At 25% or greater **A20**, however, the number of duplexes in the **A20/R10** and **A20/T20** systems is either nearly identical (e.g. for 25% **A20** cases) or closely matched in value for a given probe loading. This close match in duplex number for the two systems indicates that at these higher **A20** loadings, the effect of clipping the relatively fewer diluent strands to reduce their steric interference is less pronounced. Overall, these studies indicate that the steric interference of diluent strands can be reduced at relatively high diluent loadings while maintaining good fidelity to oligonucleotide loading by employing probes and diluent sequences of initially equal length and then clipping diluent sequences following surface immobilization.

4.2.3 - Effect of Recognition Site Location on Enzymatic Digest Efficiency

In addition to developing a digest protocol capable of clipping microsphere-bound oligonucleotides, we investigated the effect of the location of the recognition site on *AluI* cleavage activity. This work helps elucidate the behavior of oligonucleotides and enzymes near microsphere surfaces. Previous work investigating enzyme activity on immobilized oligonucleotides employed sequences in which the recognition site was 16 to 35 bases away from the nanoparticle surface *(4-11)*. In the previous section, modest clipping was observed at sites eight bases away from the microsphere surface. Here, a four-base separation between the surface and recognition segment is investigated. For this study two different **R** strands are used which leave either a six (**R6)** or ten (**R10**, previously discussed) base-long oligonucleotide on the surface following enzymatic clipping. Figure 4.2.8 illustrates the location of the AGCT:TCGA recognition site with respect to the surface for these two diluent strands. For the **R6** strand, the first base to be recognized by the restriction endonuclease is only 4 bases, or approximately 18 Å, from

the surface of the microsphere. For the **R10** case, this distance doubles, with the recognition site starting at the eighth base pair. Figure 4.2.9 shows the effect of this distance on the number of FITC-labeled duplexes before (hybridized) and remaining after (clipped) exposure to the restriction endonuclease *AluI* on surfaces immobilized with 100% **R10** or **R6** diluent strands (0% **A20**). Detailed discussion of the data for the **R10** case was presented in the previous section, so here discussion focuses on comparing the results for the **R10** and **R6** systems. The initial surface density of **R6**:**R′6** duplexes is 3292 oligos/μm^2. After five digest stages, this duplex density does not change appreciably. The slight decrease in the surface duplex density after each digest step is attributed to slight but inefficient clipping by *AluI*. Similar to the **R10** case discussed previously, the increase in **R6**:**R′6** duplexes upon exposure to the target is attributed to the formation of new duplexes with previously unoccupied **R6** diluent strands. This increase in duplex number is only slight, however, since few **R6** strands are clipped to shorter lengths to reduce their steric interference with any subsequent hybridization events. Overall, the close proximity of the recognition segment to the particle surface for the **R6** case confers little enzymatic activity of the endonuclease. In comparing the modest but continuous enzymatic activity for the **R10** case with the nearly negligible enzymatic activity for the **R6** case (Figure 4.2.10), it is clear that the closer the recognition site is to the particle surface, the less efficient the restriction endonuclease cleavage activity becomes. In fact, it appears that there is a cutoff distance at which enzyme activity on surface immobilized probes is rendered negligible. We attribute this inefficient digest behavior to the increased steric hindrance, as *AluI* must penetrate deeper into the duplex brush layer to clip at the recognition site. The probe **A20** and diluent **R6**

strands form a dense polymer brush layer on the surface, with an approximate total oligonucleotide density of 13,000 oligos/μm^2. For the 38 kDa endonuclease (in comparison, the **R′10** target is approximately 4.8 kDa) to reach the recognition site 18 Å from the microsphere surface, it must penetrate this dense polymer brush layer to an even greater extent for the **R6** case compared to the **R10** case. The negligible clipping for the **R6** case is comparable to the hindered activity of *DNase I* on surface-immobilized duplexes reported by Rosi et al. *(12)*, while the modest 69% clipping achieved for the 100% **R10** case is comparable to other studies reporting 65% to 90% digest efficiency for recognition sequences located much further from nanoparticle surfaces *(7-10)*. Combined, it is evident from our studies that the location of the recognition site with respect to the surface does play a significant role in determining the ability of *AluI* to clip surface immobilized strands. However, our results show that the longer spacer segments (16 bases or longer) employed in earlier work are *not* required to achieve comparable cleavage activity. This reveals, perhaps unexpectedly, that enzymatic processing can occur much closer to particle surfaces than previously reported. In section 2.2.2 the difficulties associated with understanding activity at a particle surface were outlined, and this work with *AluI* further reveals the effect that surfaces can have on biomacromoleculer behavior.

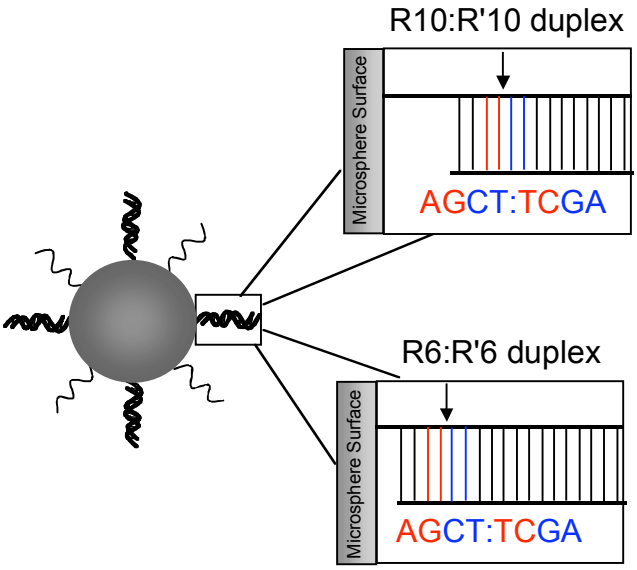

Figure 4.2.8 – Schematic illustrating the location of the recognition sequence segment (AGCT:TCGA) for duplexes formed between targets and either **R10** or **R6** diluent strands. The arrows indicate where cleavage by *AluI* occurs within the recognition segment *(2)*.

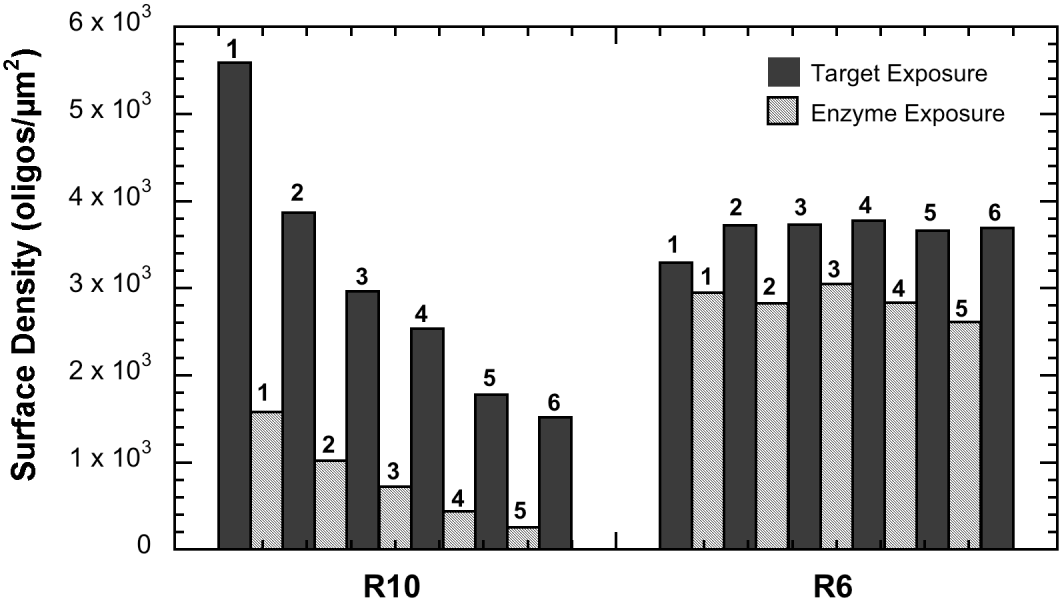

Figure 4.2.9 – Surface density of duplexes formed between immobilized **R10** or **R6** diluent strands and complementary soluble targets (**R′10** and **R′6**, respectively) before (target exposure) and remaining after (enzyme exposure) a series of exposures to the restriction enzyme *AluI*. The data in this set is for particles functionalized with either 100% **R10** or 100% **R6** *(2)*.

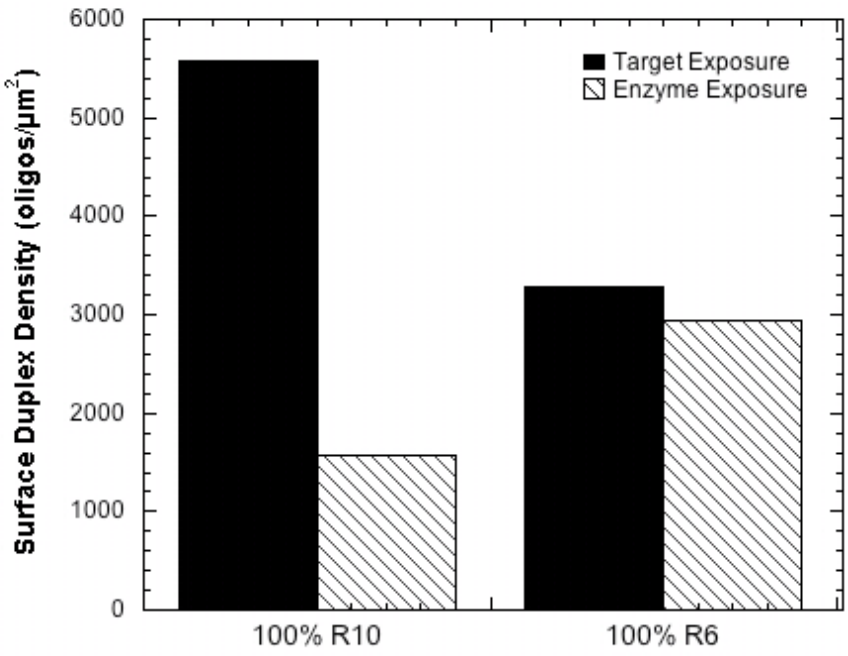

Figure 4.2.10 - Surface density of duplexes formed between immobilized **R10** or **R6** diluent strands and complementary soluble targets (**R′10** and **R′6**, respectively) before (target exposure) and remaining after (enzyme exposure) a single exposure to the restriction endonuclease *AluI*. This data is an individual set following the first digest shown in Figure 4.2.10. Both cases involve 100% **R10** or **R6** diluent loading (or 0% **A20**) on particle surfaces.

4.3 - Aggregation of Microspheres with Clipped Diluent Strands

4.3.1 - Phase Transitions of DNA-Functionalized Colloidal Particles at Various A20/R10 Loadings

Though it was determined that **R6** diluent strands were ineffectively cleaved and therefore unavailable to act as shorter diluent strands, **R10** was seen to undergo moderately high clipping without affecting nearby **A20** probes. These clipped **R10** diluent particles are here used for aggregation experiments in order to determine the effect that shorter diluent strands *at controlled ratios* have on particle aggregation. Figure

4.3.1 shows the effects of increasing **A20** loading with the clipped **R10** diluent strand present. Again, as discussed in earlier chapters, 0% **A20** loading shows a suspension of particle singlets, indicating nonspecific attractions between **R10** and **B20**-functionalized particle surfaces are negligible. For all subsequent nonzero probe loadings, we chose to investigate the same probe loadings tested previously in the **T20** diluent strand case for direct comparison, starting with 15% **A20** in Figure 4.3.1 (b). At this loading, the fluid + aggregates phase is observed for the **A20**/**R10** case, indicating that ***C**** is again lower for this asymmetric diluent-probe system compared to the symmetric **A20**/**T20** system. However, unlike the extensive aggregation observed for **T10**, the **A20**/**R10** system does possess many particle singlets at 15% and even 25% **A20**, Figure 4.3.1 (c), so the critical probe concentration needed to drive complete aggregation has not yet been reached. Upon increasing the probe concentration to 50%, Figure 4.3.1 (d), the extent of particle aggregation has increased with few singlets remaining in solution. This result indicates that the critical concentration for aggregation, ***C*****, lies between 25% and 50% **A20** for the **R10** diluent strand case. At 50% **A20** loading, the aggregates also appear larger and more fractal. This trend in aggregate size and morphology continues upon a further increase in **A20** to 75% and 90% with aggregate structure becoming continually larger and more fractal. These trends in aggregate size and morphology with increased probe loading generally follow those observed for both the **T20** and **T10** diluent strand cases. Thus, it appears that once the critical probe concentration to drive DNA-mediated aggregation to completion is reached, the length of the diluent strand does not affect the overall resultant aggregate structure.

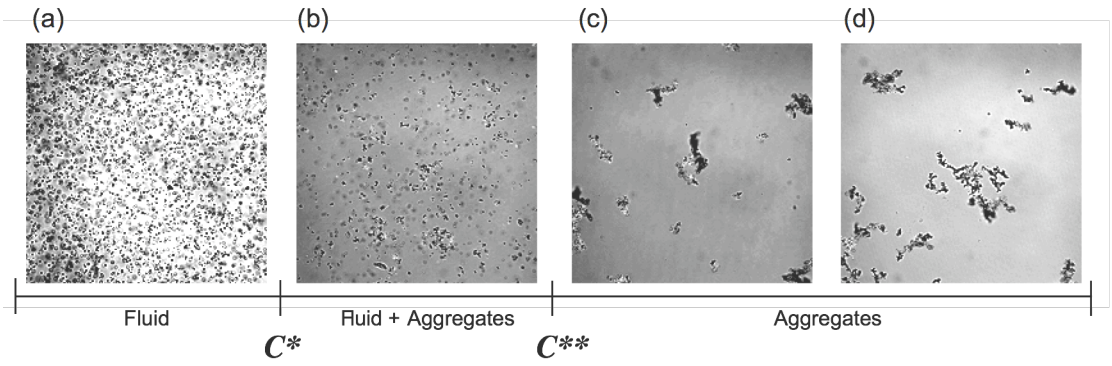

Figure 4.3.1 – Confocal micrographs taken in DIC mode at 40x for microsphere suspensions in which one microsphere population is functionalized with (a) 0%, (b) 15%, (c) 25%, and (d) 50% **A20** strands with clipped **R10** as the diluent strand. The other microsphere population is functionalized with 100% **B20**. ***C**** indicates the critical concentration of **A20** to induce a fluid (particle singlets) to fluid + aggregates phase transition in which small aggregates and singlets are present. Here, this ***C**** occurs at or below 15% **A20** loading. ***C*** indicates the fluid + aggregates to aggregates phase transition in which the suspension is comprised of larger aggregates. This latter transition occurs between 25% and 50% **A20** loading *(2)*.

4.4 – Conclusions

In summary, we have investigated the ability of the restriction enzyme *AluI* to clip surface bound duplexes in order to modify the hybridization activity and aggregation behavior of 1.04 μm polystyrene microspheres. We developed and characterized a digest procedure for the restriction endonuclease *AluI* which is capable of cleaving 50-70% of surface immobilized strands on microsphere surfaces after five digest stages for high diluent (or low probe) loadings. We found that the proximity of the recognition site to the microsphere surface plays a tremendous role in determining the efficacy of the digest. To the best of our knowledge, this is the first work to systematically investigate the effect of surface proximity on the efficiency of restriction enzyme cleavage for surface-

immobilized oligonucleotides. Further, modest clipping was seen for recognition sites located as close as 8 bases from the particle surfaces, at least 50% closer than previously studied. The use of clipped asymmetric diluent-probe strands in place of the previously reported symmetric diluent-probe strands to dilute the number of active hybridizing probes revealed marked effects such as shifts to lower probe concentrations needed to drive the fluid to fluid + aggregates phase transition. Further, clipping the immobilized strands allows for control over the ratio of different sequences coupled to particle surfaces, while simultaneously deriving a mixture of strands of different lengths on the particle surface – this was not possible with the **A20/T10** case. These strands therefore resulted in a better 1:1 correlation in duplex density as a function of percent **A20** as the initial "lag" in duplex density associated with **A20/T20** cases was not observed for **A20/R10**. This behavior is likely due to achieving the same number of immobilized probes, but with decreased steric interference of neighboring clipped diluent strands, especially at the higher diluent (lower **A20**) loadings.

References

1. IDT. *SciTools Oligo Analyzer*. **2009**; Accessed 11/09/2007. Available from: http://www.idtdna.com/analyzer/Applications/OligoAnalyzer/.

2. Tison, C.K. and Milam, V.T. *Biomacromolecules*, **2008**. *9*. 2468-76.

3. Peterson, A.W., Wolf, L.K., and Georgiadis, R.M. *J. Am. Chem. Soc.*, **2002**. *124*. 14601-7.

4. Kanaras, A.G., Wang, Z., Bates, A.D., Cosstick, R., and Brust, M. *Angew. Chem. Int. Ed. Engl.*, **2003**. *42*. 191-4.

5. Kanaras, A.G., Wang, Z., Brust, M., Cosstick, R., and Bates, A.D. *Small*, **2007**. *3*. 590-4.

6. Kanaras, A.G., Wang, Z., Hussain, I., Brust, M., Cosstick, R., and Bates, A.D. *Small*, **2007**. *3*. 67-70.

7. Qin, W.J. and Yung, L.Y. *Langmuir*, **2005**. *21*. 11330-4.

8. Qin, W.J. and Yung, L.Y. *Biomacromolecules*, **2006**. *7*. 3047-51.

9. Qin, W.J. and Yung, L.Y. *Bioconjug Chem*, **2008**. *19*. 385-90.

10. Wang, Z.X., Kanaras, A.G., Bates, A.D., Cosstick, R., and Brust, M. *Journal of Materials Chemistry*, **2004**. *14*. 578-80.

11. Yun, C.S., Khitrov, G.A., Vergona, D.E., Reich, N.O., and Strouse, G.F. *J. Am. Chem. Soc.*, **2002**. *124*. 7644-5.

12. Rosi, N.L., Giljohann, D.A., Thaxton, C.S., Lytton-Jean, A.K.R., Han, M.S., and Mirkin, C.A. *Science*, **2006**. *312*. 1027-30.

CHAPTER 5

Competitive Displacement of Soluble and Immobilized Targets Through Secondary Hybridization Events

The preceding chapters have detailed an in-depth investigation into optimizing primary hybridization for a modest, but sufficient, hybridization affinity to drive DNA-mediated particle aggregation between weakly adherent colloidal particles. Diluent strands of various base lengths and processing conditions have also been investigated in order to minimize the number of DNA linkages that exist between particles. Here, we explore competitive hybridization events with secondary targets to displace primary targets, either alone or serving as linkages between surfaces. Previous research in this field has focused on the use of elevated temperature conditions and, to a lesser extent, enzymatic processing to redisperse DNA-linked assemblies, but our interests in biomaterials applications of DNA-programmed assembly and disassembly mandates fixed temperature and "buffer" conditions. We therefore investigate primary target displacement that is driven by affinity differences between primary and secondary targets. We will investigate the effect of primary and secondary target lengths in determining the ability of a soluble secondary target to displace a hybridized, soluble primary target. Once a specific oligonucleotide system has been selected, we detail the disassembly of DNA-linked structures using competitive hybridization. Here, the ability of a 14 base-long secondary target to redisperse aggregates linked by multiple 10 base-long duplexes is investigated. Confocal and fluorescence microscopy are used to investigate the suspensions before and after competitive hybridization, and controls are run to confirm the specificity of the redispersion. The effect of diluting the concentration

of probe strands with nonsense or diluent strands on competitive redispersion will also be discussed. Finally, competitive hybridization will be used to redisperse suspensions of colloidal satellite assemblies comprised of 5 μm template particles linked to 200 nm satellite particles via the same 10 base-long duplex. This study demonstrates that DNA-linked assemblies can be redispersed at a constant temperature; one of many considerations for extending DNA as a reversible assembly tool for *bio*materials applications.

5.1 – Experimental Setup

5.1.1 - Oligonucleotide Sequence Selection

Aminated and FITC-tagged single-stranded oligonucleotides are purchased, aliquoted, and stored as previously described. The strand nomenclature will be as follows: complementary strands employed for primary hybridization events are labeled as **A** and **B**, followed by the total number of bases. All bases in the soluble strands are again intended for hybridization events. The soluble, competitive strands are labeled as **A'** to indicate that they are added to hybridize to **A** probe strands during secondary hybridization events. Surface-functionalized strands possess an amine functionality on their 5' end, allowing for covalent coupling to carboxylated microspheres. For flow cytometry, **A20** is immobilized on nonfluorescent microspheres and unlabeled **B** sequences are employed as primary target strands for analysis. Soluble **A'** sequences are employed as secondary target strands. These soluble strands are FITC-tagged on their 5' ends for quantifying secondary hybridization events via flow cytometry. Table 5.1.1

shows sequence notation, composition and melting temperature, T_m, for all sequences in this study.

Table 5.1.1 - Sequences and theoretical solution melting temperatures *(1)*, T_m, for probe-target duplexes of strands used for flow cytometry experiments *(2)*. Calculations for T_m are based on an estimated oligonucleotide concentration of 2.140 mM in phosphate buffer solution. The oligonucleotide concentration estimate is based on the mathematical approach of Biancaniello et al *(3)*.

function	sequence	T_m
immobilized probe	**A20** = 5'-TTTTTTGGATTGCGGCTGAT-3'	NA
noncomplementary soluble target	**NC20** = 5'- TTTTTTGGATTGCGGCTGAT-3'	NA
soluble 1° targets	**B6** = 3'-CGACTA-5'	41.4 °C
	B8 = 3'-GCCGACTA-5'	61.5 °C
	B10 = 3'-ACGCCGACTA-5'	72.0 °C
	B12 = 3'-TAACGCCGACTA-5'	72.6 °C
	B14 = 3'-CCTAACGCCGACTA-5'	75.2 °C
	B16 = 3'-AACCTAACGCCGACTA-5'	76.6 °C
soluble 2° targets	**A'12** = 3'-TAACGCCGACTA-5'	72.6 °C
	A'14 = 3'-CCTAACGCCGACTA-5'	75.2 °C
	A'16 = 3'-AACCTAACGCCGACTA-5'	76.6 °C

5.1.2 – Particle Preparation

Nonfluorescent 1.04 μm and 5.01 μm polystyrene particles (Bangs Laboratories) were used for these experiments. The carboxyl surface functionality allows for covalent coupling with aminated probe strands using EDAC as described previously. 1.04 μm microspheres were immobilized with multiple copies of either the **A20** probe, allowing hybridization with complementary **B** strands of various lengths, and the competitive strands, **A'**, or **B20** (immobilized on the 5.01 μm particles).

5.1.3 - Flow Cytometry

Flow cytometry was used to quantify secondary hybridization events. To determine the hybridization activity of secondary target with **A20** probe strands in the presence of primary targets, **A20**-functionalized nonfluorescent microspheres were first incubated with unlabeled primary targets **B8U**, **B10U**, **B12U**, **B14U**, or **B16U** for six hours to allow primary hybridization events to occur first. Each primary target was hybridized to two different **A20** coupled batches with two samples in each batch (for a total of four sets of primary hybridized samples, total). These four sets for each primary target were repeated for *each secondary target tested*, resulting in four runs at each primary target length for the various secondary targets. Microspheres were then washed three times in hybridization buffer to remove any unassociated primary target strands and then incubated with dye-labeled secondary target strands **A'12/FITC**, **A'14/FITC**, or **A'16/FITC**. Following incubation for 24 hours (kinetics studies analyzing other time points are discussed in Chapter 6), microspheres are washed and flow cytometry samples are prepared and run as described in detail in earlier chapters. Quantum MESF FITC Medium standards were again used to convert fluorescence intensity values into the number of secondary, fluorescently labeled targets hybridized to probes.

5.1.4 - Particle Aggregation, Restabilization, and Image Analysis

Confocal microscopy (Zeiss LSM 510) was used to investigate the ability of DNA-functionalized microspheres to both aggregate (via primary hybridization) and be redispersed (via competitive hybridization). Separate suspensions of fluorescent and nonfluorescent microspheres were re-suspended in PBS/BSA at a total initial volume fraction of 10^{-3}. To prepare sample chambers for aggregation experiments, 20 μL wells

were formed using Mμlti* Hybridization Slides (Sorenson Bioscience). Within the well, 10 μL of PBS/BSA is added, and allowed to coat the surface for 10 minutes to help prevent nonspecific adhesion of particles to the glass slide surface. In a separate 0.5 mL centrifuge tube, 2.0 μL of each microsphere suspension (5.0 μm particles were used for select assembly experiments) are added to 11.0 μL of PBS/BSA. This 15.0 μL suspension is briefly centrifuged to consolidate the suspension, sonicated to disperse the microspheres, and then added to the hybridization well resulting in a 25.0 μL total volume suspension on the slide. A glass cover slip is then mounted on top forming a tightly sealed well. All samples are incubated at room temperature for 24 hours and then imaged. DIC mode is used to investigate morphology and phase transitions of the suspensions associated with primary and secondary hybridization events. Confocal microscopy was used to investigate specificity of aggregation.

Restabilization studies in the presence of soluble oligonucleotides are run using a similar protocol as aggregation experiments. To allow introduction of the soluble target strand **A'14**, Mμlti* Hybridization Slide spacers are replaced with a vacuum grease "well." The use of vacuum grease as a sealer allows removal of the top cover slide, addition of the soluble target strand (10 μL at 100μM), and reapplication of the top cover. To create a consistently sized well, vacuum grease is loaded in a 10 mL slip-tip syringe, and dispensed while tracing the Mμlti* Hybridization Slide spacer outline. The height of the vacuum grease from the surface allows for a suspension volume of ~ 40μL, allowing for the addition of 10 μL of soluble target strands without changing the concentrations used for microsphere aggregation. Suspensions are then incubated with the soluble strands for 24-72 hours and checked periodically for disassembly progress.

5.2 - Results of Soluble Target Displacement

5.2.1 - Review of Soluble Target Primary Hybridization

In section 2.2.2 and 2.2.4, it was determined that a 10 base-long duplex is sufficient to cause modest soluble target hybridization as well as aggregation of DNA-linked particles. However, 12, 14 and 16 base long strands are also shown to achieve either equivalent (12) or higher (14 and 16) duplex densities compared to **B10**. In this chapter, all primary targets previously discussed are subjected to competitive hybridization with the three longest secondary targets. By comparing the surface density of hybridized secondary targets to the surface density of the hybridized primary targets, we assess the ability of competitive strands to displace the primary targets.

5.2.2 - Quantitative Analysis of Secondary Hybridization Events

To investigate the ability of competitive soluble targets to displace primary targets hybridized to probes, flow cytometry was used to monitor the hybridization activity of FITC-labeled, *secondary* oligonucleotide targets. In this set of experiments, microspheres are first exposed to unlabeled, primary targets and then exposed to FITC-labeled, secondary targets. The peak fluorescence intensity of the microspheres alone (negative) and each unlabeled primary target (**B8U**, **B10U**, **B12U**, **B14U**) are all low and nearly identical in value as seen in the histogram, Figure 5.2.1 (only **B10U** is shown for clarity).

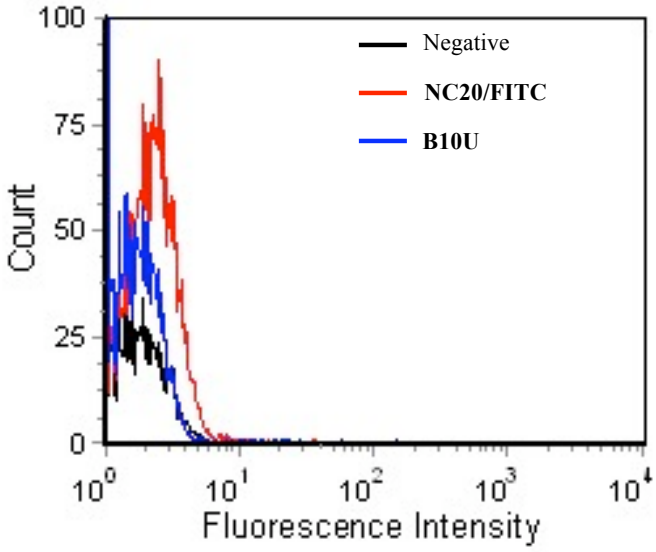

Figure 5.2.1 – Representative fluorescence histogram showing no fluorescence intensity differences between **A20**-functionalized 1.04 μm colloidal particles alone (negative) and incubated with either noncomplementary target (**NC20/FITC**) or with unlabeled **B10** targets.

These matching peak values indicate that no change in fluorescence intensity is observed for microspheres which have been hybridized to unlabeled primary target strands and that nonspecific association of noncomplementary target (**NC20/FITC**) is negligible. Figure 5.2.2 shows a representative fluorescence histogram for cases in which the microspheres are then exposed to any of the FITC-labeled secondary targets (**A′14/FITC** is shown as a representative secondary target) following incubation with the nonfluorescent primary strands. A general *decrease* in fluorescence intensity is observed as the length of the primary target strand increases from 8 to 16 indicating that the greater the affinity of the primary target, the more difficult it is for the secondary target to hybridize to the probe strands.

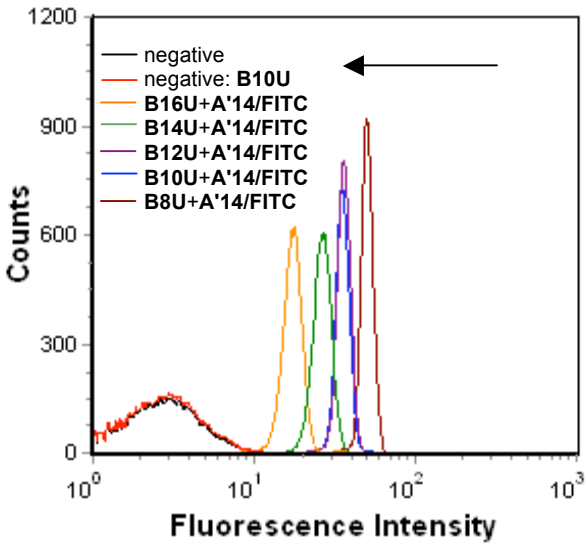

Figure 5.2.2 – Representative fluorescence histogram of suspensions of DNA-functionalized (**A20**) microspheres incubated with FITC-labeled secondary target strands. Microspheres were first incubated with unlabeled (U) primary target strands containing 8 (**B8U**), 10 (**B10U**), 12 (**B12U**), 14 (**B14U**) or 16 (**B16U**) base-pair matches for the **A20** probe sequence. Microspheres were then incubated with FITC-labeled target strands containing 14 base pair matches (**A'14/FITC**) for the **A20** probe sequence. The arrow indicates the general trend of decreasing fluorescence intensity as the difference in the base-pair matches between the two target sequences decreases. Negative controls include DNA-functionalized microspheres alone (negative) and incubated with unlabeled primary targets (negative: **B10U**).

To facilitate comparison of secondary hybridization activity of all the candidate secondary targets, Figures 5.2.3 – 5.2.5 show quantitative analysis of the hybridization activity of the same three different secondary targets (**A'12/FITC**, **A'14/FITC**, **A'16/FITC**, respectively). Surface densities are averaged over four different runs for each secondary target and standard deviations are shown as error bars. These results are individually overlaid with the previous results of hybridization activity of primary targets from Figure 2.2.6 in section 2.2 (shown with a dashed line). Figure 5.2.3 shows the results of the 12 base long secondary target, **A'12**, hybridizing to **A20** probes that were

either previously occupied with primary targets, or unhybridized. Moving from left to right on the graph, an increasing number of base pair matches in the primary target, it is seen that the surface density of hybridized **A'12** secondary targets drops from around 5,000 oligos/μm^2 to 1,500 oligos/μm^2. These results indicate, intuitively, that as the number of *primary* target base length increases; the ability for secondary duplexes to form. However, for all cases here, the **A'12** secondary target never reaches a hybridized surface density that is equivalent to its *primary* hybridization density of around 7,000 oligos/μm^2.

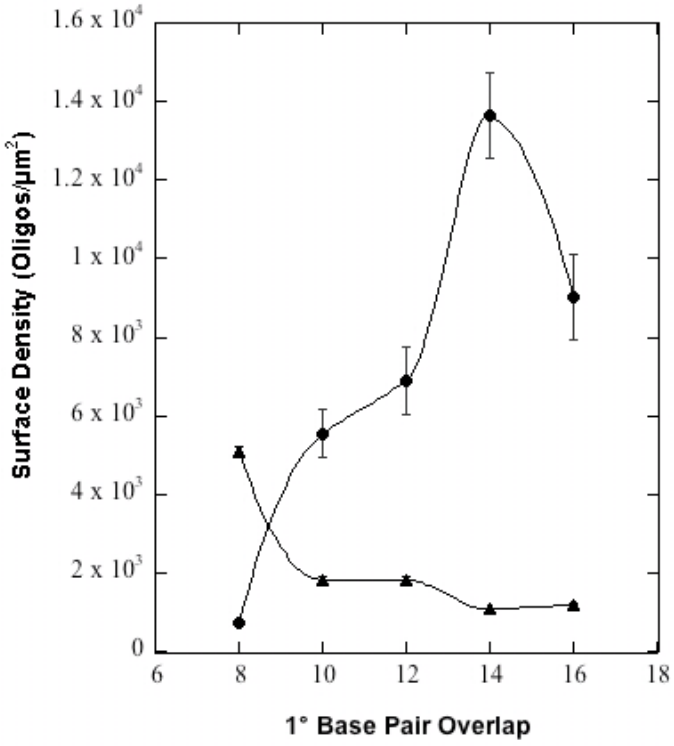

Figure 5.2.3 – Surface density of primary (circles) and secondary (**B12/FITC**, triangles) targets following hybridization with **A20** probes. The primary target length is plotted along the x-axis, with 12 base-long secondary targets displacing that length primary target. A general decrease in secondary hybridization is seen as the length of the primary target to be displaced increases.

Figure 5.2.4 shows results for the 14 base-long target **A'14** acting as the secondary target strand. It is clear that the 14 base-long secondary target has significantly higher hybridization activity then **A'12**. Again, moving from left to right along the x-axis reveals a decrease in secondary hybridization activity as the length of the primary target increases. However, it is observed that this secondary target case has a higher hybridization activity than the primary hybridization activity for **B8**, **B10** and **B12** targets.

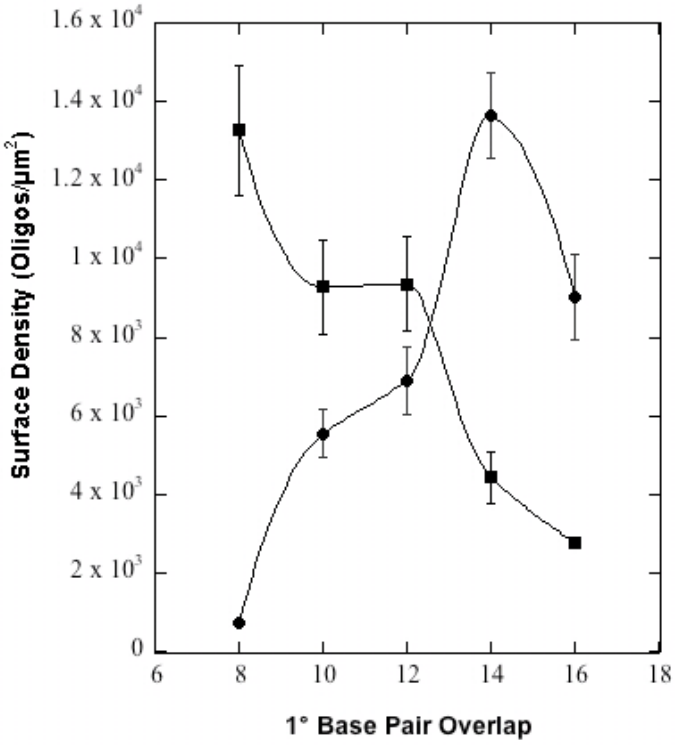

Figure 5.2.4 – Surface density of primary (circles) and secondary (**B14/FITC**, squares) duplexes formed with **A20** probes as a function of primary target length.

Figure 5.2.5 shows results for the final secondary target tested, **A'16**. Similar to results for primary hybridization, the 16 base long target shows less secondary target hybridization activity than the shorter **A'14** target. The same trend of decreasing hybridization activity is again seen as the primary target length increases, indicating that the **A'16** secondary target is less effective as a hybridization partner as the base length of the primary target increases. However, compared to the 14 base secondary target, the overall activity of **A'16** is less.

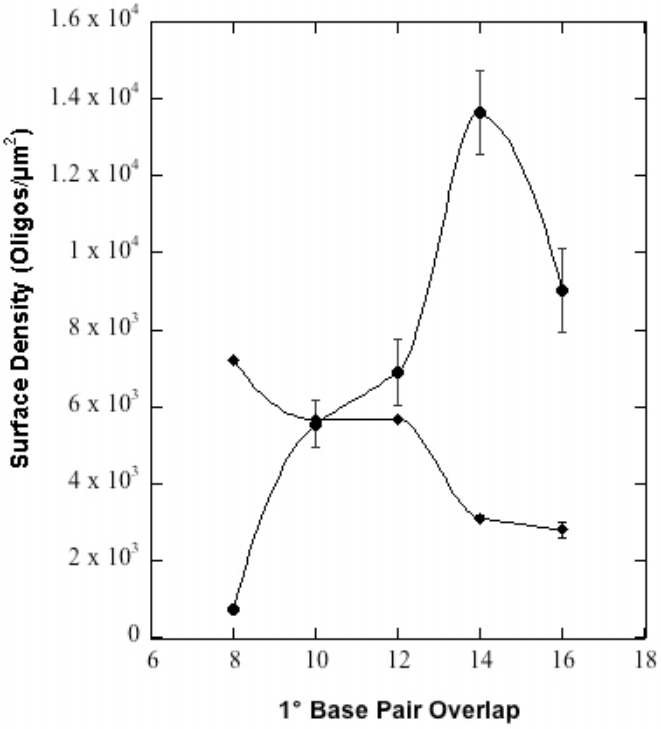

Figure 5.2.5 – Surface density of primary (circles) and secondary (**B16/FITC**, diamonds) duplexes formed with **A20** probes as a function of primary target base length.

In comparing results from primary and secondary hybridization events there is a striking similarity in the role of target sequence length. In the cases of both primary and secondary target the 14 base-long sequence exhibits the highest hybridization activity followed by the 16 base-long and 12 base-long sequences, respectively. However, all three secondary targets exhibit a general decrease in hybridization activity as the length of the primary target strand increases.

5.2.3 - Discussion of Secondary Target Displacement Reaction

In order to explain this apparent contrast in activity between primary and secondary targets, one must consider the two "routes" for the secondary targets to hybridize to the **A20** probes: 1) form duplexes with previously unoccupied **A20** probes or 2) displace the primary target in the original duplex to form a new duplex with **A20** probes. By analyzing the results from Figures 5.2.3 – 5.2.5 with respect to these two routes, a clearer image emerges as to the role played by the sequence length of both the primary and secondary targets. First, as the length of the primary target increase from 8 to 14 bases, the increasing primary hybridization activity leaves fewer probes unoccupied. Second, as the length of the primary targets increases from 8 to 16, the affinity between complementary strands in the duplexes that do form continually increases as indicated by melting temperature calculations shown in Table 5.1.1. Thus, the 8 base-long primary target case is the most likely situation to favor high hybridization activity of the 12, 14 and 16 base-long secondary targets since there are many probe strands left unoccupied by the relatively short primary target and the occupied probes have formed a relatively weak duplex with the 8 base-long primary target. Each of the secondary targets in this case can form a longer duplex with higher affinity value by competitively displacing the original 8

base-long partner strand. In the case of the 14 base-long secondary targets, it appears that all 8 base-long duplexes are displaced since the hybridization activity of 14 base-long primary (13,661 oligos/mm^2) and secondary targets (13,262 oligos/mm^2) are close in value. For the 10 and 12 base-long primary targets, there are fewer probe strands left unoccupied and the duplex strength continually increases, though only modestly between 10 and 12 bases. Thus, overall secondary hybridization activity is less favorable than for 8 base-long primary target case, and approximately equal for the 10 and 12 base long cases. The 14 base-long primary target case is the least favorable situation for significant secondary hybridization activity since there are very few, if any, probes left unoccupied, and a relatively strong duplex already exists with the 14 base-long primary target. The 16 base-long primary target case is an interesting component to this trend of decreasing secondary hybridization activity for increasing primary target length. Compared to the 14 base long primary target, more probes are available for duplex formation with secondary targets; however, since the secondary targets studied are either equivalent to or shorter than the 16 bases there is little drive for competitive displacement of the original target to form a shorter duplex. Thus, unlike the 14 base-pair secondary / 8 base-pair primary target case in which duplexes ultimately involve only the 14 base-long target, here it is likely that we have a mixture of duplexes, the original 16 base-long primary / probe duplex and new duplexes formed between secondary targets and probes previously unoccupied by primary targets. Thus, for all secondary targets, the highest hybridization activity with **A20** probe strands is observed for microspheres first exposed to the shortest primary target **B8**; while the lowest hybridization activity is typically observed for microspheres first exposed to the longer primary targets (**B14** and **B16**). For the 10 base-

long primary target case selected for aggregation, both 14 and 16 base long secondary targets appear to effectively displace the primary target. However, the 14 base competitive target appears most effective at displacing 10 base-long targets and was thus employed for restabilization experiments in the next section.

5.3 - Restabilization of DNA-Linked Microspheres with Competitive Hybridization Events

5.3.1 - Redispersion of DNA-Linked Aggregates with No Dilution of Hybridizing Probe Strand

To investigate the ability of soluble secondary targets to redisperse aggregates (or, displace immobilized targets), **A'14** was introduced to a suspension of microspheres linked by a 10 base-long duplex (**A20**:**B20**) identical to that of the soluble **B10** target. Figure 5.3.1 illustrates the proposed restabilization route for a pair of DNA-linked microspheres, whereby the addition of soluble **A'14** secondary targets causes competitive displacement of **B20** strands. Following DNA-mediated aggregation, the suspension was then incubated with the soluble, secondary targets for 24 hours and then investigated using confocal microscopy. Figure 5.3.2 shows micrographs of a suspension before (b) and after (d) incubation with secondary targets at 100% **A20** loading. It is important to clarify that our approach involves DNA-mediated aggregation (via primary hybridization events) between immobilized strands of **A20** and **B20** to form 10 base-long duplexes (**A20**:**B20**) between complementary microsphere surfaces whereas DNA-mediated restabilization (via secondary hybridization events) involves adding a soluble target to

competitively displace **B20** hybridization partners and form a longer, 14-base duplex (**A20**:**A'14**) which thereby dissociates DNA linkages between microspheres. Here, it is seen that at 100% loading of the **A20** probe, restabilization is NOT complete. It is observed that the large gel-like aggregates do appear to break up into smaller clusters, but that they appear trapped in the aggregated state. This competitive displacement hybridization was carried out to 96 hours, and it is evident that complete redispersion has not occurred. However, earlier results did show that decreasing the number of **A20** probes changed the aggregation profile, and that the weaker, but complete aggregates formed at lower **A20** loadings. Redispersion of these aggregates involving lower **A20** loading is explored next.

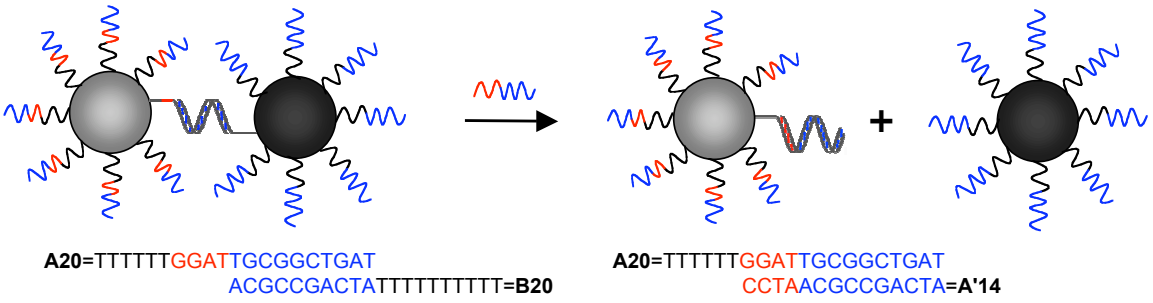

Figure 5.3.1 – Schematic of competitive hybridization approach to drive redispersion of DNA-linked aggregates. On the left, a pair of colloidal particles is shown linked by a 10 base-long duplex. Upon introduction of a longer secondary target strand, competitive hybridization occurs and redispersion results *(2)*. For simplicity, only one duplex is shown between colloidal particles.

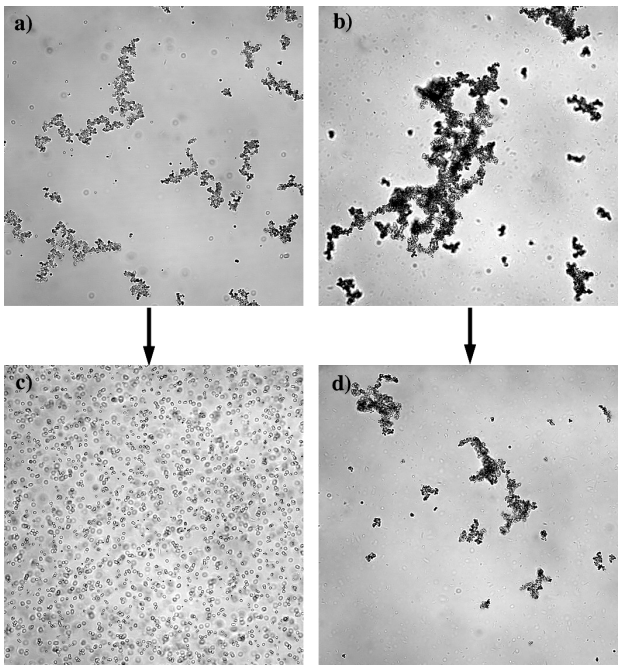

Figure 5.3.2 – Confocal micrographs taken in DIC mode at 40x for microsphere suspensions in which one microsphere population is functionalized with a) 25% and b) 100% **A20** strands while the other microsphere population is functionalized with 100% **B20** strands to form DNA-linked aggregates. These suspensions are then incubated with soluble, secondary targets (**A'14**) and after 24 hours form c) a fluid phase of singlets with occasional doubles and triplets for the 25% **A20** case and d) smaller clusters or aggregates for the 100% **A20** case *(2)*.

5.3.2 - Redispersion of DNA-Linked Aggregates at the Critical Probe Concentration Necessary for Aggregation

In Section 3.3.1, 25% **A20** was identified as the critical probe concentration, ***C*****, necessary to drive DNA-mediated aggregation to completion. Here, the effect of **A20** probe concentration was tested for the 25% and 100% **A20** cases to determine whether reducing the number of active linking strands present in the aggregates increases the likelihood for complete restabilization. Figure 5.3.2 (a) and (c) show micrographs taken for the 25% **A20** suspension system. In this case, the suspension of aggregates shown in Figure 5.3.2 (a) exhibited redispersion into singlets (with only occasional doublets and

triplets) in Figure 5.3.2 (c) after 24 hours of incubation with the **A'14** competitive target strand. This is in contrast to the 100% **A20** suspension that did not show complete particle redispersion. The reason for the lack of a completely restabilized suspension in the 100% case is likely two-fold: a larger number of DNA linkages (maximum of 19) that must be dissociated by the competitive targets as well as the larger cluster size which may hinder the secondary targets from infiltrating the aggregate structure. By reducing the maximum number of linkages present from approximately 19 to 5 for the 25% **A20** system and forming smaller aggregate structures, the competitive strands are capable of displacing enough **B20** strands in the DNA linkages to cause redispersion of the microspheres. Two sets of control experiments were run to test for secondary hybridization events. First, soluble, noncomplementary competitive targets (**NC20**) were added to the 25% **A20** suspension system in place of the soluble competitive targets **A'14**. In that case, no change in aggregate structure was observed after 24 hours, indicating that it is the specific hybridization of **A'14** to the **A20** probe strand that causes oligonucleotide displacement and subsequent disassembly of the aggregate structure. As a second control, soluble secondary targets were added when the two particle populations (**A20** and **B20**) were first mixed together. Even after 48 hours no aggregation was evident. Compared to the collision rate of complementary microspheres to induce DNA-mediated adhesion, the soluble **A'14** strands are likely to diffuse quickly to hybridize to the **A20**-functionalized surface and thereby hinder (10 base-long) duplex formation between immobilized strands. Since the stability of the 14 base-long duplex is greater than that of a prospective 10 base-long duplex, competitive displacement to form the

shorter duplexes (necessary for aggregation) is not favorable and microspheres remain as dispersed singlets in the suspension.

5.3.3 - Redispersion of DNA-Linked Colloidal Satellites

Competitive hybridization was next performed on DNA-linked binary satellite structures consisting of a 5.01 μm template particle linked via a 10 base-long duplex to 1.04 μm red fluorescent shell particles as shown in Figure 5.3.3. Assemblies were incubated in PBS/Tween solution along with 5.0 μM of **A'14/U** secondary target. The assembly was then imaged via confocal microscopy to test for redispersion at 24 hours. As seen in Figures 5.3.3, complete redispersion is observed. However, in these situations, diluent strands are *not* required for complete redispersion to occur. As discussed previous in 3.3.4, assembly itself was not possible when **A20** probes were titrated with any diluent strands. This likely indicates that the duplex density of DNA linkages for forming colloidal satellites is already at the critical concentration, ***C****. For this reason, only a few duplexes must be displaced to cause satellite particle redispersion, even at 100% probe loading.

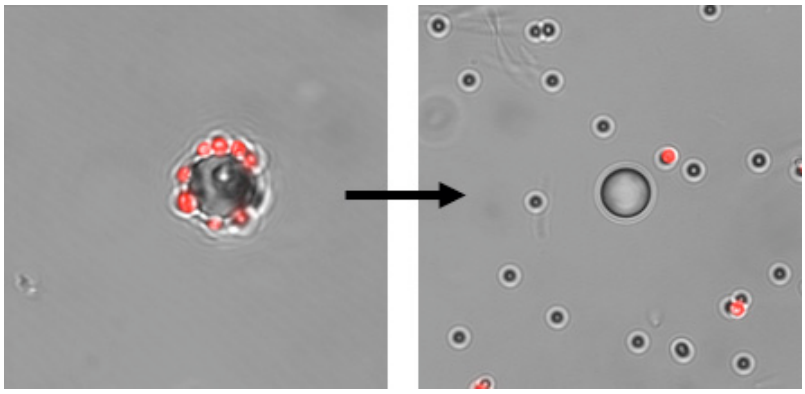

Figure 5.3.3 – Confocal micrograph shows a representative colloidal satellite structure assembled via a 10 base-long overlap (left) and disassembled after incubation with 5.0 μM **B14** secondary target strand for 24 hours *(2)*.

5.4 – Conclusions

This chapter outlined optimizing competitive hybridization to drive programmed redispersion of DNA-linked colloidal structures. First, soluble primary targets were displaced by soluble secondary targets of varying length and an optimal dual target system was selected. Following selection of the 14 base-long secondary target, we investigated its ability to redisperse colloidal structures linked by the selected 10 base-long duplexes. By optimizing the number of **A20** probes present using diluent strands, we found that 1.04 μm aggregates could by completely redispersed by adding the 14 base-long secondary target strand. For the colloidal satellite assemblies, already linked with low avidity, no dilution was required for complete redispersion by the same strand. In summary, this disassembly approach does not require changes in either ionic conditions or temperature, and provides a potential mechanism for reversing DNA-mediated adhesion in isothermal environments. To the best of our knowledge, this is the first reported use of DNA as a programmable, isothermal disassembly tool.

References

1. IDT. *SciTools Oligo Analyzer*. **2009**; Accessed 10/9/2007. Available from: http://www.idtdna.com/analyzer/Applications/OligoAnalyzer/.

2. Tison, C.K. and Milam, V.T. *Langmuir*, **2007**. *23*. 9728-36.

3. Biancaniello, P.L., Crocker, J.C., Hammer, D.A., and Milam, V.T. *Langmuir*, **2007**. *23*. 2688-93.

CHAPTER 6

Kinetics of Competitive Displacement of Soluble, Primary Targets

One of the more exciting aspects of using DNA as a programmable assembly tool for biomaterials applications is the ability to trigger the release of particles from a substrate through competitive hybridization events (as illustrated in the previous chapter). These "satellite" particles may carry imaging moieties, pharmaceuticals, or other particles for use in drug delivery. In the next two chapters we investigate the kinetics of competitive displacement and show that the timing and extent of release can be tuned through choices in the DNA characteristics (e.g. base-length, concentration, etc.) First, displacement of soluble primary targets by soluble secondary targets is monitored by flow cytometry. Both the effects of secondary target length and concentration are investigated and results are plotted as the fraction of primary targets displaced as a function of time. Next, this replacement data is fit to a first order equation to determine the observed replacement rate, k_{obs}. By plotting k_{obs} versus the concentration of different secondary target strands it is revealed that significant competitive hybridization activity (over 50% displacement of primary targets) can be activated or turned-on. This data yields insights into the use of DNA in bead-based microarrays and colorimetric sensors. Taken together, this data reveals that DNA can be used as a trigger for programming the kinetics and extent of soluble target displacement; Chapter 7 will investigate these reactions for displacing immobilized targets that link smaller particles to a larger template particle in colloidal satellite assemblies.

6.1 - Experimental Methods and Techniques

6.1.1 - Oligonucleotide and Particle Selection

Unlabeled, aminated, and FITC-labeled DNA was purchased from Invitrogen. Strands were handled and stored as previously described. Hybridization segments are identical to those used in Chapter 2. These sequences possess moderate duplex melting temperatures and self-melt temperatures well below room temperature as shown calculated previously. All sequences are shown in Table 6.1.1. The combination of low self-melt temperatures and moderate duplex melting temperatures indicates that the probability of both duplex formation between identical strands and the formation of loops or hairpins within a single strand is low. For this chapter, strand nomenclature is as follows. Surface immobilized probes are 20 base-long strands, **A20**. All bases in the soluble strands (labeled **A'** and **B**) will be involved in hybridization events with the surface-immobilized probe. For Chapters 6 and 7, primary target hybridization events will always occur with a FITC-labeled target (**A'10**), always of 10 bases. For secondary (or competitive) hybridization, unlabeled **B** strands of various base length (from 8 to 16 bases) are utilized. It is important to realize that **A'10** strands are identical to **B10** strands, but are used exclusively for primary hybridization and are labeled with a FITC fluorophore. The concentration of primary strands hybridized to surfaces is measured via flow cytometry, and the concentration of secondary strands introduced is modulated by diluting aliquots of the secondary target in TE storage buffer. Consistent with experimental protocols from prior chapters, all hybridization and assembly protocols are performed in PBS/Tween buffer.

6.1.2 - Particle Preparation for Immobilized Target Experiments

Non-fluorescent 5.01 μm carboxylated polystyrene particles (Bangs Laboratories, Fishers, IN) were immobilized with **A20** strands using EDAC chemistry as previously detailed.

Table 6.1.1 – Oligonucleotide sequences and theoretical (duplex) solution melting temperatures used for competitive kinetics studies *(1)*. All bases in soluble targets are intended for complementary hybridization to the **A20** probe strands.

function	sequence	T_m
immobilized probe	**A20** = 5′ - TTTTTTGGATTGCGGCTGAT - 3′	NA
	B20 = 3′ - ACGCCGACTATTTTTTTTTT - 5′	72.0 °C
soluble, FITC-labeled, primary target	**A′10** = 3′ - ACGCCGACTA - 5′	72.0 °C
soluble, unlabeled, competitive target	**B8** = 3′ - GCCGACTA - 5′	61.5 °C
	B10 = 3′ - ACGCCGACTA - 5′	72.0 °C
	B12 = 3′ - ATACGCCGACTA - 5′	70.2 °C
	B14 = 3′ - CCATACGCCGACTA - 5′	74.4 °C
	B16 = 3′ - AACCATACGCCGACTA - 5′	75.9 °C
soluble, non-complementary secondary target for flow cytometry studies	**NC14** = 3′ - GGATTGCGGCTGAT - 5′	NA
soluble, non-complementary target for disassembly studies (Chapter 7)	**ImNC14** = 3′ - TTTTTTTTTTTTTTT - 5′	NA

6.1.3 - Flow Cytometry

The use of FITC-labeled primary targets allows one to measure the primary hybridization activity using flow cytometry. Further, as unlabeled secondary targets are added to competitively displace the primary target (whether present as a soluble FITC-labeled target or immobilized to serve as a linkage between particle surfaces), flow cytometry can be used to monitor the kinetics of primary target displacement by measuring the changes in fluorescence intensity associated with the "tagged"

microspheres over time. In previous chapters we utilized unlabeled primary targets and fluorescently labeled secondary targets in order to monitor all secondary hybridization events arising from secondary duplexes that form with either occupied or unoccupied probes. Here, we are only interested in exclusively monitoring secondary hybridization events stemming from competitive displacement of the labeled, primary (or original) hybridization partner. For the soluble primary target case, bead-based Quantum MESF Medium flow cytometry standards (Bangs Laboratories) can be used to approximate the surface density of hybridized target strands using calibration curves derived from the standards for the molecules of equivalent soluble fluorochrome (MESF). This allows us to quantitatively monitor the changes in surface density of primary targets over time due to competitive hybridization as shown schematically in Figure 6.1.1.

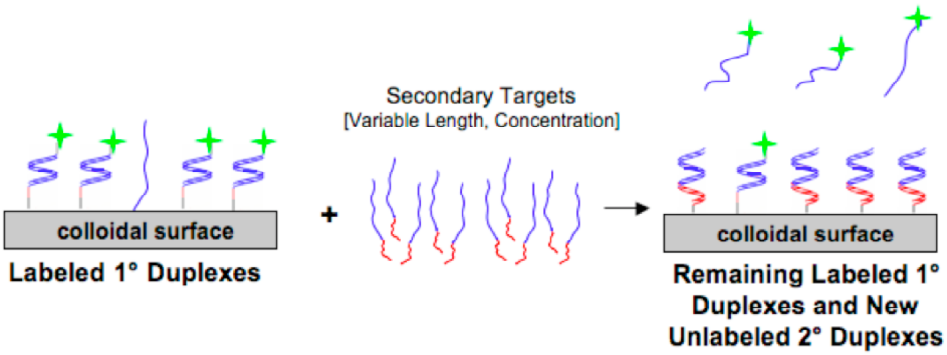

Figure 6.1.1 – Schematic of primary target replacement upon competitive hybridization with longer secondary targets. Fluorescently labeled targets (left) are displaced by secondary unlabeled targets (middle) resulting in their removal from the surface. The decrease in fluorescence intensity associated with removal of fluorescently labeled primary targets can be monitored via flow cytometry.

Briefly, a 200 μL aliquot of particles hybridized with primary targets was resuspended by gentle vortexing (three different coupled batches are utilized, each hybridized with primary targets in one set, resulting in three sets of primary hybridized samples that are then subjected to secondary target hybridization). A 20 μL volume of the sample was removed as a positive control and flow cytometry was performed to determine the fluorescence intensity at $t = 0$. Next, 20 μL of secondary target was added to the remaining suspension at 10 times the desired concentration (i.e., for the 10 nM case, 20 μL of 100 nM secondary target was added, resulting in 10 nM secondary target concentration in the suspension). After the secondary target was introduced, it was gently vortexed and then incubated on a Roto-Mixer for various times (between 1 min and 24 hours). At the specified time, 20 μL of the suspension was removed, washed, and investigated using flow cytometry. For short time points, samples are centrifuged at 15.0 kG for 30 seconds and timed so that the first centrifugation cycle is completed (and particles are therefore removed from suspension with displaced targets) at the reported time. This approach was taken in order to accurately capture the competitive reaction at the time reported. Figure 6.1.2 shows a representative histogram of the decreasing fluorescence intensity that is observed as 14 base-long secondary targets displace 10 base-long primary targets over time.

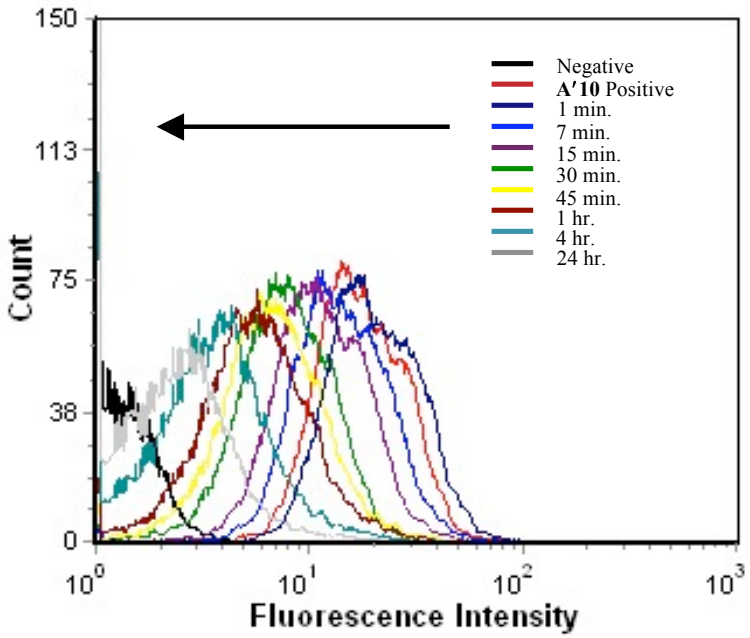

Figure 6.1.2 – Representative histogram of **A20**-functionalized, 5.01 µm colloidal particles hybridized initially to labeled **B10** primary targets and then incubated with unlabeled **B14** secondary targets for the indicated times. The arrow indicates a decrease in fluorescence intensity that occurs as the incubation time with secondary targets increases.

6.2 – Results

6.2.1 – Displacement of Soluble Primary Targets

6.2.1.1 – Effect of Secondary Target Length on Primary Target Displacement

First, the surface density of hybridized soluble **A'10/FITC** targets on **A20** immobilized 5.01 µm particles was measured using flow cytometry. Controls were also run to check for non-specific association of targets with either the immobilized probes or the particle surface. These controls were, 1) **A20**-coupled 5.01 µm particles as a negative, and 2) **A20**-coupled particles incubated with noncomplementary **NC14/FITC** targets.

Both controls showed no difference in fluorescence intensity as seen in Figure 6.2.1, indicating non-specific association of the targets is negligible. **A20** particles were incubated with **A'10/FITC** targets for varying times from 1 hour to 24 hours. It was seen that the surface density of hybridized targets plateaus at approximately 6 hours with a surface density of 1,219 oligos/μm^2. The reasons for the lower overall target hybridization activity for these larger microspheres (compared to the 1.04 µm microspheres) case are discussed in section 2.2.3.

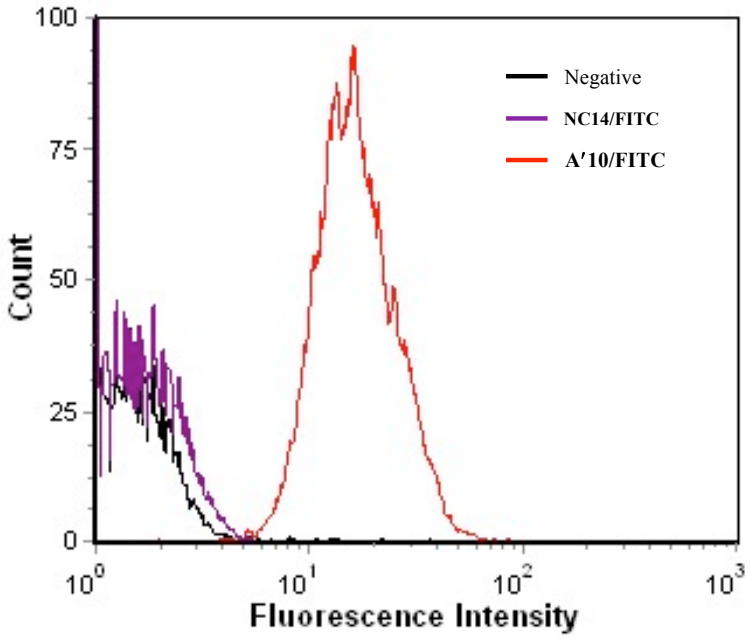

Figure 6.2.1 – Representative histogram showing negligible differences in fluorescence intensity of **A20**-functionalized 5.01 µm colloidal particles alone (Negative) or incubated with FITC-labeled noncomplementary targets. Compared to the controls, the positive sample (**A'10/FITC**) shows a dramatic increase in fluorescence intensity.

Following primary target hybridization with **A'10/FITC**, soluble secondary strands of varying base-lengths (8-16) were added to the particle suspensions (as shown schematically in Figure 6.1.1) at 10.0 μM concentration. Here, the 8 base-long secondary target is even shorter than the 10 base primary duplex, and the 16 base-long secondary target possesses the greatest length difference of 6 bases compared to the primary duplex. The drop in fluorescence intensity over time was then used to analyze the kinetics of target displacement (Figure 6.1.1 shows a representative histogram for the **B14** secondary case). Each of the four sets (split between two different coupled batches) is normalized with respect to non-specific displacement and reported with error shown as the standard deviation. These results were compared to two controls, 1) a positive sample incubated at room temperature in PBS/Tween buffer (no secondary target added), and 2) a positive sample incubated with a noncomplementary **NC14** competitive target. Note: while the **NC14** strand consists of an identical sequence as the hybridization segment of the **A20**, the inversion of the 5' and 3' ends in the **NC14** sequence would only allow duplexes to form in a parallel, and thus unfavorable, conformation. The fraction of primary targets displaced was then measured by comparing the surface density of FITC-labeled primary targets remaining at the specified time to the original surface density of the positive at t = 0, after first accounting for the small fraction of targets (consistently less than 5%) which appear to dissociate (in the absence of complementary secondary targets) as shown in Figure 6.2.2. The noncomplementary control showed only a very small leftward shift in fluorescence intensity as compared to the other control in which no secondary targets are added.

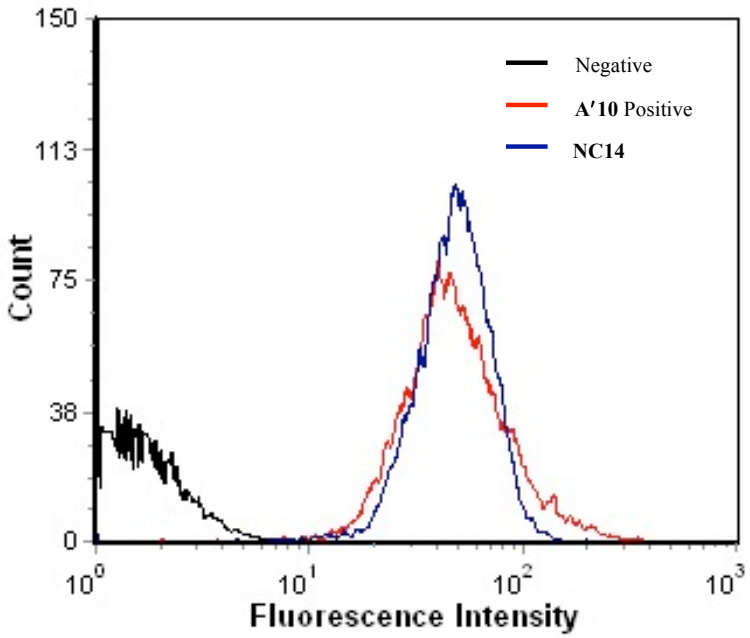

Figure 6.2.2 – Representative histogram showing only a very small shift in fluorescence intensity for particles possessing **A20:B10** duplexes and then incubated with unlabeled, noncomplementary **NC14** targets.

Compared to the nearly negligible shifts in the negative controls, the representative histogram shown in Figure 6.2.3 illustrates the more dramatic decrease in fluorescence intensity associated with incubating the suspensions with complementary secondary target strands of varying base-length and 10.0 μM concentration for 24 hours. Figure 6.2.4 summarizes the time-dependent results of multiple runs at varying concentrations for the six secondary targets. It is clear that at the high secondary target concentration of 10.0 μM, length does play a role in determining the extent of primary target displacement. First, the 8 base-long target, **B8,** shows negligible displacement out to 24 hours, with less than 10% of the 10 base-long primary target displaced. This result is expected, as the 8 base-long secondary target has a lower affinity for the probe than the

original 10 base-long primary hybridization partner. In order for any displacement to occur, a portion of the 10 base duplex must "unzip" (unlikely at room temperature since the **A20:A'10** duplex T_m is 72.0 °C) to allow for the 8 base secondary target to undergo significant hybridization activity with formerly occupied probes. As the secondary target length is increased to 10 bases for the **B10** case, moderate displacement is seen to occur. For the 10 base-long secondary target displacing the 10 base-long primary target, both targets possess the same affinity for the **A20** probe. Upon further increases in secondary target length to strands of greater length than the primary target, near complete displacement is observed. However, for the **B12**, **B14**, and **B16** secondary targets, little difference in the extent of displacement is observed after 24 hours at the highest concentration of 10.0 μM.

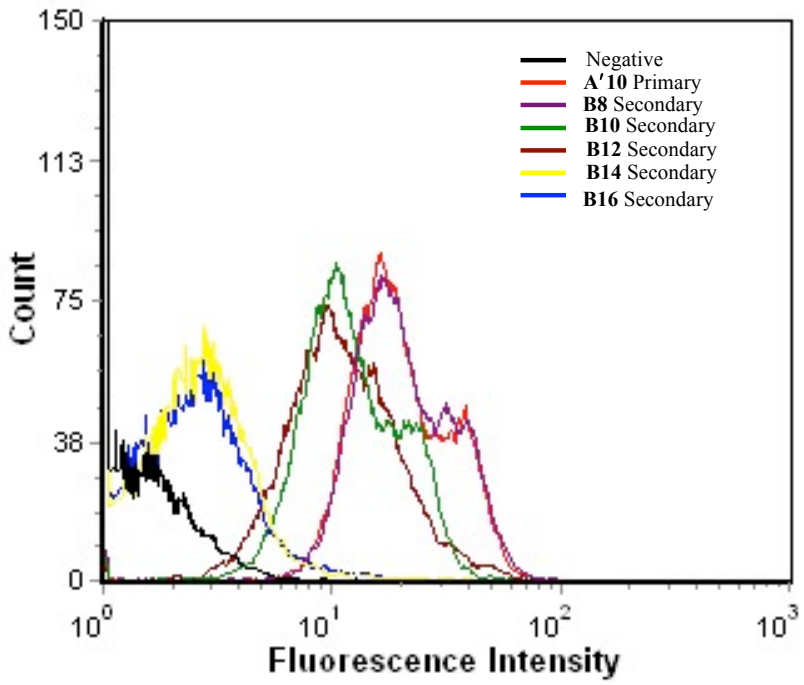

Figure 6.2.3 – Representative histogram showing decreased fluorescence intensity after 24 hours of incubation with secondary targets of varying base length at 10.0 μM concentration. The labeled primary target is a 10 base-long strand (**A'10**).

For these three longer strands, a significant fraction (~70%) of the primary target is displaced within the first one hour, with the replacement rate slowing dramatically at longer times until a plateau is reached. For each of the longer secondary targets, it is difficult to distinguish any subtle differences in the kinetics of competitive hybridization events – replacement rate analysis in section 6.3.1 will better help distinguish the behavior of these three targets. It is noted that the **B12** case does show slightly slower competitive hybridization activity (as indicated by a more gradual plateau) in the first 4 hours, but ultimately reaches approximately the same extent of competitive hybridization activity as both the **B14** and **B16** secondary targets. In order to further explore the effects of base length differences and to further tune the extent and rate of primary target

displacement, we next explore the effect of secondary target concentration on displacement.

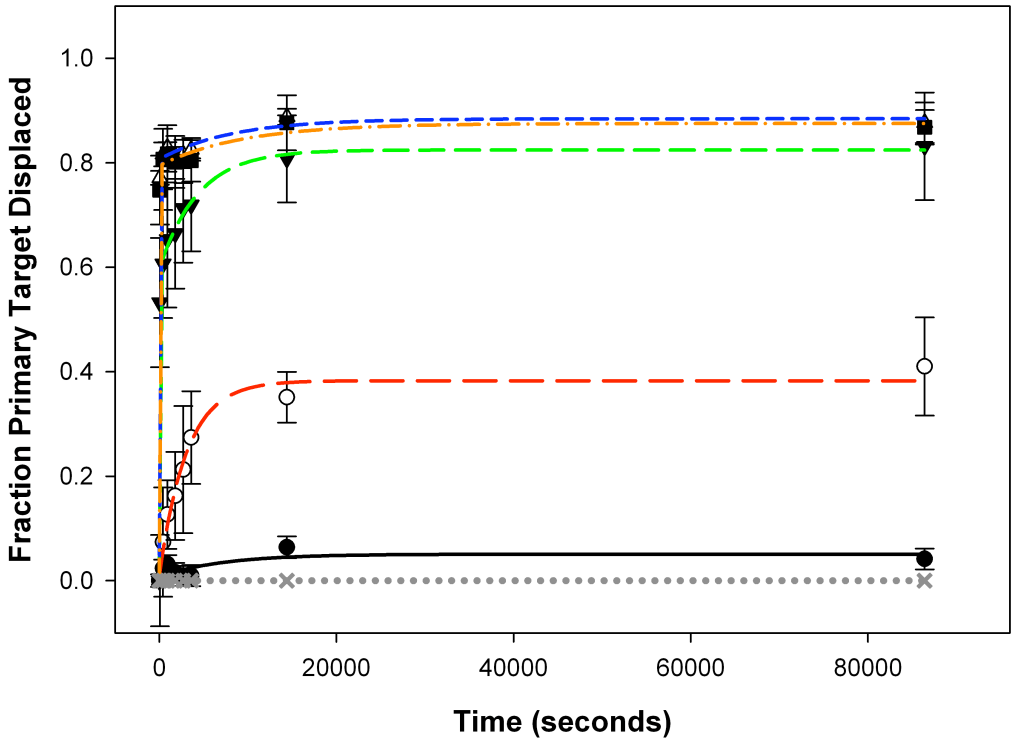

Figure 6.2.4 – Long-time (24 hour) dependent displacement of 10 base-long primary targets by secondary targets of different base lengths at 10.0 μM concentration. Secondary target symbols are as follows: **NC14** (grey, dotted, x), **B8** (black, solid line), **B10** (red, long dash), **B12** (green, medium dash), **B14** (blue, short dash) and **B16** (orange, dash-dot) all shown. Results shown averaged over 4 sets with standard deviation.

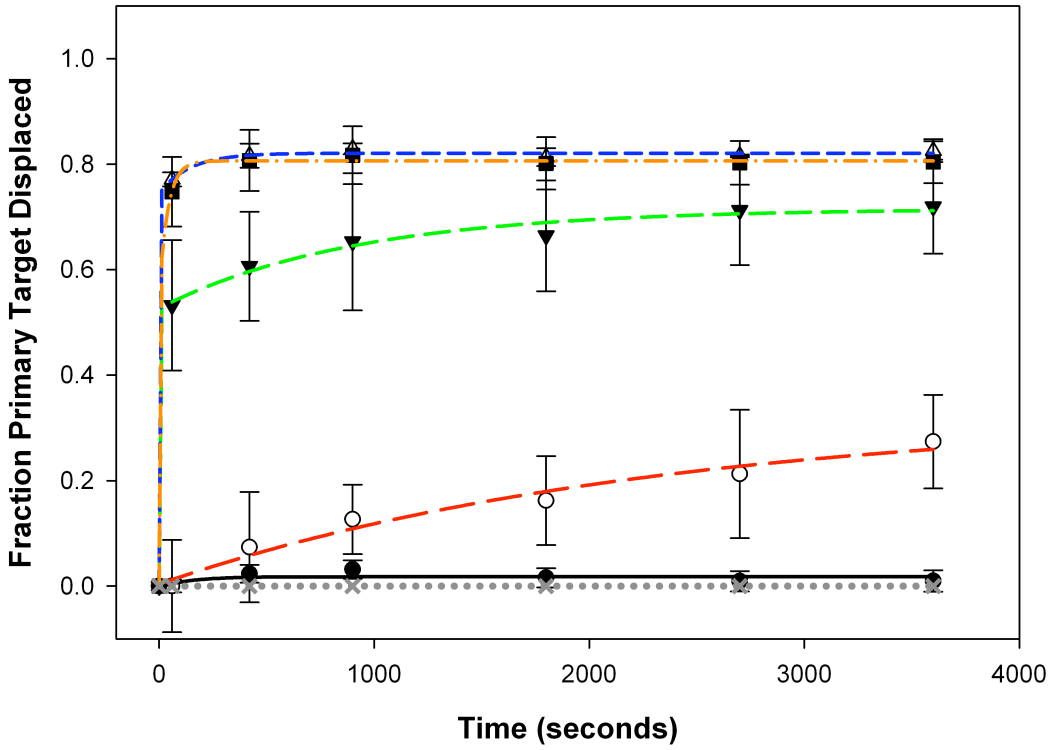

Figure 6.2.5 – Short-time (1 hour) dependent displacement of 10 base-long primary targets by secondary targets of different base lengths at 10.0 μM concentration. Secondary target symbols are as follows: **NC14** (grey, dotted, x), **B8** (black, solid line), **B10** (red, long dash), **B12** (green, medium dash), **B14** (blue, short dash) and **B16** (orange, dash-dot) all shown. Results shown averaged over 4 sets with standard deviation.

6.2.1.2 – Effect of Secondary Target Concentration on Primary Target Displacement

The previous section outlined the effect of secondary target length on the fraction of primary targets that are replaced due to competitive hybridization at high concentrations (10.0 μM) of secondary target. Here, we investigate the effect that reducing the concentration of secondary targets has on the total fraction and rate of primary target displacement. We reduce the secondary target concentration over 3 orders

of magnitude, and test each secondary target for each step of that reduction (i.e., secondary target concentrations of 1.0 μM, 0.1 μM and 0.01 μM are tested).

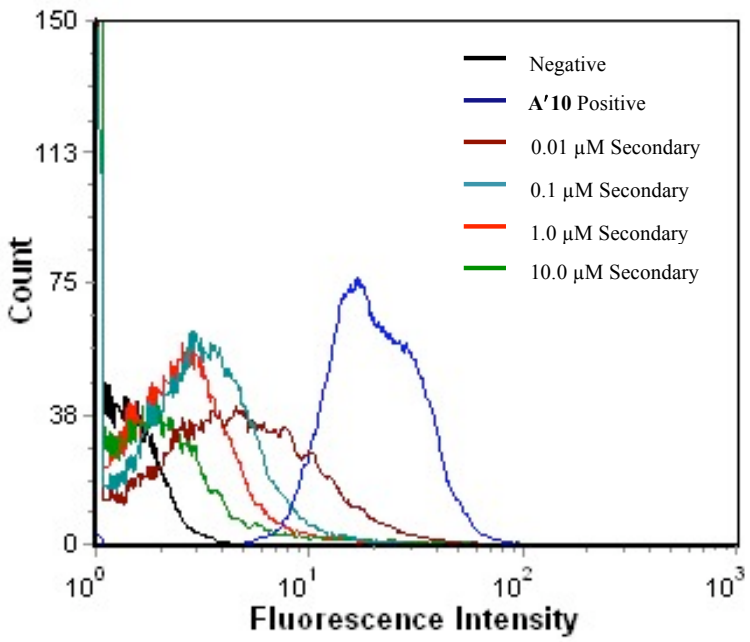

Figure 6.2.6 – Representative histogram shows decreasing fluorescence associated with labeled **A20:A'10** duplexes on microspheres as the concentration of **B14** secondary target is increased. All data was collected following 24 hours of incubation with **B14**.

Figure 6.2.6 shows a representative histogram illustrating the decreasing fluorescence intensity associated with microspheres possessing labeled **A20:A'10** duplexes as the concentration of **B14** secondary target is increased. The 10 nM (0.01 μM) secondary target case is discussed first, and is shown in Figure 6.2.7(a). It is observed that only the 16 base-long secondary target is capable of effectively displacing the 10

base-long primary target over time at this lowest concentration (the inset shows 24 hours competitive hybridization time, with the primary graph showing only the first hour of displacement for clarity). After accounting for thermal dissociation of primary targets, the **B16** secondary target is seen to displace approximately 82% of the **A'10/FITC** primary targets after 24 hours, with the large majority displaced in the first 60 minutes (Appendix D shows the numerical data for all secondary targets and concentrations tested). The **B8** case shows negligible displacement, and all other sequences show less than 30% displacement over 24 hours. Interestingly, the **B10**, **B12** and **B14** secondary targets all show very similar displacement profiles, with a gradual increase in the amount of primary target displaced over time.

Figure 6.2.7(b) shows the results for the 100 nM secondary target case, in which both the 14 and 16 base-long secondary targets are now able to displace greater than 80% of the primary target in 24 hours. Further, for both these strands, the majority of the displacement occurs in the first 60 minutes, with **B14** having a slightly more gradual displacement profile. Again, **B8** displaces a negligible fraction of the primary targets, and both **B10** and **B12** displace approximately 40% of the primary targets. This increase from 0.01 to 0.1 μM reveals that it is possible to "activate" a secondary targets ability to displace the primary target by controlling the concentration. Between 0.01 μM and 0.1 μM, this activation occurs for the 14 base long **B14** secondary targets.

Upon increasing the secondary target concentration to 1 μM, shown in Figure 6.2.7(c), clear differences are revealed in the effect of base-pair length on competitive hybridization kinetics. It is apparent that as the base-pair length is increased, the affinity for target displacement increases. At the 1.0 μM case, **B14** and **B16** are again shown

effective at displacing greater than 80% of the primary target. Here, **B14** is shown *more* effective, which confirms earlier results showing **B14** more efficient at displacing a 10 base duplex that **B16** (see section 5.2.2). Further, **B12** has begun to distinguish itself from the **B10** secondary target, displacing 52% of the primary targets at this concentration. Similar to the previous two concentrations, however, **B10** and **B12** have similar displacement profiles, and have not yet shifted to the dramatic replacement in the first minutes as seen for the **B14** and **B16** targets at this concentration.

Finally, the concentration of secondary targets is increased back to 10.0 μM, as shown in 6.2.7(d) and discussed in section 6.2.1.1. **B12** is observed effective at displacing 83% of the primary targets at this concentration. **B14** and **B16** show negligible changes in displacement from the previous concentrations, **B10** increases, and **B8** is still seen to displace negligible primary targets. These results, combined, reveal the ability to "activate" certain secondary targets as effective competitors by either increasing the concentration or base length of the secondary target. Further, all graphs reveal the speed at which this displacement occurs, with the large majority of the displaced strands departing in the first 60 minutes for effective secondary targets. Indeed, even for the 10 nM **B16** case, greater than 62% of the primary targets have been replaced within the first hour, with nearly 40% displaced in the first 15 minutes. To understand the two "phase" behavior in which extremely quick displacement is followed by more gradual displacement, it is important to remember that we are unable to determine whether *complete* primary target hybridization has occurred – it is likely that many of the targets are only partially hybridized at any given time. As DNA hybridization is a highly dynamic system, there are likely transient melting events on a large subset of the

duplexes at any given time. This partial hybridization will result in extremely fast displacement of the partially hybridized population, followed by slower displacement of the targets that have successfully formed a 10 base-long primary duplex. In the next section, we will investigate a first-order equation to curve-fit our data points, and reveal the effect of both secondary target length and concentration on the observed replacement rate constant, k_{obs}.

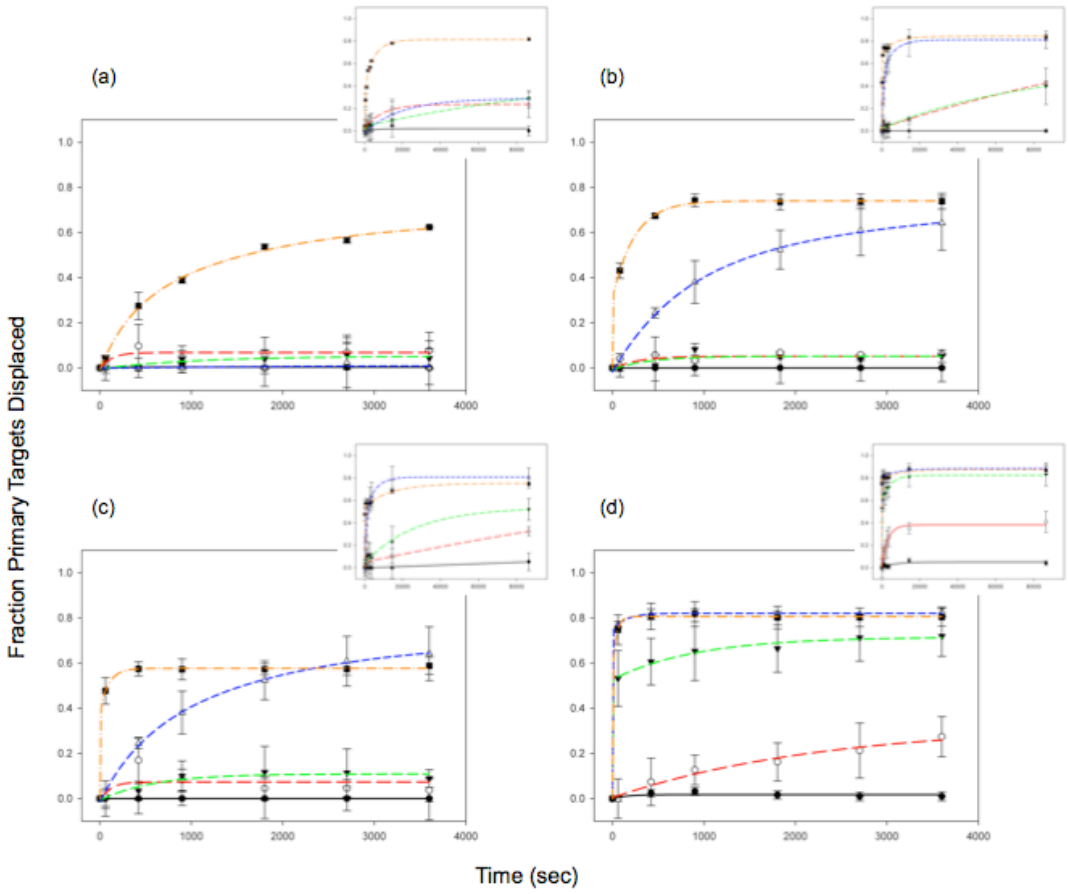

Figure 6.2.7 – Fraction 10 base-long primary target displaced over time for all secondary targets at varying concentrations of a) 10 nM, b) 100 nM, c) 1 µM, and d) 10 µM. Curve fits were generated by fitting data with a first order replacement rate equation. Secondary target symbols are as follows: **B8** (black, solid line), **B10** (red, long dash), **B12** (green, medium dash), **B14** (blue, short dash) and **B16** (orange, dash-dot) are all shown. Primary graphs show displacement out to 1 hr (3600 s) with insets showing the displacement out to 24 hr. Results shown averaged over 4 sets with standard deviation.

6.3 – Rate Constant Analysis

6.3.1 – Replacement Rate Analysis for Soluble Primary Target Displacement by Competitive Hybridization

Utilizing the method employed by Reynaldo et al. to determine the observed replacement rate for oligonucleotide displacement due to competitive hybridization *(2)*, data shown in Figure 6.2.7 was fit to either Equation (1) or (2) using SigmaPlot 11 (Systat Software Inc.)

$$f = f_0 + (f_\infty - f_0)[1 - \exp(-k_{obs}t)] \quad (1)$$

$$f = f_0 + f_{fast}\left[1 - \exp\left(-k_{fast}t\right)\right] + f_{slow}\left[1 - \exp\left(-k_{slow}t\right)\right] \quad (2)$$

Here, f is the fraction primary target displaced at a given time, t, f_0 is the initial fraction displaced (typically at $t = 0$, f_0,= 0), f_∞ is the fraction displaced at equilibrium (defined as occurring at 24 hours), and k_{obs} is the observed replacement rate in s^{-1}. Equation 2 is a two-rate first order equation used for select cases in which two-state displacement activity is observed (i.e., extremely fast initial displacement followed by significantly slower displacement until a plateau is reached). For this equation, f_{fast}, k_{fast}, f_{slow} *and* k_{slow} correspond to the fraction displaced and the rate of displacement in the fast and slow regimes, respectively. For consistency, each set of data is first fit with the single-rate Equation (1). SigmaPlot analysis reports both R^2 values, as well as results for a constant variance test. If R^2 values are greater than 0.90, indicating good fit with given data points,

and the constant variance test is passed, indicating the variance of the dependent variable is constant regardless of the value of the independent variable, then the single rate, k_{obs}, is reported. For the situations in which a single-rate equation does not pass either or both these tests, the two-rate equation is used and both k_{fast} and k_{slow} are reported. For clarity, Figure 6.2.7 (**B14** secondary case) shows both of these equations being employed to fit the data. For the 0.01 μM, a one-rate equation is appropriate since there is a gradual increase in displacement, while for 10.0 μM, a two-rate equation is appropriate since there is a dramatic rate of displacement initially, followed by a slower rise in displacement until a plateau is reached. Figure 6.3.1 shows the observed replacement rate versus secondary target concentration for each of the secondary targets tested. For the single-rate (Equation 1) cases, k_{obs} is reported; while for the two-rate systems, k_{fast} is reported, as it dominates the replacement rate behaviour. It is evident that the 8 and 10 base long secondary targets have slow or negligible displacement rates at all concentrations, with k_{obs} values below 10^{-4} s^{-1} at the highest concentration of 10 μM. As the secondary target length is increased, the concentration at which displacement occurs relatively quickly (defined arbitrarily as greater than 10^{-4} s^{-1}) continually decreases. For the **B12** target, it requires 10 μM secondary target to get the high displacement rate of 3.66×10^{-2} s^{-1}. For the **B14** case, the replacement rate passes 6.0×10^{-4} s^{-1} at the low concentration of 100 nM, and is above 1.59×10^{-2} s^{-1} at the 1 μM concentration. Finally, for the **B16** secondary target, relatively fast displacement of 6.0×10^{-4} s^{-1} is seen even at 10 nM target, which increases to 4.70×10^{-2} s^{-1} at the 10 μM concentration. This same data is next plotted as k_{obs} vs. secondary target length for each secondary target concentration. Again, the activation behavior is clearly observed. It is also possible to see

B14 has a greater replacement rate than **B16** at the 10.0 μM case – further confirmation that for the 10 base primary duplex, there is an "optimal" secondary target for displacement, and it depends strongly on the concentration of that target in solution. Table 6.3.1 shows the measured replacement rates for all cases with the single-rate cases reporting k_{obs} as k_{fast}. We hypothesize that this "activation" behavior is due to interplay between the toehold length (difference in base-pair length between primary and secondary targets) of the secondary target and the probability of primary target displacement before secondary target removal. Competition is known to behave as a classic "gamblers ruin" situation *(3)*, where hybridization occurs one nucleotide at a time in either direction until one of the targets (primary or secondary) has been removed. It is known that the shortest stable duplex is approximately 3 nucleotides in length, so for secondary target strands with toehold regions longer than this, the probability of successful "nucleation" of a critical hybridization segment followed by displacement (as hybridization continues) is increased.

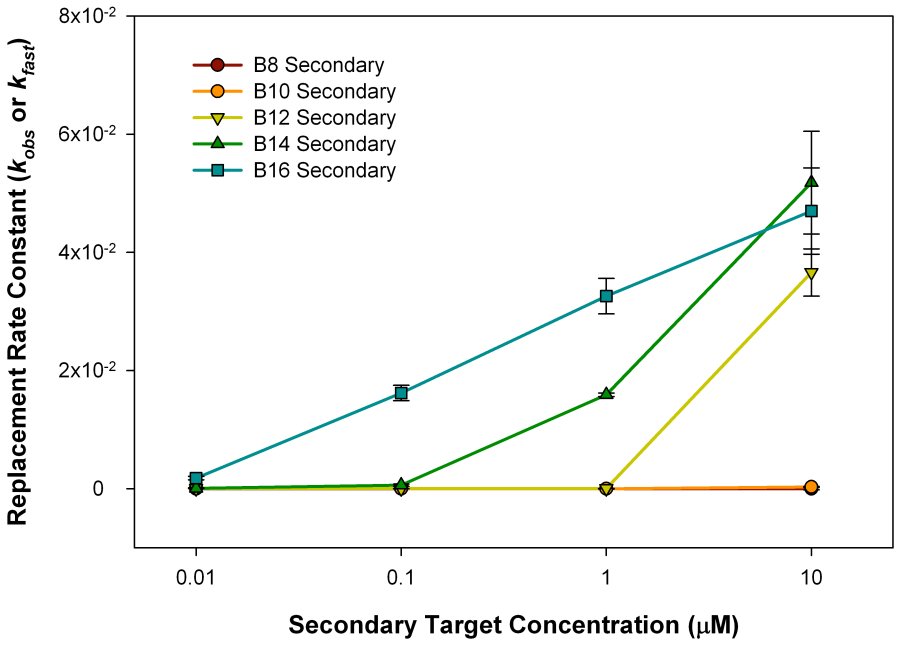

Figure 6.3.1 – Replacement rate constant as a function of secondary target concentration for secondary targets of differing base lengths. For cases in which a two-rate equation is appropriate (i.e., **B14** at 10.0 μM), only the value of k_{fast} is graphed here as the dominant rate constant.

Table 6.3.1 - Observed replacement rate constants for primary target displacement by various secondary targets at specific secondary target concentration. For one-rate cases, k_{obs} is shown as k_{fast}. For two-rate cases, both k_{fast} and k_{slow} are reported separately.

[2° Target] (μM)	B8		B10		B12		B14		B16	
	k_{fast} (s^{-1})	k_{slow} (s^{-1})	k_{fast} (s^{-1})	k_{slow} (s^{-1})	k_{fast} (s^{-1})	k_{slow} (s^{-1})	k_{fast} (s^{-1})	k_{slow} (s^{-1})	k_{fast} (s^{-1})	k_{slow} (s^{-1})
0.01 μM	-	-	**1.00×10^{-5}**	-	**3.12×10^{-5}**	-	**6.05×10^{-5}**	-	**1.80×10^{-3}**	2.00×10^{-4}
0.1 μM	-	-	**4.49×10^{-6}**	-	**1.47×10^{-5}**	-	**1.20×10^{-3}**	2.00×10^{-4}	**1.20×10^{-2}**	1.00×10^{-4}
1.0 μM	-	-	**3.04×10^{-6}**	-	**3.76×10^{-5}**	-	**1.40×10^{-3}**	2.00×10^{-4}	**3.26×10^{-2}**	6.64×10^{-5}
10.0 μM	**2.00×10^{-4}**	-	**4.01×10^{-4}**	-	**3.66×10^{-2}**	2.00×10^{-4}	**5.18×10^{-2}**	1.00×10^{-4}	**4.70×10^{-2}**	1.00×10^{-4}

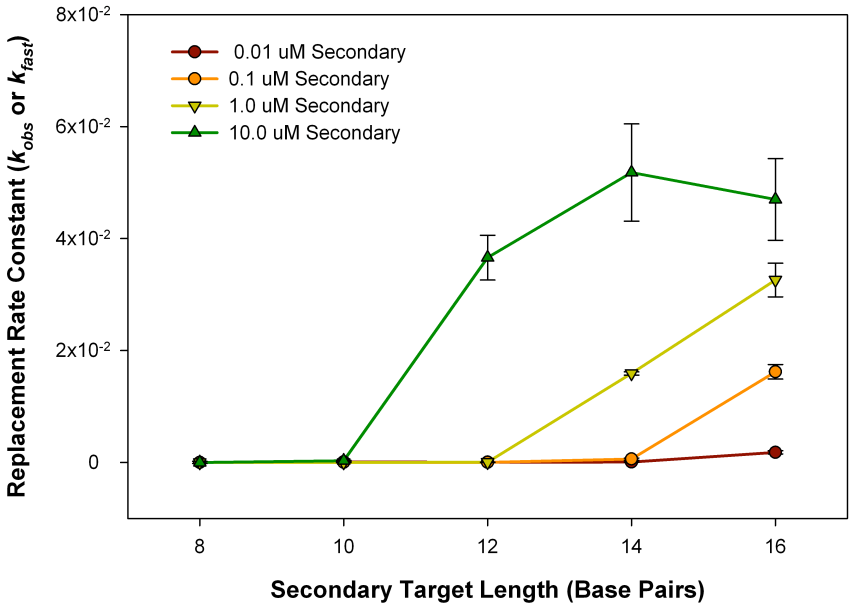

Figure 6.3.2 - Replacement rate constant as a function of secondary target length at different concentrations. For cases in which a two-rate equation is appropriate (i.e., **B14** at 10.0 µM), only the k_{fast} value is plotted here as the dominant rate constant. This data is the same as shown in Table 6.3.1, but the graph reveals the on-off behaviour exhibited by base-pair differences at a given concentration.

Finally, the above replacement rate data is plotted as a three-dimensional contour plot to further elucidate the replacement behavior based upon synergy between base-pair length and secondary target concentration. Crossover points between the x-y plane show individual samples, and allow one to select a system for a specific replacement rate regime. For example, if one desires a replacement rate, k_{obs}, of 2.0 x 10^{-2}, the only option is **B14** at 1.0 µM. For a k_{obs} of 3.0 x 10^{-2}, two options exist – both **B12** at 10.0 µM or **B16** at 1.0 µM. This analysis clearly shows that if one variable is "locked" we are able to determine the value of the second variable (here, the length) required for a certain displacement rate.

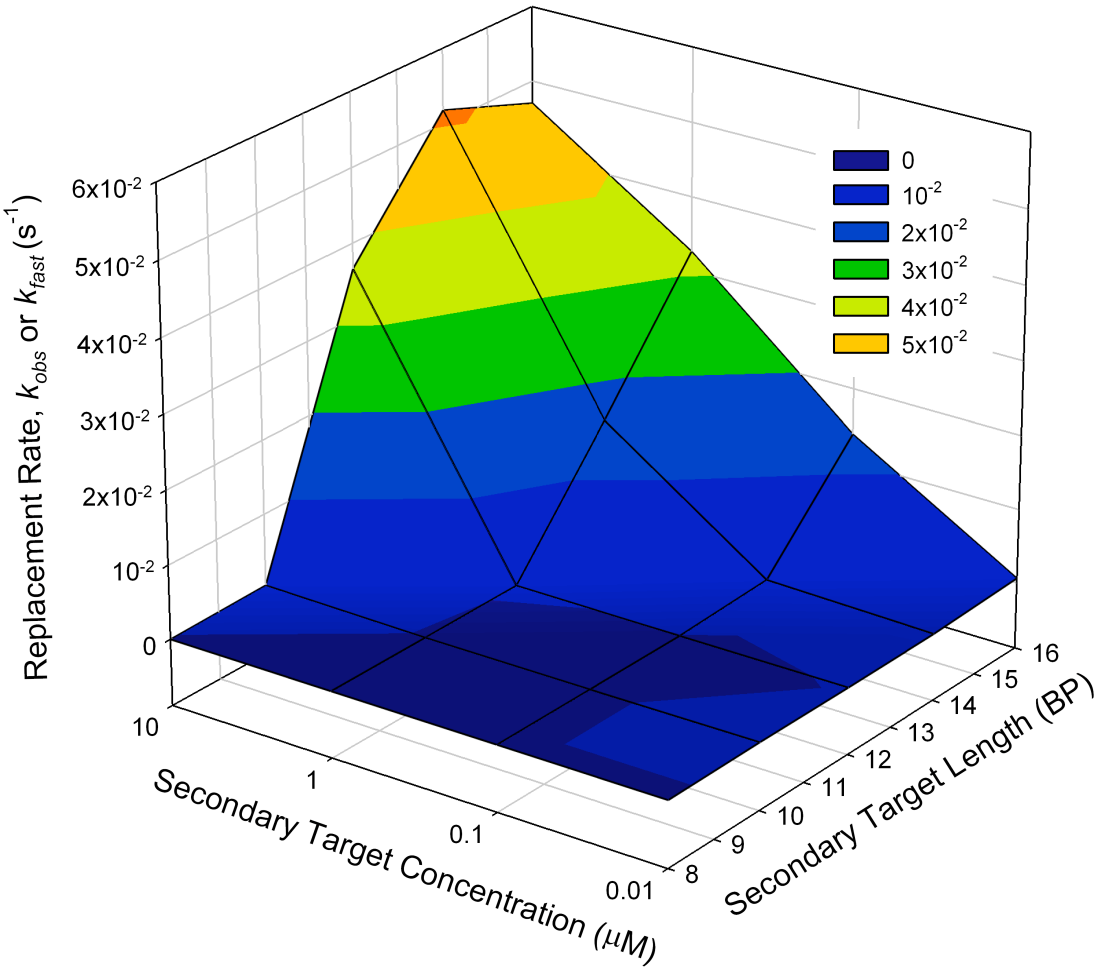

Figure 6.3.3 – Three-dimensional contour plot illustrating the competitive hybridization replacement rate constant can be tuned by selecting a specific secondary target length and concentration. Average over four sets with standard deviation not shown.

6.3.2 – Discussion of Rate Constants

Combined, this data reveals that it is possible to select a specific replacement rate for the system (over a wide range from 10^{-6} to 10^{-2} s^{-1}) by tuning the two variables of secondary target concentration and length (a graph of the replacement rate for 10^{-6} to 10^{-3} s^{-1} is shown in Appendix E). These observed replacement rates for **B12 – B16** are

significantly higher than those determined by Reynaldo *(2)*, due in greater part to the affinity differences of the primary and secondary targets. In the Reynaldo system, an equivalent length secondary target is utilized, while we take advantage of increased affinity of longer secondary targets to drive the displacement reaction. In comparing our **B10** secondary case (equivalent in length to the **A′10** primary target) to Reynaldo's system we find similar replacement rates, indicating that the additional base-pair matches on our secondary targets are indeed responsible for driving the replacement at greatly increased rates. For example, Reynaldo reported a k_{obs} value of 5.6 x 10^{-6} s^{-1} for the 12 base-long primary and secondary targets at 30 °C and 1.0 μM secondary target concentration. This is similar to our k_{obs} value of 2.70 x 10^{-6} s^{-1} for the 10 base-long primary and secondary targets at room temperature and 1.0 μM secondary target concentration.

6.4 – Conclusions

This chapter explored the kinetics of competitive hybridization for the displacement of a *soluble* primary target of 10 bases (**A'10**) by secondary targets of various base lengths and concentrations. After analyzing the fraction primary targets displaced over time, an observed replacement rate constant was determined for each secondary target and concentration tested. It was determined that both length and concentration play an important role in determining the kinetics of the displacement process, and that the ability to tune this rate (within a certain range) is possible. We found that all longer secondary targets are able to displace a significant fraction of the primary

targets at modest or high concentrations. For example, **B14**, with four extra bases than the primary target, is ineffective at displacement when only used at 0.1 μM concentration. When this concentration is increased to 1.0 μM or 10.0 μM, effective displacement occurs. This "on-off" activation character is observed for all longer secondary targets (**B12**, **B14**, **B16**) and to a lesser extent with the equivalent length secondary target, **B10**. Results from this chapter show that DNA can act as a programmable "trigger" for controlled release and provides relevant kinetic data for the bead-based microarray field. This data reveals that DNA is a promising tool for programming isothermal displacement, and the next chapter will investigate its ability to drive isothermal redispersion of DNA-linked colloidal structures.

References

1. IDT. *SciTools Oligo Analyzer*. **2009**; Accessed 6/10/2008. Available from: http://www.idtdna.com/analyzer/Applications/OligoAnalyzer/.

2. Reynaldo, L.P., Vologodskii, A.V., Neri, B.P., and Lyamichev, V.I. *J. Mol. Biol.*, **2000**. *297*. 511-20.

3. Anshelevich, V.V., Vologodskii, A.V., Lukashin, A.V., and Frank-Kamenetskii, M.D. *Biopolymers*, **1984**. *23*. 39-58.

CHAPTER 7

Kinetics of Nanoparticle Release from DNA-Linked Colloidal Assemblies Via Competitive Hybridization Events

The kinetics of releasing fluorescent nanoparticles from DNA-linked colloidal satellite assemblies by competitive hybridization is analyzed in this chapter using a novel extension of flow cytometry. Here, based upon previous results for the 10 base primary target – 14 base secondary target system, we only investigate that secondary target length of interest. The concentration of secondary target is the sole variable, and the same concentrations as used for the soluble case in Chapter 7 are investigated here. It is found that the displacement of nanoparticles is significantly slower than displacement of soluble primary targets, but that high fractions of particles can be released over long time scales (days instead of hours or minutes). This data reveals that competitive hybridization can be used as a programmable, isothermal disassembly tool for DNA-linked colloidal structures. Further, the use of competitive hybridization for the programmed release of a model drug delivery system is shown possible at isothermal conditions.

7.1 – Experimental

7.1.1 – Oligonucleotide Selection

Unlabeled and aminated DNA was purchased from Invitrogen. Strands were handled and stored as previously described. Hybridization segments are identical to those used in the previous chapter. Again, strand nomenclature will follow rules previously laid out. Complementary strands for particle assembly are labeled **A** and **B** followed by the

number of bases in each strand. Particle assembly will always occur with a 10 base-long hybridizing segment on strands **A20** and **B20**. All bases in the soluble strands (here labeled **B**) will be involved in competitive hybridization events. For secondary hybridization, unlabeled **B** strands of 14 bases (**B14**) will be used and will hybridize to a 14 base-long segment on the **A20** probe. As the self-melt temperature for **B14** is low *(1, 2)*, and **B20** has an identical 10 base-pair long segment, hybridization to **B20** is not expected. The average number density of primary strands hybridized to each colloidal particle is measured using flow cytometry, and the concentration of secondary strands introduced will be modulated by diluting aliquots of the target in TE storage buffer. All hybridization and assembly protocols are performed in PBS/Tween buffer as described in section 2.1.2.

7.1.2 – Particle Preparation and Assembly

Nonfluorescent 5.01 μm carboxylated polystyrene particles (Bangs Laboratories) and 200 nm red fluorescent carboxylated polystyrene particles (Molecular Probes) were immobilized with **A20** and **B20** strands, respectively, using EDAC chemistry as previously discussed in Chapter 2. DNA-linked colloidal satellites were assembled to investigate the kinetics of nanoparticle release from assemblies as competitive targets are added to the suspension. Briefly, 5.0 μL of **A20**-functionalized 5.01 μm particles at 0.1% volume fraction were mixed with an excess 20.0 μL **B20** 200 nm particles at 0.1% volume fraction. 75 μL of PBS/Tween hybridization buffer was then added to make a total suspension volume of 100 μL and the mixed suspension was left to incubate for 48 hours. The colloidal micelle suspension is then washed 8 times at 5.2 kG for 5 minutes, to remove any excess, nonadherent nanoparticles in the supernatant. PBS/Tween is then

added to bring the suspension volume back to 100 μL. Following the eighth wash, colloidal satellites are resuspended to 100 μL (for an approximate colloidal satellite concentration of 0.005%) and imaged using both fluorescence and confocal microscopy to check the extent of nanoparticle coverage. The number of washes and centrifugal speed were optimized to remove a significant fraction of the unattached nanoparticles while simultaneously preventing the destruction of the satellite structure due to centrifugation.

7.1.3 – Competitive Hybridization Driving Satellite Disassembly

Following successful colloidal satellite assembly, 10.0 μL is removed from the 100 μL suspension as a positive and imaged to confirm and document DNA-mediated assembly of a colloidal satellite structure. The remaining 90 μL is split into two – 45 μL aliquots. Here, the noncomplementary strand **ImNC14**, a 14 base-long thymine strand (the previously used non-complementary strand **NC14** could not be used as it is complementary to the **B20** strand), is added to one aliquot as an unlabeled target that is noncomplementary to both **A20** and **B20** as a negative control. Various concentrations of complementary **B14** secondary target are added to the second aliquot. The two aliquots are incubated for 24, 48, 72, and 96 hours, with a 10 μL sample being removed from each aliquot at each designated time point. These suspensions are then characterized to examine the extent of nanoparticle release, if any, using both confocal microscopy (qualitative) and flow cytometry (quantitative). The flow cytometry procedure we developed is discussed below

7.1.4 – Flow Cytometry to Quantitatively Monitor the Extent of Nanoparticle Release from Colloidal Satellite Assemblies

Here, flow cytometry is used to monitor the release of 200 nm fluorescent nanoparticles from satellite assemblies due to competitive hybridization events with soluble secondary targets (shown schematically in Figure 7.1.1). In this case, quantifying the actual number of attached nanoparticles is not feasible since calibration standards do not currently exist for the novel experimental approaches involving nanoparticles as fluorescent "tags" instead of the conventional tagged molecular ligands. However, by comparing the fluorescence intensity values over time, the relative differences in nanoparticle coverage can be monitored to assess the extent of nanoparticle release from the assemblies. Further, comparing fluorescence histograms of micelles with confocal microscopy images of the same sample reveals that flow cytometry accurately gauges the number of shell particles remaining (i.e., a fluorescence intensity decrease of 50% from the positive corresponds with images that show approximately half the originally adherent nanoparticles are released). The use of flow cytometry to monitor the characteristics of a particle assembly is relatively new *(3)*, and offers several advantages including the ability to accurately and reproducibly gate specific particle populations by size *(4)*. This characteristic ensures that all fluorescence intensity being monitored is associated with DNA-linked fluorescent nanoparticles. The work presented in this chapter is the first instance of using flow cytometry to analyze changes in the structure of a colloidal assembly. For flow cytometry runs, the aliquoted portion removed from the sample is resuspended to 500 μL in PBS/Tween buffer. This sample is very gently mixed by flicking the tube, and then interrogated by flow cytometry utilizing a FSC vs. SSC dot

plot to gate the population of interest (based on size) and a PerCP-Cy5 fluorescence intensity histogram is generated to count the number of events (i.e., number of individual colloidal satellites) with a measured intensity value. Samples are run until at least 2,500 individual samples are counted *within the gated population*. The gating on the FSC vs. SSC graph shown in Figure 7.1.2 allows specific micelle populations to be interrogated, and therefore allows us to ignore any red fluorescent nanoparticles in solution that are not bound (as they will not be counted in the gated area). Further, this gating can be determined between sample runs across different days, allowing for comparisons between samples over the long time-scales of these experiments. To calculate the fraction of nanoparticles release, the fluorescent intensity at each time point ($t > 0$) is compared to the positive signal at $t = 0$. Additionally, the positive sample (with no secondary target additions but left at room temperature) is run at each time point to confirm that no weakly adherent particles are lost over time at room temperature due to collective dissociation of DNA linkages.

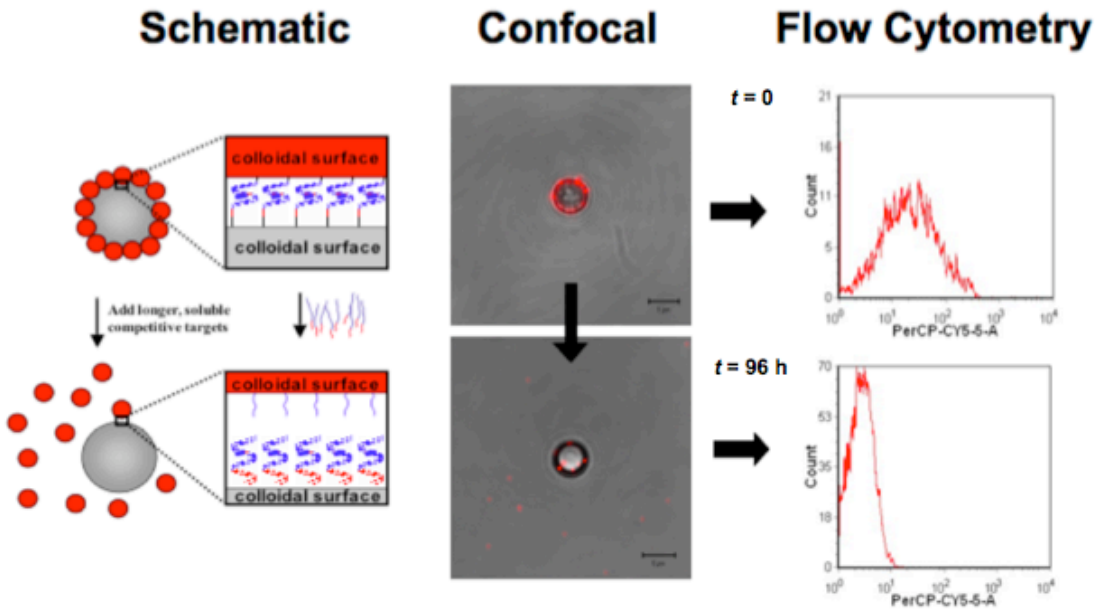

Figure 7.1.1 – Schematic (left), confocal images (middle) and flow cytometry histograms (right) of DNA-linked colloidal satellites (top) that disassembly (bottom) upon addition of secondary targets. Here, DNA linkages are comprised of 10 base-long duplexes whereas secondary duplexes are 14 bases long.

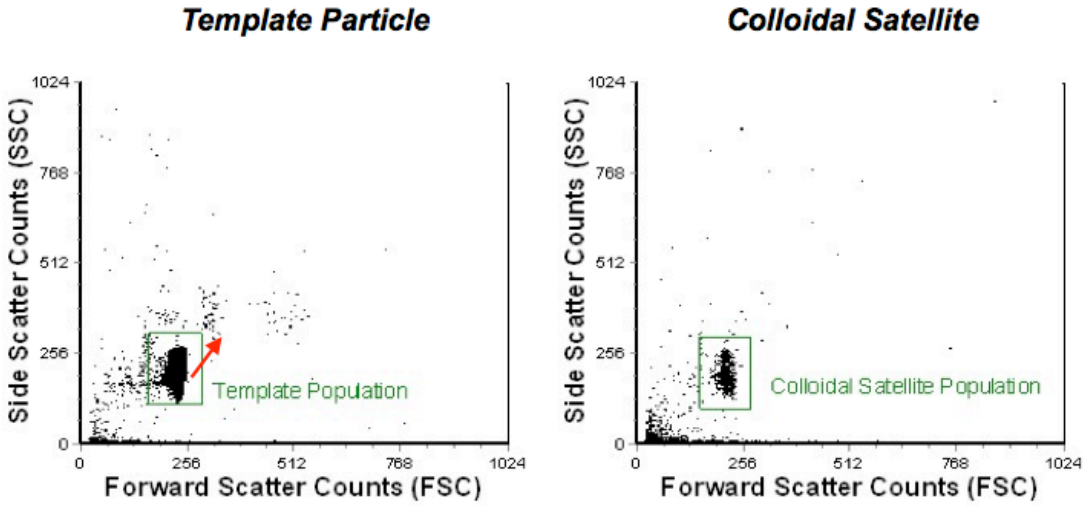

Figure 7.1.2 – Representative dot-plots for forward scatter counts vs. side scatter counts gating of template and colloidal satellite populations. The red arrow indicates the slight shift in gating that occurs as colloidal assembly proceeds.

7.2 – Results

7.2.1 – Colloidal Satellite Assembly Studies

DNA-linked colloidal satellites were first assembled and characterized to determine the relative extent of fluorescent nanoparticle coverage in the DNA-linked shell and the base-line fluorescence intensity associated with a population of colloidal satellites and their maximum nanoparticle coverage. Confocal microscopy revealed near complete coverage for the majority of the 5.01 μm template particles. Figure 7.2.1 shows confocal micrographs of a representative colloidal satellites, along with corresponding fluorescence histograms of the entire population of colloidal satellites. For flow cytometry runs, a suspension of bare 5.01 μm particles is run first to determine the autofluorescence background and to allow for accurate gating on an FSC-SSC dot-plot of individual colloidal satellites (7.2.1 (a)). Figure 7.2.1 (b) shows a histogram of a population of satellites. Compared to Figure 7.2.1 (a) it is observed that the attachment of red fluorescent nanoparticle to the surface of the non-fluorescent colloidal particle causes a significant rightward shift in PerCP-Cy5 fluorescence intensity, resulting in a clear indication that the fluorescent nanoparticles are acting as effective tagging agents.

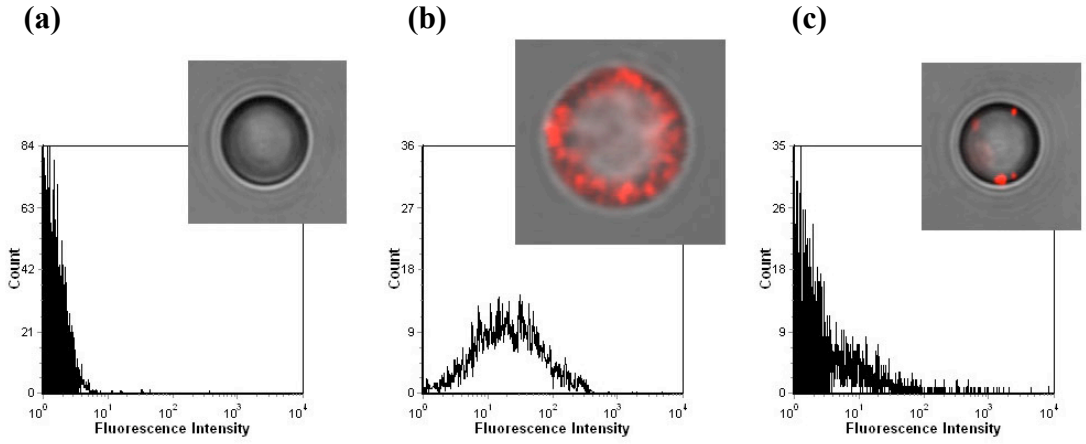

Figure 7.2.1 – Representative confocal microscopy images and corresponding flow cytometry histograms illustrating the colloidal satellite template (a), assembly (b), and disassembly (c) process by DNA hybridization reactions. Assembly is performed with 48 hours of incubation, and the disassembly shown here is after 96 hours with 1.0 μM secondary competitive target.

7.2.2 – Competitive Hybridization Kinetics for Immobilized Target Displacement

The change in fluorescence intensity associated with a population of colloidal micelles is now monitored as unlabeled secondary targets are added to the suspensions. First, controls were run to check for the release of fluorescent nanoparticles due to the collective thermal dissociation of the DNA linkages. These controls include the following samples: 1) a population of satellites incubated in PBS/Tween hybridization buffer alone and washed at each indicated time point; 2) a population of colloidal satellites incubated in 20 μL Tris-EDTA to test for the effects of buffer changes (Note: DNA is stored in Tris-EDTA); and 3) a population of satellites incubated with 10 μM noncomplementary target **ImNC14** to check for possible nonspecific displacement by the noncomplementary target. The above controls show only a small fraction of nanoparticles (less than 10%) is released from the weakly adherent assemblies, as shown in Figure 7.2.2.

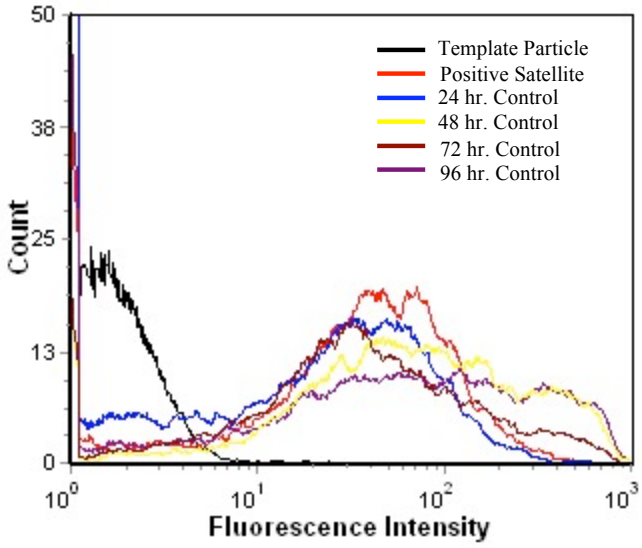

Figure 7.2.2 – Representative fluorescence intensity histogram showing negligible changes in fluorescence intensity associated with a satellite population incubated with noncomplementary secondary targets for up to 96 hours. Similar results were obtained for satellites incubated in DNA storage buffer alone or incubated in PBS/Tween buffer alone.

Figure 7.2.3 shows a representative fluorescence intensity histogram showing the positive colloidal satellite sample run at time t = 0 and 96 hours. It is clear that relatively few, if any, nanoparticles are lost due to mixing and room temperature incubation conditions, as the fluorescence intensity profile is essentially identical at each time point. Similar controls are run at each time point for each sample.

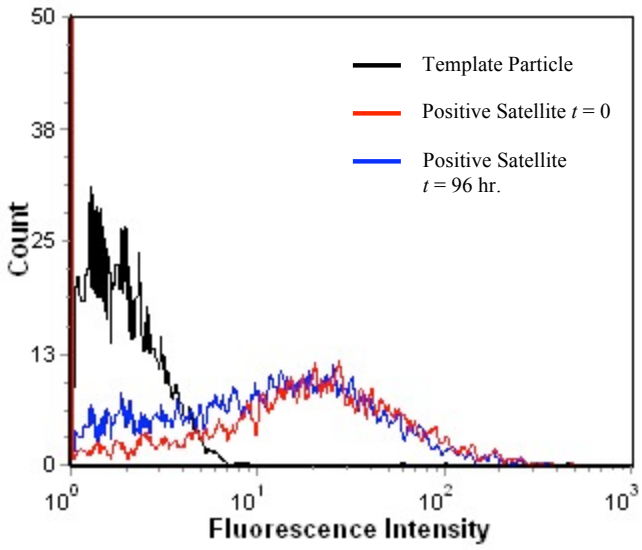

Figure 7.2.3 – Representative fluorescence histogram illustrating negligible change in the fluorescence intensity profile over 96 hours of gentle mixing of a population of colloidal satellites at room temperature.

Figure 7.2.4 shows a representative histogram for colloidal satellites incubated with the complementary, 14 base-long secondary target at 10.0 μM concentration (similar results are obtained for all other concentrations tested). The decrease in fluorescence intensity over time indicates that fluorescent nanoparticle tags are being released from the satellite assemblies, as compared to the negative control case discussed in Figure 7.2.2. Here, the histogram is presented with a higher aspect ratio to clarify the changes in fluorescence intensity over time; vertical lines correspond to the mean value for each individual case, further clarifying the decrease over time (this is performed to remove some of the effect the peak broadening has as the number of counts decreases.)

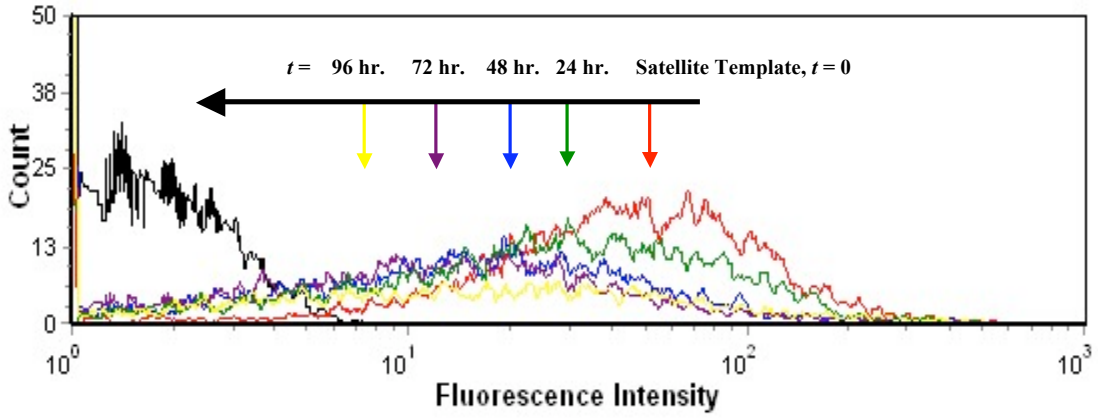

Figure 7.2.4 – Representative fluorescence histogram illustrating the decrease in fluorescence intensity associated with fluorescent particle release from colloidal satellites assemblies following incubation with **B14** secondary targets at 10.0 μM concentration. The large horizontal arrow points in the direction of *increasing* incubation time. Vertical arrows correspond with the mean of the fluorescence intensity at each time point.

This data is then converted to the fraction of nanoparticles released as a function of time following incubation with varying concentrations of **B14** secondary targets in Figure 7.2.5. It is clear that the time-scale of competitive target displacement for immobilized targets is significantly longer than that for soluble targets. Even for the 10 μM case, 72 hours are required to release more than 80% of the nanoparticles. For the lowest concentration of secondary target tested, 10 nM, moderate displacement of 42% is observed at 96 hours. The rate of displacement at this low concentration is fairly linear, however, indicating that given more time, nearly complete release of nanoparticles may occur. The 100 nM **B14** case shows similar behaviour to the 10 nM case overall, though it appears to exhibit a two-state displacement profile, with a great increase in release rate past 48 hours. This behavior may be due to the gradual displacement of multiple linking duplexes between particle surfaces that are slowly displaced by complementary targets initially – if there are still sufficient linkages to remain assembled, a second stage of

competitive hybridization events may be required before release of the nanoparticles finally begins to occur. Once the concentration of secondary targets is increased to 1.0 μM, significant differences in the release profiles become evident, with 57% of the nanoparticles being released within 24 hours. However, the displacement rate greatly decreases for the next 72 hours, maintaining an almost linear state out to 96 hours. The 10.0 μM secondary target case shows similar displacement kinetics as the 1.0 μM case, with a fast initial regime, followed by slower and nearly linear displacement out to 96 hours.

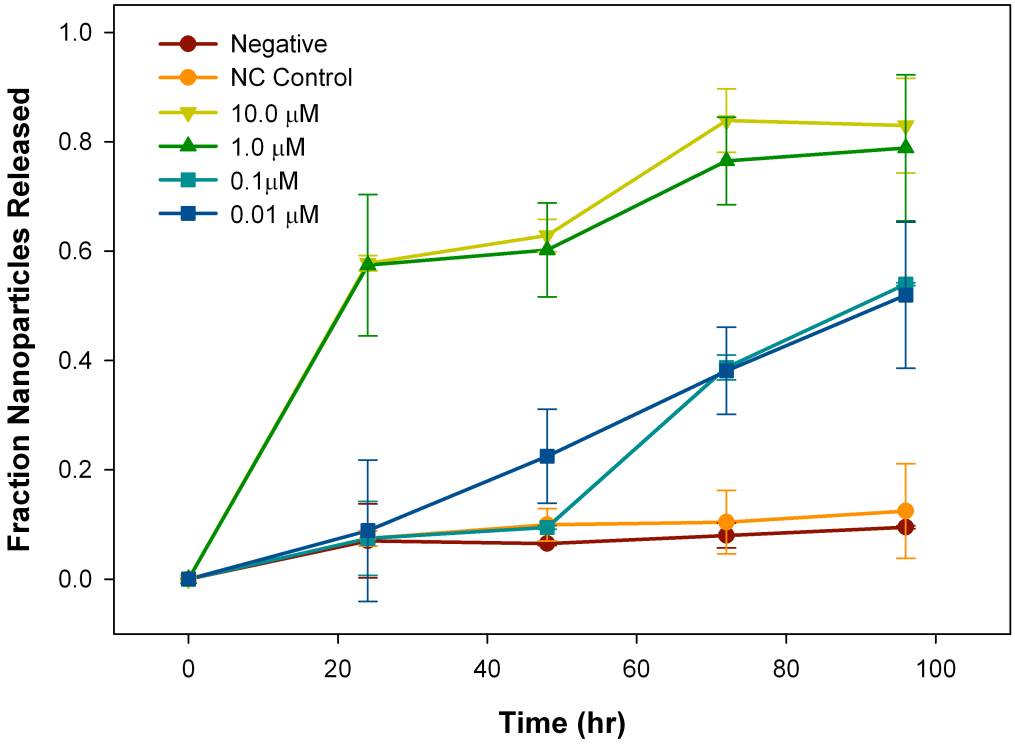

Figure 7.2.5 – Fraction nanoparticles released over time from colloidal satellite assemblies following incubation with **B14** secondary targets at various concentrations. The negative control indicates negative changes to the positive sample run at each time point. The noncomplementary target (NC Control) indicates negligible nanoparticle release following at 10.0 μM.

Though the kinetics of immobilized target displacement are obviously slower than for the soluble target case, the trends in the release profiles for the two highest and two lowest secondary target concentrations highlight concentration dependent behavior as well. We attribute both the decreased overall release rate and the two-state behavior to the presence of multiple linkages between the 5.01 μm and 200 nm shell particle surfaces inducing assembly. With multiple linkages present between particle surfaces (approximately 2-3, as calculated using geometric arguments presented in Chapter 2), it is clear that more linkages must be "broken" by competitive hybridization to cause release of the nanoparticles. Additionally, secondary targets must penetrate deeper into the confined volume to replace the remaining DNA linkages. The successful hybridization of a competitive target with a previously hybridized **A20** probe *does not guarantee* any decrease in fluorescence, as multiple duplexes may exist between surfaces. Our earlier work on restriction enzyme cleavage near the particle surface revealed that steric effects play a significant role in reducing biomacromoleculer activity – these results are confirmed here, as dense local environments between particle surfaces appear to reduce the rate of nanoparticle release compared to the soluble primary target cases in Chapter 6.

7.2.3 – Replacement Rate Analysis of Nanoparticle Release from Satellite Assemblies

In order to compare the release timing of soluble targets (Chapter 6) and nanoparticles, the "half-life" of labeled duplexes or nanoparticle tags is estimated from the data sets. This half-life, $t_{1/2}$, is defined as the time at which half of the soluble primary targets or DNA-linked nanoparticles have been released by competitive hybridization events. As the satellite disassembly studies were only performed for the 14 base-long secondary target, **B14**, we only report half-lives here for the soluble primary target cases

involving **B14** as the competitive target. For both samples, $t_{1/2}$ is not reached at the 10 nM secondary target concentration in the time regime tested. For the soluble case, only 28% of the primary targets have been displaced within 24 hours, while the colloidal satellites show nearly 50% of the nanoparticles released at 96 hours. Once the secondary target concentration is increased to 100 nM, $t_{1/2}$ for the soluble primary target case is determined to be approximately 30 minutes, as 52% of the primary target is displaced in 1,830 seconds. The colloidal satellites case shows a much slower release profile, with $t_{1/2}$ of nearly 96 hours for the 100 nM case. It is evident that when the concentration of secondary targets is sufficient for displacement, it is significantly slower for the nanoparticle case. Upon increasing the secondary target concentration to 1.0 μM, $t_{1/2}$ for the soluble primary targets is just over 60 seconds, with 46% of the primary target displaced within the first minute. The satellite assemblies also see a sharp drop in its half-life time, with over 50% of the nanoparticles released within the first 24 hours. Again, however, it is observed that the rate of release is significantly slower for the satellite assemblies – on the scale of hours, rather than seconds. Finally, the $t_{1/2}$ for the 10.0 μM secondary target concentration is determined. For the soluble case, the half-life is less than 60 seconds, as more than 77% of the primary target are displaced in this time period. As we cannot test less than 1 minute using this technique, we only know that there is greater displacement within the first minute as compared to the 1.0 μM case. For the satellite assemblies, the 10.0 μM secondary target case shows little difference from the 1.0 μM case, with displacement nearly equivalent at 24 hours, and only slightly higher at longer time periods. Again, however, the release timing is significantly slower than for the soluble primary targets. Furthermore, unlike the soluble primary target case, no

increase in the extent of nanoparticle release is observed by increasing the secondary target concentration from 1.0 to 10.0 μM.

7.3 – Conclusions

The results of this section reveal that DNA can act as a programmable and reversible colloidal assembly tool under isothermal conditions by using competitive hybridization as the disassembly trigger. Using a novel approach to flow cytometry, the release of DNA-linked nanoparticles due to competitive hybridization was investigated. Using a previously optimized system in which 10 base-long primary duplexes were successfully displaced by 14 base-long secondary targets, we extended the study to investigate the effect of secondary target concentration on the kinetics of competitive hybridization activity. It was determined that displacement occurs down to 10 nM secondary target, and that a degree of control exists over the replacement rate by changing this concentration. Compared to soluble target displacement (on the order of minutes to hours), the displacement of DNA-linked colloidal satellites is much slower, with replacement times of hours to days. This work is highly relevant for the field of drug delivery, where controlled payload release is of great interest. Further, the flow cytometry procedure developed is an exciting addition to the colloidal scientists characterization toolbox. These results clearly show that DNA holds great promise as a programmable isothermal disassembly tool, specifically for the tuned release of particles from a model DNA-linked drug delivery system.

References

1. Zuker, M. *Nucleic Acids Res.*, **2003**. *31*. 3406-15.

2. Zuker, M. *Mfold Web Server*. **2003**; Accessed 6/01/2008. Available from: http://mfold.bioinfo.rpi.edu/.

3. Rollié, S. and Sundmacher, K. *Langmuir*, **2008**. *24*. 13348-58.

4. Cram, L.S. *Methods in Cell Science*, **2003**. *24*. 1-9.

CHAPTER 8

Extending Competitive Hybridization to Develop Colloidal Drug Carriers with Stealth Coatings

In this chapter, the ability to use competitive hybridization events to induce a stealth-targeting switch is explored in a model carrier – cell mimic system. The premise involves using primary targets conjugated with a PEG polymer "tail" to hybridize to surface-bound **A20** probes on colloidal particles to form a protective or stealth coating. This coating is intended to effectively mask or hide underlying ligand-capped, here, biotinylated DNA. Competitive hybridization is used to release the primary targets, and thereby shed the coating to then reveal the biotin groups to avidin-functionalized colloidal particles. Thus, both primary and secondary hybridization events are employed to first inhibit, and then promote, specific binding events between colloidal particles (model drug carriers) and avidin-functionalized colloidal particles (acting as cellular mimics).

8.1 – Experimental

8.1.1 – Oligonucleotide Selection and Heat Tests

Aminated, biotinylated, PEGylated and fluorescently labeled DNA was purchased from Integrated DNA Technologies and stored as previously described. Table 8.1.1 shows all candidate sequences tested, including several from previous chapters. Following primary hybridization of FITC-tagged targets to **A20**-functionalized colloidal particles, suspensions were washed to remove excess targets and then warmed to 37 °C to

test the effect of heating on a) primary target dissociation in the absence of secondary target strands, and b) primary target release in the presence of secondary targets. To prepare colloidal particles with both DNA probes (**A20**) and biotin-DNA (**T20/Biotin**), mixtures of amine-terminated sequences were coupled to the particle surfaces. This approach closely mimics our approach in Chapter 3 involving mixtures of probe and diluent strands. Fluorescently labeled targets (**B10/FITC** through **B17/FITC**) without PEG tails are first investigated for thermal stability at 37 °C. The primary targets selected from heat tests to be used with a PEG tail are purchased separately from Integrated DNA Technologies as a DNA-PEG conjugate. The PEG tail has a molecular weight of approximately 2700 g/mol. These PEGylated targets are intended to hybridize to the **A20** probes to form the initial PEG coating until displaced or released through competitive hybridization events with secondary targets.

Table 8.1.1 – List of candidate sequences and theoretical duplex melting temperatures *(1)*.

function	sequence	T_m
immobilized probe	**A20** = 5'-NH_3-TTTTTTGGATTGCGGCTGAT-3'	NA
immobilized biotinylated strand	**T20/Biotin** = 5'-NH_3-TTTTTTTTTTTTTTTTTTTT-Biotin-3'	NA
noncomplementary target	**NC14** = 5'- GGATTGCGGCTGAT-3'	NA
soluble 1° targets	**B10** = 3'-ACGCCGACTA-5'	72.0 °C
	B11 = 3'-AACGCCGACTA-5'	72.6 °C
	B12 = 3'-TAACGCCGACTA-5'	72.6 °C
	B13 = 3'-CTAACGCCGACTA-5'	72.8 °C
	B14 = 3'-CCTAACGCCGACTA-5'	75.2 °C
	B15 = 3'-ACCTAACGCCGACTA-5'	76.8 °C
	B16 = 3'-AACCTAACGCCGACTA-5'	76.6 °C
	B17 = 3'-AAACCTAACGCCGACTA-5'	77.2 °C
PEGylated 1° target	**B13/PEG$_{2700}$** = 3'-CTAACGCCGACTA-PEG$_{2700}$-5'	72.8 °C
soluble 2° target	**A'15** = 3'-ACCTAACGCCGACTA-5'	76.8 °C

8.1.2 – Particle Preparation and Adhesion Studies

Nonfluorescent 1.10 μm microspheres (Bang's Labs) were modified with **A20** probes and **T20/Biotin** at various ratios. To control the ratio of biotinylated (ligand-capped strands) to hybridizing **A20** probe strands, the DNA is mixed in specific ratios prior to coupling. Following simultaneous DNA conjugation and then hybridization (with either PEGylated or non-PEGylated targets), all particles are resuspended in 100 μL of PBS/Tween buffer for storage as a 0.01 volume fraction suspension. Avidin-coated, 10.0 μm particles are purchased (Bangs Labs) and used as cell mimics for biotinylated adhesion studies. For adhesion studies, an excess of the DNA-functionalized particles are first incubated with PEGylated targets and washed three times. The "coated" particles are then incubated with the avidin-coated colloidal particles at controlled volume fractions similar to those described for forming colloidal satellite assemblies in Chapter 7. These adhesion studies are done either 1) in the absence of secondary targets (to test for nonspecific adhesion between PEG-coated colloidal particles and avidin-functionalized colloidal particles and 2) in the presence of secondary targets (to test if competitive hybridization effectively "shed" the PEG-coating). Select adhesion studies were also done in the absence of primary and secondary targets to determine the minimum percentage of **T20/Biotin** necessary to drive specific adhesion to cell mimics.

8.1.3 – Flow Cytometry to Quantify Hybridization Activity

Flow cytometry is used to characterize the surface coverage of **A20** probes at various ratios with **T20/Biotin** strands. **B14/FITC** targets are hybridized to the **A20** probes and tagged **A20:B14** duplexes are quantified using flow cytometry as previously discussed. Similar, to quantify the density of PEGylated targets hybridized to the particle

surface, FITC-labeled PEG strands are used. Quantum MESF bead-based standards are again used to convert fluorescence intensity values to the surface density of hybridized targets.

8.1.4 – PEG Shielding Effect and Shedding by Competition

PEGylated target strands **B13/PEG$_{2700}$** (with a PEG molecular weight of 2700 g/mol) are hybridized to **A20** probes in the presence of the minimum concentration of **T20/Biotin** required for subsequent adhesion events to avidin-coated colloidal particles. Following hybridization to form the PEGylated coating, an excess of the 1.10 μm particles comprised of **A20:B14/PEG$_{2700}$** duplexes are then incubated with a suspension of avidin-coated 10.0 μm particles at 0.05%. Confocal microscopy is used to monitor the suspension behavior and check for (nonspecific) adhesion between heterogeneous colloidal particles. Unlabeled secondary targets are then introduced to the suspension and incubated for 24 hours. The suspensions are then studied again using confocal microscopy to determine if specific adhesion now occurs between heterogeneous colloidal particles.

8.2 – Quantification of Target Hybridization Activity and Adhesion Events

8.2.1 – Sheddable Coatings for Drug Delivery Technologies

The use of sheddable coatings in drug delivery technologies is an emerging but exciting field *(2)*. In past studies, the shedding of the coating (typically polymer-based) is driven by some stimulus such as cleavage by matrix metalloproteases (MMPs) *(3)* or pH changes *(4)*. The use of polyethylene glycol or PEG to shield immobilized biotin from

avidin has been previously studied as well *(5)*. In that study, however, there was no stimulus for releasing the polymer chains from colloidal carriers. Competitive hybridization has not been investigated as a "trigger" for inducing a stealth-to-targeting switch in colloidal carriers. Figure 8.2.1 shows a schematic illustration of how competitive hybridization events may be directed to cause programmed shedding of the PEGylated protective coating. This method offers several advantages over previously researched techniques including a level of kinetic control over the shield release (as discussed in Chapter 6). However, because competitive hybridization will now occur *in vivo*, the effect of physiological temperature (37.5 °C) on primary target dissociation and competitive hybridization must first be explored.

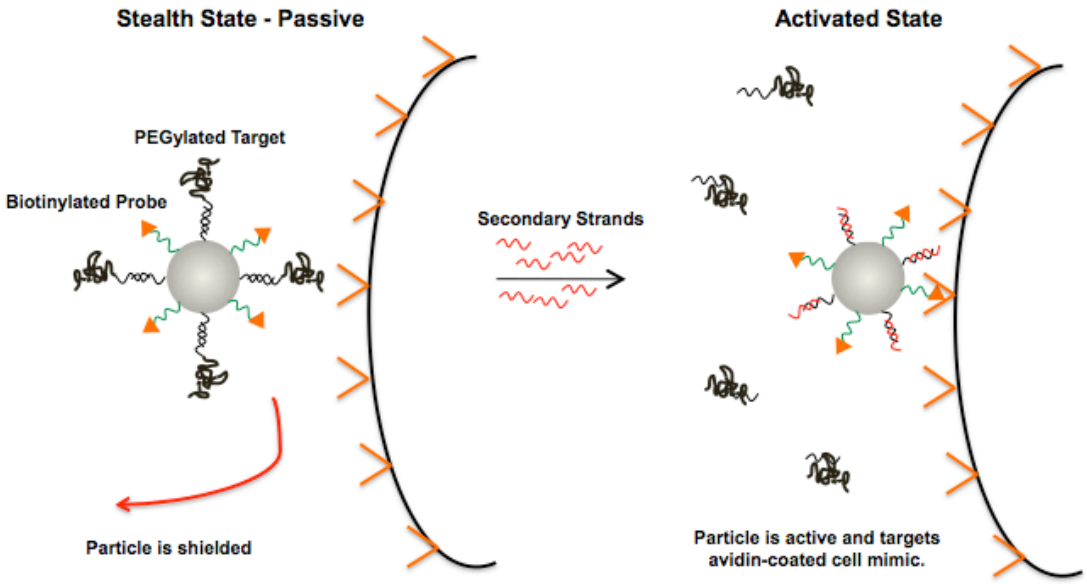

Figure 8.2.1 – Schematic of model carrier undergoing stealth-to-targeting switch (Left). The carrier is initially hindered from adhering to cell mimic (avidin-functionalized colloidal particle) by its coating of PEGylated targets hybridized to immobilized probes. Following competitive hybridization events with longer secondary target strands, these PEGylated targets are released, revealing the underlying biotinylated groups and promoting specific adhesion to avidin-functionalized colloidal particles (Right).

8.2.2 – Effect of Heat on Primary Duplex Stability

A20-immobilized 1.10 μm particles are hybridized to FITC-labeled primary targets of varying base length. First, targets are incubated with the DNA-functionalized colloidal particles for 24 hours and then washed three times to remove excess primary targets. The second step is then to incubate an aliquot of this suspension in a hybridization oven at 37 °C for 24 hours; it is then washed three times. Flow cytometry is performed on both positive (unheated) and heated samples. The number of primary targets dissociated by heat treatment is then measured by comparing the data between the positive control and each heated sample. Figure 8.2.2 shows the effect of heating on

primary targets duplex densities ranging in hybridizing base-length from 10 to 17. First, it is important to notice the general increase in surface duplex density as the primary target length increases, plateauing at approximately 25,000 oligos/μm^2 for the 14 through 17 base-long targets. These surface densities are slightly higher than observed in previous chapters, but they correlate well with parking area changes on the new lot of 1.1 μm particles used for these particular studies.

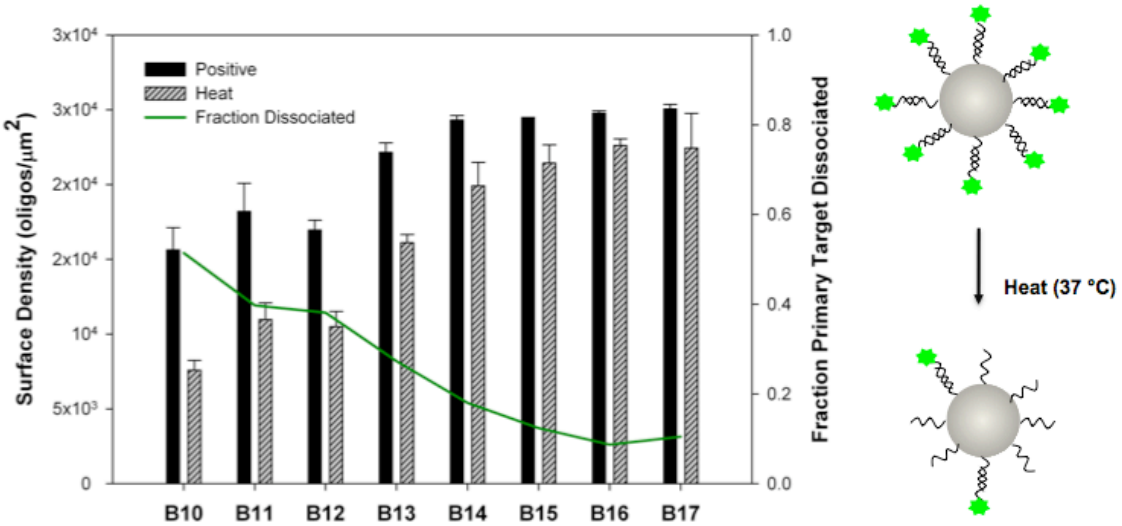

Figure 8.2.2 – Primary duplex densities before (Positive) and after heating suspensions to 37 °C for 24 hours as a function of target base length (10-17). For clarity (since the duplex densities vary with target length), the line traces the fraction of target that is thermally dissociated. Schematic illustrates dissociation of fluorescently labeled primary targets due to heating at 37 °C.

It is particularly noted that the **B10** primary target used in previous chapters under room temperature conditions to drive DNA-mediated particle aggregation, undergoes approximately 50% thermal dissociation. As the primary target length is increased, the

fraction dissociated decreases to approximately 10% for the **B15**, **B16**, and **B17** cases. Interestingly, the fraction primary target dissociated continues to decrease for primary targets longer than 14 bases, though the initial primary duplex density reaches a plateau value for targets 14 to 17 bases in length. This behavior indicates that longer targets either encounter steric interference issues that prevent them from reaching within the polymer brush layer to hybridize to their complementary segments, or the probes functionalized to the surface are saturated at approximately 25,000 oligos/μm^2. Regardless, the decrease in thermal dissociation as targets become longer is evidence of the continuous increase in affinities, as also indicated by the continuous rise in duplex melting temperatures with base length shown in Table 8.1.1.

8.2.3 – Effect of Heat on Competitive Hybridization Events

Based on the above results, two primary targets were chosen for further investigation of competitive hybridization at physiological conditions – the **B11** and **B13** cases. For both of these targets moderate hybridization occurs, but dissociation is less pronounced than observed for the **B10** targets. In addition, **B15** is selected as the secondary target of interest for two reasons; first, 15 base-long targets achieved maximum duplex density of approximately 25,000 oligos/μm^2. Second, these targets showed minimal thermal dissociation (approximately 10%). Figure 8.2.3 shows the results of incubating particles functionalized with labeled **A20:B11** or **A20:B13** primary duplexes with unlabeled secondary target **B15** both at room temperature and at 37 °C. The **B11** primary target case shows moderate primary target hybridization of approximately 18,000 oligos/μm^2. After 24 hours of *heating only,* nearly 50% of these primary targets are dissociated. Following the addition of secondary **B15** targets at room

temperature, only approximately 25% of the original duplexes remain Finally, when incubated with secondary targets at 37 °C, only about 1% of the original **A20:B11** duplexes remain. This data reveals that competitive hybridization is significantly more efficient at elevated temperatures, and that the **B11** target can be completely displaced from the surface. In order to decrease the fraction of primary targets thermally dissociated by heating at 37 °C, however, **B13** primary targets were investigated as a potential alternative system. Figure 8.2.3 shows these results, with an initial primary duplex density of approximately 21,000 oligos/μm^2 for the **B13** case. It is observed that after heating, only 25% of the primary targets are dissociated within 24 hours, indicating that significantly fewer primary targets are lost at physiological temperature as compared to the **B11** primary target case. Further, competitive hybridization with secondary target **B15** at room temperature shows minimal competitive displacement; only 25% of the primary targets are displaced. However, when competitive hybridization is performed at 37 °C, only about 1% of the original **A20:B13** duplexes remain. Again, this result shows the increased efficiency of competitive hybridization at higher temperatures, and indicates that higher affinity primary targets can be displaced than observed at room temperature. As we desire a primary target with enhanced thermal stability (in the absence of competitive secondary targets) but can be effectively displaced by competitive hybridization, the **B13** primary target is chosen as the primary target for forming the "hybridized" PEG-DNA-based coating for subsequent adhesion studies.

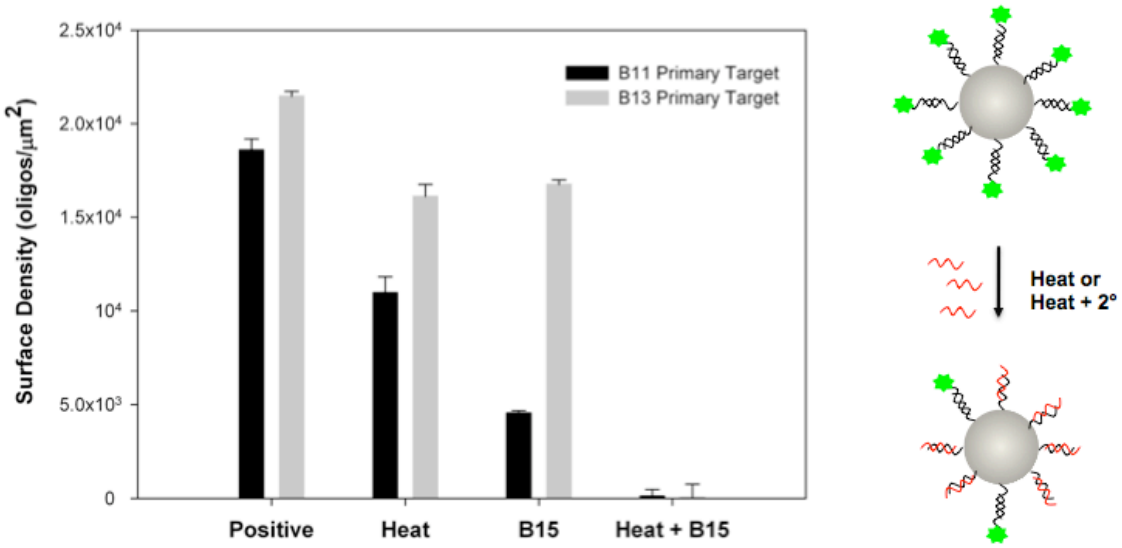

Figure 8.2.3 – Surface density of **A20:B11** and **A20:B13** primary duplexes under varying conditions. The conditions are as follows: initial duplex density at room temperature (Positive); following heating at 37 °C for 24 hours (Heat); following incubation with **B15** secondary target at room temperature (B15), and at 37 °C (Heat + **B15**). Schematic illustrates dissociation or displacement of fluorescently labeled primary targets by heat or competitive hybridization, respectively.

8.2.4 Determination of Minimum Biotin Required for Adhesion to Avidin-Functionalized Colloidal Particles

In order to target avidin-coated microspheres that act as cell mimics, biotinylated probes are immobilized to 1.10 μm polystyrene microspheres. However, as initial "stealth" behavior of the colloidal carriers is desired, the minimum concentration of biotinylated probes required for subsequent targeted adhesion is first determined. Mixtures of biotinylated **T20** and **A20** probes are coupled to colloidal particles at varying ratios. To determine the "effective" density of **A20** probes following immobilization, suspensions are incubated with FITC-labeled **B14** primary targets. Controls are first run to test for non-specific binding of the **B14** targets on surfaces that only possess the

T20/Biotin strands. Results showed negligible nonspecific binding of the targets. Figure 8.2.4 shows the results of primary target hybridization on surfaces functionalized with mixtures of **T20/Biotin** and **A20**, with the initial (i.e., prior to immobilization) fraction of **A20** probes plotted along the x-axis. In addition, fluorescently labeled soluble avidin (Molecular Probes) was used quantify the **T20/Biotin** present on the surface. First, it appears that the avidin-FITC does serve as a suitable receptor for the **T20/Biotin** strands, though its maximum density does not equal that of the **A20:B14** duplexes, nor does it mimic the relatively nonlinear profile. The relatively low avidin-FITC binding may be due to 1) individual avidin molecules are binding to multiple, closely spaced biotin molecules on the surface and 2) the large avidin molecule is shielding neighboring biotin groups from binding to other avidin proteins.

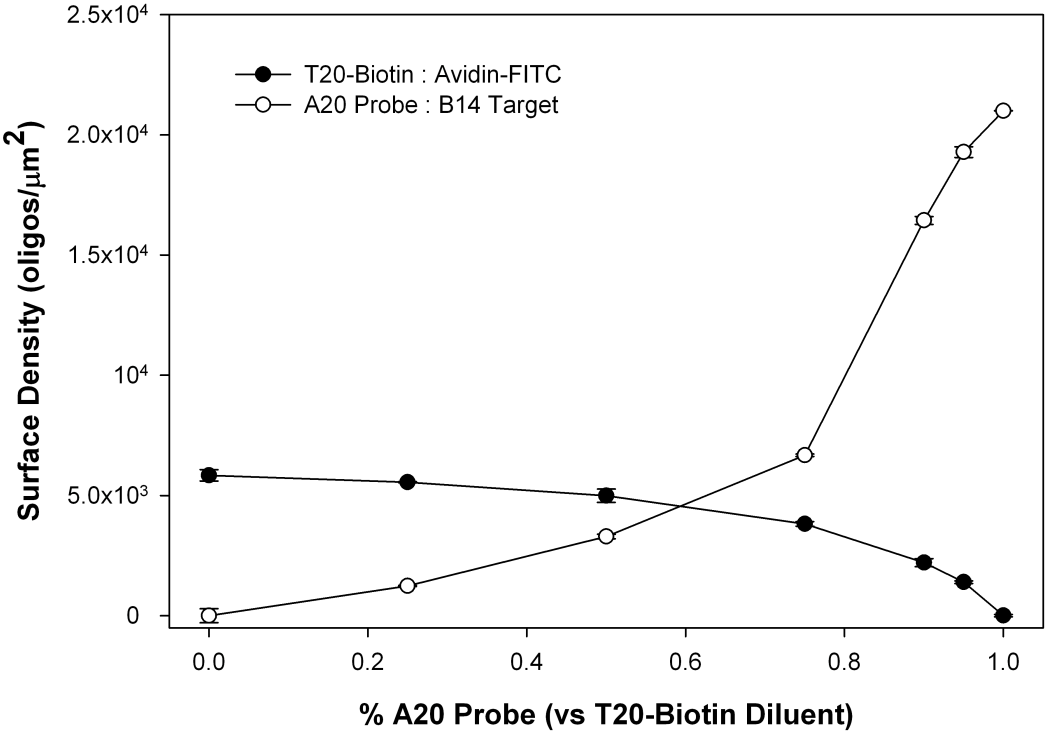

Figure 8.2.4 – Surface density of 1) **B14** primary targets hybridized to **A20** probes and 2) soluble avidin-FITC bound to biotinylated **T20** strand.

After flow cytometry experiments revealed that surfaces could be titrated with the biotinylated probes and that the biotin functionality did not affect soluble target hybridization, assembly experiments were performed to determine the minimum ratio of **A20:T20/Biotin** was required to promote successful biotin-avidin mediated adhesion. Briefly, **A20-T20/Biotin**-functionalized 1.10 μm particles were mixed with avidin-functionalized 10.0 μm particles at 37 °C and mixtures were observed under microscopy after 24 hours. Figure 8.2.4 shows representative micrographs of these initial adhesion studies. The control, 0% **T20/Biotin** (a), and the 2.5% **T20/Biotin** case (b) show negligible particle adhesion after 24 hours, indicating that the critical amount of biotin to promote specific adhesion has not been reached. Upon increasing the **T20/Biotin** loading

to 5% (c) it is observed that avidin-functionalized microspheres are coated with the smaller, colloidal particles while all higher loadings also promoted adhesion between heterogeneous particles (d, e). 5% **T20/Biotin** was selected as the optimal case since approximately 95% of the remaining strands can serve as hybridizing probes to form the PEG-coating with **B13/PEG$_{2700}$** targets.

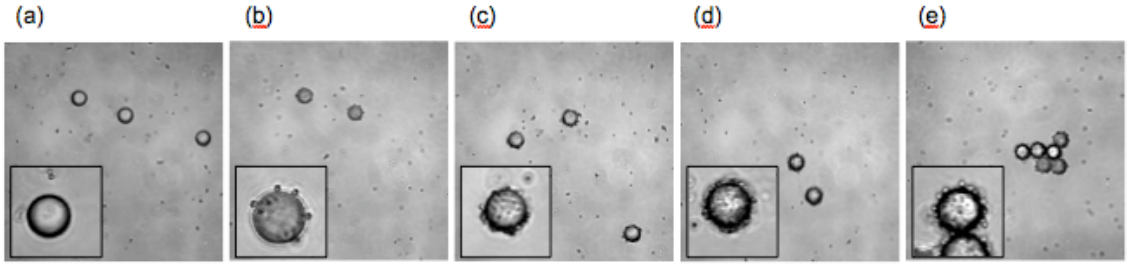

Figure 8.2.5 – Representative confocal micrographs of adhesion studies between large avidin-functionalized microspheres and smaller colloidal particles functionalized with varying ratios of **A20** and **T20/Biotin**. The percentage of **T20/Biotin** loadings is as follows: (a) 0%, (b) 2.5%, (c) 5.0%, (d) 50%, and (e) 100%. The control, 0% **T20/Biotin**, (a) shows negligible particle adhesion after 24 hours.

8.2.5 – PEGylated Target Hybridization and Quantification

To quantify the hybridization activity of PEGylated **B13** targets on 1.10 μm particle surfaces, fluorescently labeled **B13/PEG$_{2700}$** is used. Briefly, 0% **T20/Biotin** (100% **A20**) and 5% **T20/Biotin** (95% **A20**) immobilized particles are incubated with 100 μL at 10 μM of the **B13/PEG$_{2700}$/FITC** targets for 24 hours at room temperature. After primary hybridization the sample is split into three samples to determine the effect of heat and competitive hybridization on the PEGylated target case. Flow cytometry is

then performed to determine the surface density of hybridized targets both before and after heating or competitive hybridization.

Figure 8.2.6 shows the surface density of FITC-labeled **B13/PEG$_{2700}$** targets for the 0% and 5% **T20/Biotin** cases. It is observed that significant hybridization activity does occur with a hybridized surface density of approximately 11,000 oligos/μm^2 for the 100% **A20** probe case. This surface density indicates that the presence of the PEG tail does not completely prevent hybridization by shielding **B13** access to the **A20** probe. However, the surface density is severely reduced (by nearly 50%) as compared to the **B13** case with no PEGylation (Figure 8.2.2). After the suspension is heated for 24 hours, the surface density of targets drops 52% to 5,400 oligos/μm^2. Interestingly, this drop is significantly higher than that seen due to heating for the non-PEGylated **B13** target. Finally, competitive hybridization with the selected secondary target, **B15**, shows 99% displacement of the PEGylated primary target after 24 hours of secondary hybridization at 37 °C. Further, a control sample with a noncomplementary secondary target shows no competitive displacement occurs. The 5% **T20/Biotin** case behaves nearly identical to the 0% case discussed above. Collectively, this indicates that programmable release of the PEGylated targets occurs at 37 °C, and thus may allow directed shedding of the PEG coating to reveal underlying ligands acting as a sheddable shield layer.

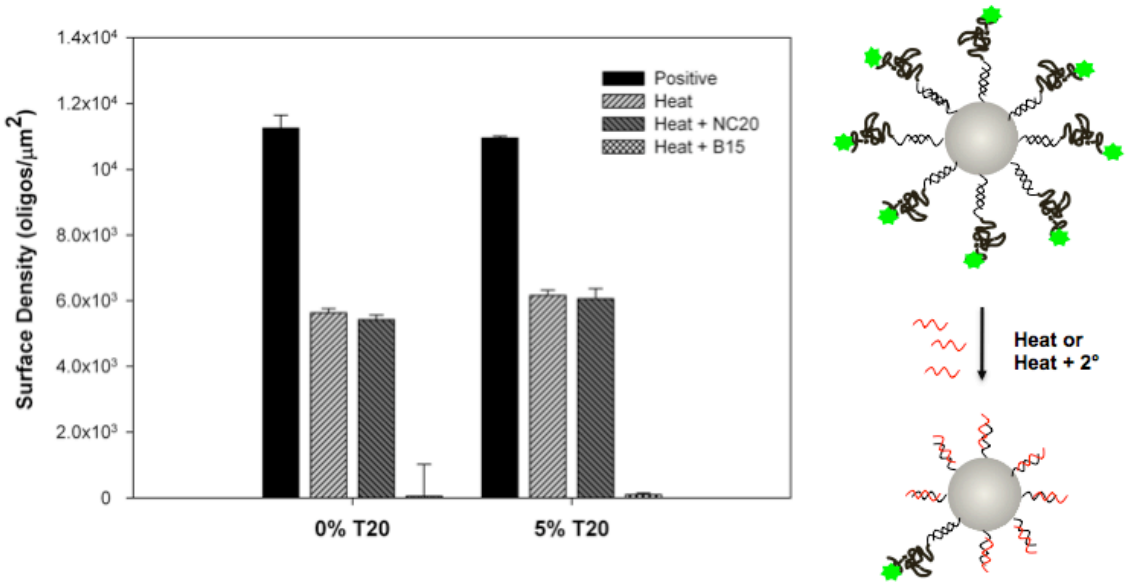

Figure 8.2.6 – Surface density of **B13/FITC** primary targets following target hybridization (Positive), 24 hours of heating at 37 °C (Heat), 24 hours of heating with the addition of a non-complementary secondary target (Heat + NC20) and after 24 hours of heating with the secondary target **B15** (Heat + B15) for samples with 0% **T20/Biotin** (100% **A20** probes) and 5% **T20/Biotin** (95% **A20**). Schematic illustrates dissociation or displacement of fluorescently labeled, PEGylated **B13** primary targets by heating or competitive hybridization, respectively.

8.3 – Programmed Adhesion Between Biotinylated and Avidin-Functionalized Particle Surfaces

8.3.1 – Shielding of Biotinylated Particles from Avidin Mimic by PEGylated Targets

Following hybridization of the 95% **A20** (5% **T20/Biotin)** particles with the **B13/PEG$_{2700}$** target, assembly tests are performed to determine if the PEGylated target layer provides sufficient shielding to prevent adhesion between heterogeneous colloidal particles. Briefly, **B13/PEG$_{2700}$** targets are hybridized to the 5% **T20/Biotin** case as previously described in 8.2.5. Following target hybridization, samples are resuspended to

0.1% and introduced into suspension with avidin-functionalized 10.0 µm particles. The samples are incubated for 24 hours at 37 °C and then imaged using confocal microscopy. Figure 8.3.1 shows the results of the shielding experiment for the 5% **T20/Biotin** case. The adhesion control in 8.3.1 (a) shows complete adhesion at 37 °C when no PEGylated target is present. However, 8.3.1 (b) shows that negligible adhesion is observed when the shielding target is present, indicating that the PEG_{2700} tail successfully blocks the binding of the biotinylated group on the 1.10 µm colloidal particles to the avidin-coated 10.0 µm colloidal particles. Interestingly, this shielding occurs even though as much as 50% of the PEGylated targets may be thermally dissociated.

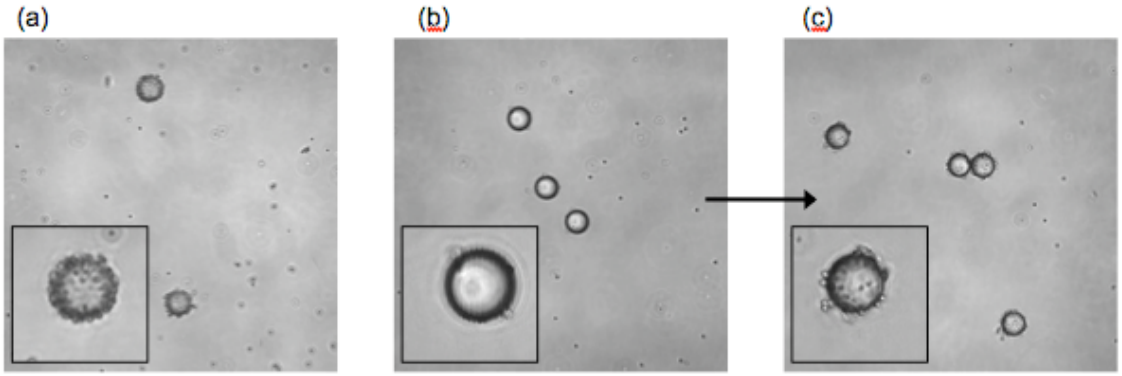

Figure 8.3.1 – Representative confocal micrographs indicating (a) adhesion of 5% **T20/Biotin** colloidal particles to avidin-functionalized 10.0 µm microspheres in the absence of PEGylated targets. Samples that are first hybridized to **B13/PEG$_{2700}$** show little or no adhesion when introduced to the same avidin-coated microspheres (b). Following competitive hybridization (indicated by the arrow) with a **B15** secondary target adhesion now occurs in (c). All suspensions were incubated at 37 °C.

8.3.2 – Competitive Hybridization for Sheddable Coatings

Following confirmation of particle shielding due to the PEGylated target, a 5.0 μm solution of **B15** secondary target was introduced to the suspension. The sample was incubated at 37 °C for 24 hours and then reimaged to determine the effect of competitive hybridization. Figure 8.3.1 (c) shows a representative sample following 24 hours of competitive hybridization. It is evident that adhesion occurs, indicating that sufficient release of PEGylated target has occurred to reveal the underlying biotin functionalities. Further, introduction of a noncomplementary secondary target resulted in no change to adhesion between colloidal particles – indicating that secondary target hybridization does drive the PEG target release permitting biotinylated probes to bind to avidin-functionalized microspheres. It is important to note that all experiments are performed and held at 37 °C – the transitions observed are in no way due to possible swelling of the polystyrene particles as temperatures are raised.

8.4 – Conclusions

Sheddable coatings are of tremendous interest in the drug delivery field. Here, the competitive hybridization technique detailed in this thesis is used for programmed release of a PEGylated targets from the surface of 1.10 μm particles immobilized with biotin-capped macromolecules. First, heating tests are performed to determine the effect of physiological temperature on simple target dissociation. A system of primary and secondary targets is determined to optimize modest primary target hybridization with increased stability against heating. The critical concentration of **T20/Biotin** probes

required for adhesion to avidin-coated microspheres is then determined via confocal microscopy and the quantity of **T20** and **A20** probes on the surface is quantified via flow cytometry. The ability of PEGylated targets to hybridize to **A20** probes in the presence of the biotinylated diluent strands is then determined. Finally, adhesion tests are performed to determine the ability of PEGylated targets to shield the biotin functionality and prevent particle adhesion. It is shown that optimizing the system as described herein permits the creation of a sheddable coating that prevents particle adhesion but that can be removed by competitive hybridization. This research presents an important first step in the development of a stealth drug delivery vehicle in which stealth coatings can be removed via programmable competitive hybridization.

References

1. Zuker, M. *Mfold Web Server*. **2003**; Accessed 01/14/2009. Available from: http://mfold.bioinfo.rpi.edu/.

2. Romberg, B., W. Hennink, and G. Storm. *Pharm. Res.*, **2008**. *25*. 55-71.

3. Harris, T.J., G. von Maltzahn, M.E. Lord, J.H. Park, A. Agrawal, D.H. Min, M.J. Sailor, and S.N. Bhatia. *Small*, **2008**. *4*. 1307-12.

4. Sawant, R.M., J.P. Hurley, S. Salmaso, A. Kale, E. Tolcheva, T.S. Levchenko, and V.P. Torchilin. *Bioconjug. Chem.*, **2006**. *17*. 943-9.

5. Kaasgaard, T., O.G. Mouritsen, and K. Jorgensen. *Int. J. Pharm.*, **2001**. *214*. 63-5.

CHAPTER 9

Summary and Concluding Remarks

This thesis detailed the use of competitive hybridization reactions to cause isothermal redispersion of DNA-linked colloidal structures. Previously, multiple groups have relied on DNA-hybridization to program the assembly of a variety of colloid-based systems – relying on the complementary base pairing of DNA to dictate whether aggregation or assembly occurs. Here, we introduce a new concept whereby affinity differences between primary and secondary targets are used to program the redispersion of DNA-linked structures. We have found that by optimizing the base-pair difference (affinity) and duplex number (avidity), competitive hybridization can be used to program both the extent and rate of colloidal disassembly. In the process, a novel restriction enzyme procedure was developed that allows of modification of surface-immobilized strands at closer proximities to particle surfaces than has previously been observed. We determined the effect that various diluent strands had on DNA-mediated colloidal aggregation, and found that regardless of the diluent strand length (and its effects on the steric environment near the surface) a minimum of three to five duplexes is required between particle surfaces to induce aggregation. The kinetics of competitive hybridization was investigated, and replacement rate constants were derived for the soluble target displacement case. Though multiple studies have analyzed displacement of targets at a planar surface, no previous work has revealed the kinetics of oligonucleotide displacement on a bead-based system – this work holds tremendous impact in the field of

bead-based microarrays. Soluble target displacement revealed that observed replacement rates could be tuned over the range of 10^{-6} to 10^{-2} s^{-1}. To investigate the programmed disassembly of DNA-linked satellite structures, a novel flow cytometry technique was developed that allows one to analyze the release of satellite nanoparticles from a template particle. Not only did this technique reveal the kinetic behavior of our model drug delivery system, it also introduces a new way for colloidal scientists to analyze aggregate structures using a technique traditionally reserved for biologists. Finally, the competitive hybridization reaction optimized and analyzed in the first seven chapters was adopted to develop a proof-of-concept stealth drug delivery vehicle. It was successfully shown that secondary targets could displace PEGylated primary targets for use in shedding a protective coating. This work has tremendous promise for drug delivery applications in which programmed release of a protective coating may offer a stealth targeting mechanism.

Combined, this thesis work revealed that competitive hybridization could be used to program the isothermal redispersion of DNA-linked colloidal structures, which helps expand DNA's usage as a reversible assembly tool into physiological environments. Significant work remains in this field, but this thesis continues adding various techniques to the "toolbox" of DNA-mediated assembly. Current work in the lab is now investigating the use of competitive hybridization for mismatch and pathogen detection. Further, both ribonucleic acids (RNA) and locked nucleic acids (LNA) are being investigated for their ability to undergo competitive hybridization reactions. Several technologies are also being investigated for the protection of DNA duplexes from enzymatic cleavage *in vivo*. Though hurdles remain, DNA is a powerful and exciting tool

for the materials science field, and remains the quintessential tool for programmable materials synthesis.

APPENDIX A

NEAREST-NEIGHBOR THERMODYNAMIC ANALYSIS

Utilizing the nearest-neighbor thermodynamic calculations of SantaLucia et al. (31), we determined the Gibbs free energy of duplex formation for the **B10** primary target case (forming a 10 base-long duplex with **A20**). The calculation is based upon a summation of nearest neighbor interactions. The figure below shows how these interactions are determined and summed for each nearest neighbor present. The initiation value for AT is -5.0 kcal, while the symmetry value (for this case with no self-complementarity) is zero. Similar calculations could be performed for all targets and concentrations to determine interactions energies for each system.

$$\Delta G^{\circ}(total) = \Sigma n_i \Delta G_i(i) + \Delta G^{\circ}_{initG-C} + \Delta G^{\circ}_{initA-T} + \Delta G^{\circ}_{sym}$$

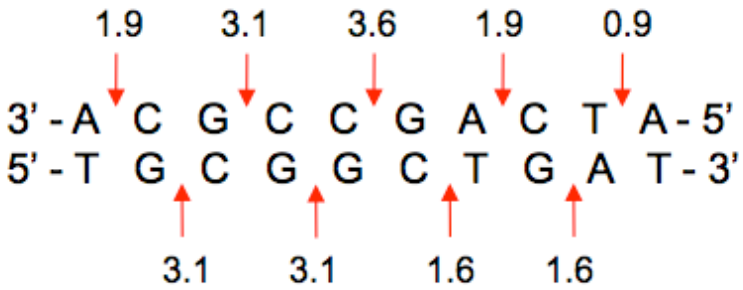

$$\Delta G(total) = 2(1.9) + 3(3.1) + 1(3.6) + 2(1.6) + 1(0.9) - 5.0$$

$$\Delta G(total) = 15.8(kcal/mol)$$

We next use this free energy value in order to approximate the interaction energy associated with **B10** duplexes between particle surfaces, shown below. For these

calculations, the free energy for the **B10** duplex is reported as 15.8 kcal/mol and room temperature is used to calculate $1k_BT$ = 4.11 x 10^{-21} Joules. We report the interaction energy as k_BT per duplex:

$$\frac{1\ duplex}{6.02\times10^{23}}\times\frac{15.8\ kcal}{mol}\times\frac{4184\ J}{kcal}=5.49\times10^{-19}\ J$$

$$\frac{5.49\times10^{-19}\ J}{4.11\times10^{-21}\left(\frac{J}{k_BT}\right)}=26.718\ \frac{k_BT}{duplex}$$

It is important to recognize that this calculated interaction energy of 26.718 *kT* per duplex is likely overestimated. First, the information used to derive the free energy is available only for duplexes *in solution* – it is beyond the scope of this study to determine these free energies once immobilized to the particle surface. Second, this interaction energy does not take into effect any vdW attractions or, more importantly, electrostatic or electrosteric repulsions. As the colloids are stable within suspension (in the absence of immobilized DNA) and coated with negatively charged carboxyl groups, it is likely the electrostatic repulsion is high.

APPENDIX B

POLYSTYRENE MICROSPHERE CHARACTERIZATION AND SPECIFICATIONS

Table B.1: Characteristics of microsphere populations used in experimental studies. All properties are reported by manufacturer (also shown). Characterization techniques used for size analysis are also shown.

Microsphere Population	Supplier	Diameter (μm)	Parking Area ($Å^2$/surface group)	Solids Content (wt. %)	Characterization Technique (by supplier)
1.04 μm nonfluorescent	Bangs Labs	1.04 μm ± 0.045	9.0	10.1%	DLS
5.01 μm nonfluorescent	Bangs Labs	5.01 μm ± 0.105	44.5	10.4%	Coulter
1.10 μm nonfluorescent	Bangs Labs	1.10 μm ± 0025	6.2	10.5%	DLS
1.1 μm red fluorescent	Molecular Probes	1.1 ± 0.035 μm	7.5	2%	DLS
0.21 μm red fluorescent	Molecular Probes	0.21 ± 0.005 μm	NA	2%	DLS
9.95 μm Avidin-coated, nonfluorescent	Bangs Labs	9.95 μm	NA	1%	Coulter

All microsphere population size and parking area calculations were performed by supplier using either light scattering (DLS) or coulter counting. Flow cytometry is also performed by both supplier and in-lab to determine that the percent singlets in suspension exceeds 95% upon arrival. If further characterization of microsphere populations is desired, a variety of techniques may be applicable, including:

1. Zeta potential measurements to determine surface charge density before and after DNA immobilization.

2. Scanning electron microscopy after critical point drying to investigate size distribution and surface roughness of particles. However, this technique may cause de-swelling of the polystyrene particles and should be approached with caution. A reference SEM image is shown in Figure B.1.
3. In-house dynamic light scattering (DLS) to confirm size distribution quoted by supplier.

The surface roughness of the polystyrene may also be of interest, as the length scale of oligonucleotides used in these experiments is likely on the size-range of the surface roughness. Characterization of the roughness within an aqueous environment is not attempted. Since we see hybridization and assembly behavior occurring with great specificity, the roughness obviously does not preempt the specific reactions that must occur.

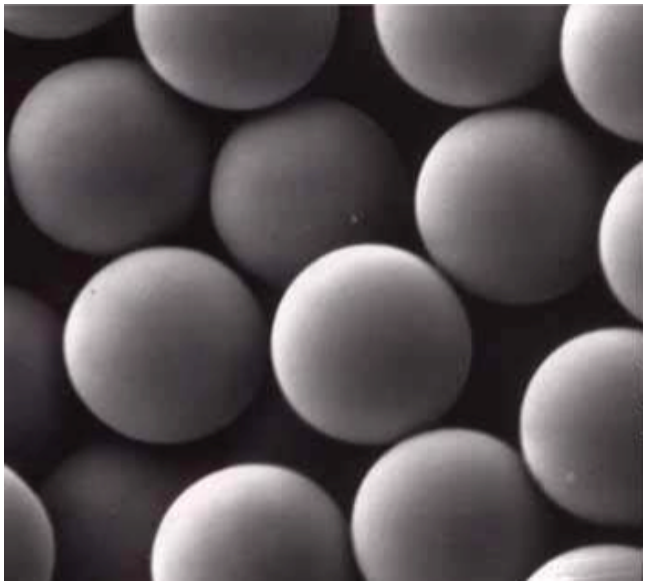

Figure B.1: SEM image of 1.10 μm polystyrene microspheres provided by Bangs Laboratories.

APPENDIX C

PHASE TRANSITION ANALYSIS

In addition to qualitative analysis to determine the phase transition points, ***C**** and ***C*****, image processing was performed. After converting individual micrographs to 8-bit black and white images, the mean grey intensity (MGI) for each sample was determined using ImageJ software. The MGI for each sample was plotted as a fraction of **A20** target for the **T20** diluent strand case only. MGI can be used to monitor the aggregation behavior as follows: fluid singlet suspensions appear gray and are recorded with lower MGI values. As the sample aggregates, aggregate structures appear dark or black, resulting in higher MGI values.

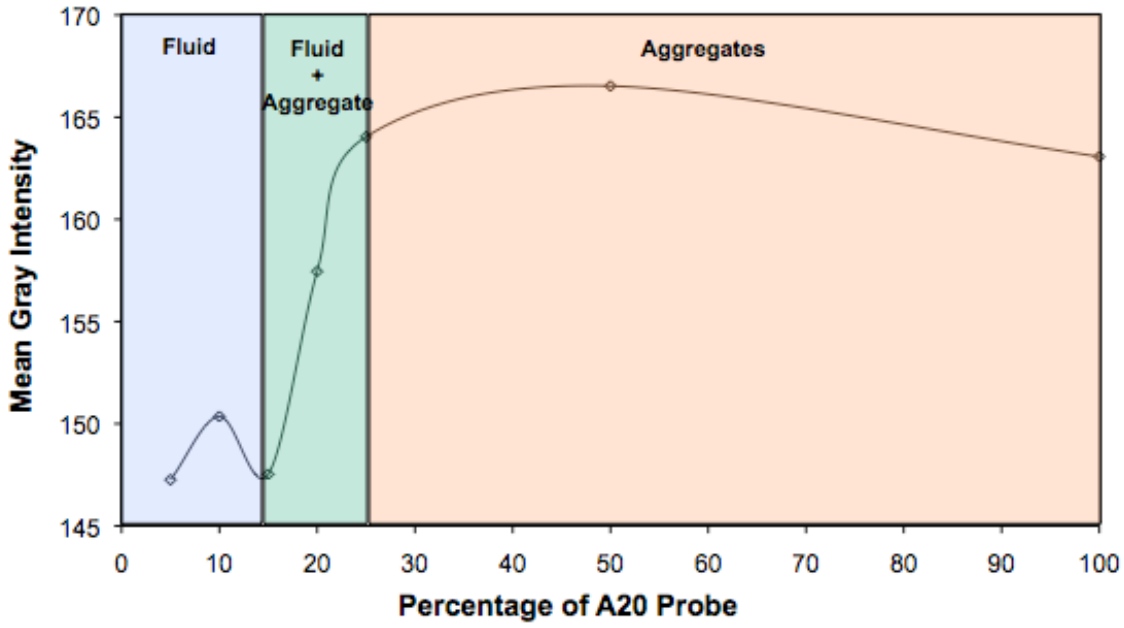

Figure C.1: Mean gray intensity plotted against fraction of **A20** probe. Increasing MGI reveals aggregation of singlet particles.

In addition to mean gray intensity analysis, dynamic light scattering (DLS) could also be performed to obtain quantitative data for the phase transitions. DLS is a technique whereby light scattering can be used to monitor the motion of particles in solution. Based upon information of Brownian motion of the particles, it is possible to derive a size range of the aggregates as they form. Either technique (MGI or DLS) is sufficient if more quantitative data for phase transitions is desired.

APPENDIX D

NUMERICAL DATA FOR KINETICS ANALYSIS

Tables below show average primary target displaced, non-complementary control compensation, and error as standard deviation for four sets of kinetic runs. The samples are run as two sets on each of two batches of probe-immobilized particles. Any negative values (common for the shorter sequences at low concentration) exist due to the compensation with noncomplementary sequences. In these cases, the behavior of the secondary target and the control are essentially the same, and small changes in the fluorescence reading result in occasional (and negligible) negative values. In the graphs, the negative values are set to zero.

Table D.1: Kinetic analysis for **B8** secondary target at all concentrations tested.

B8 2° Target Analysis				
10 nM				
Time (sec)	**Fraction 1° Replaced**	**Standard Error**	**Control Replaced**	**Fraction 1° Displaced by Competition**
0	0	0	0	0
60	0.07	0.054761201	0.121727414	-0.051727414
420	0.07	0.043417437	0.078201073	-0.008201073
900	0.09	0.035766313	0.073836053	0.016163947
1800	0.09510131	0.081310109	0.096998338	-0.001897028
2700	0.111079485	0.103906661	0.108248238	0.002831246
3600	0.109501855	0.073508994	0.111338704	-0.001836849
14400	0.097657909	0.100304439	0.050629848	0.047028061
86400	0.031723008	0.044863108	0.088684176	-0.056961169
100 nM				
Time (sec)	**Fraction 1° Replaced**	**Standard Error**	**Control Replaced**	**Fraction 1° Displaced by Competition**
0	0	0	0	0
80	0	0.04003004	0.121727414	-0.121727414
465	0.04066	0.057499884	0.078201073	-0.037541073
900	0.06739	0.033720779	0.073836053	-0.006446053
1830	0.04845	0.068514006	0.096998338	-0.048548338
2710	0.05135	0.058406342	0.108248238	-0.056898238
3600	0.05396	0.060711398	0.111338704	-0.057378704
14400	0	0.05993884	0.050629848	-0.050629848
86400	0.05977	0.010426148	0.088684176	-0.028914176
1 µM				
Time (sec)	**Fraction 1° Replaced**	**Standard Error**	**Control Replaced**	**Fraction 1° Displaced by Competition**
0	0	0	0	0
60	0.038842	0.044258629	0.121727414	-0.082885414
420	0.05701	0.06689573	0.078201073	-0.021191073
900	0.038813	0.030469026	0.073836053	-0.035023053
1800	0.088093	0.089474436	0.096998338	-0.008905338
2700	0.081046	0.053578562	0.108248238	-0.027202238
3600	0.057025	0.09443653	0.111338704	-0.054313704
14400	0.044848	0.095583445	0.050629848	-0.005781848
86400	0.14195	0.077313225	0.088684176	0.053265824
10 µM				
Time (sec)	**Fraction 1° Replaced**	**Standard Error**	**Control Replaced**	**Fraction 1° Displaced by Competition**
0	0	0	0	0
60	0.0974	0.119479308	0.121727414	-0.024327414
420	0.10143	0.168708851	0.078201073	0.023228927
900	0.10535	0.175685732	0.073836053	0.031513947
1800	0.11266	0.182475158	0.096998338	0.015661662
2700	0.11729	0.195137593	0.108248238	0.009041762
3600	0.12088	0.2031472	0.111338704	0.009541296
14400	0.11421	0.209368205	0.050629848	0.063580152
86400	0.13008	0.197808847	0.088684176	0.041395824

Table D.2: Kinetic analysis for **B10** secondary target at all concentrations tested.

B10 2° Target Analysis				
10 nM				
Time (sec)	**Fraction 1° Replaced**	**Standard Error**	**Control Replaced**	**Fraction 1° Displaced by Competition**
0	0	0	0	0
60	0.133000181	0.03521055	0.121727414	0.011272767
420	0.175315153	0.095052957	0.078201073	0.09711408
900	0.12043679	0.050623439	0.073836053	0.046600737
1800	0.152439645	0.080561786	0.096998338	0.055441307
2700	0.176733386	0.076666615	0.108248238	0.068485148
3600	0.188680877	0.080828339	0.111338704	0.077342173
14400	0.253820662	0.058713162	0.050629848	0.203190814
216000	0.321506164	0.111692353	0.088684176	0.232821988
100 nM				
Time (sec)	**Fraction 1° Replaced**	**Standard Error**	**Control Replaced**	**Fraction 1° Displaced by Competition**
0	0	0	0	0
80	0.1203	0.023588143	0.121727414	-0.001427414
465	0.12248	0.001234586	0.078201073	0.044278927
900	0.13508	0.008874329	0.073836053	0.061243947
1830	0.14596	0.002706985	0.096998338	0.048961662
2710	0.14664	0.003669291	0.108248238	0.038391762
3600	0.16913	0.00505883	0.111338704	0.057791296
14400	0.14902	0.017035049	0.050629848	0.098390152
86400	0.51549	0.016984032	0.088684176	0.426805824
1 µM				
Time (sec)	**Fraction 1° Replaced**	**Standard Error**	**Control Replaced**	**Fraction 1° Displaced by Competition**
0	0	0	0	0
60	0.11933	0.033291516	0.121727414	-0.002397414
420	0.24749	0.102107331	0.078201073	0.169288927
900	0.15652	0.047579396	0.073836053	0.082683947
1800	0.14177	0.053748739	0.096998338	0.044771662
2700	0.15339	0.038651087	0.108248238	0.045141762
3600	0.14764	0.050786973	0.111338704	0.036301296
14400	0.15788	0.063007653	0.050629848	0.107250152
86400	0.41401	0.042259152	0.088684176	0.325325824
10 µM				
Time (sec)	**Fraction 1° Replaced**	**Standard Error**	**Control Replaced**	**Fraction 1° Displaced by Competition**
0	0	0	0	0
60	0.05054	0.087536225	0.121727414	-0.071187414
420	0.15197	0.104779356	0.078201073	0.073768927
900	0.20021	0.065770245	0.073836053	0.126373947
1800	0.25917	0.084318331	0.096998338	0.162171662
2700	0.32076	0.121686767	0.108248238	0.212511762
3600	0.38522	0.088739758	0.111338704	0.273881296
14400	0.40163	0.048742239	0.050629848	0.351000152
86400	0.49867	0.09398401	0.088684176	0.409985824

Table D.3: Kinetic analysis for **B12** secondary target at all concentrations tested.

B12 2° Target Analysis				
10 nM				
Time (sec)	**Fraction 1° Replaced**	**Standard Error**	**Control Replaced**	**Fraction 1° Displaced by Competition**
0	0	0	0	0
60	0.058575917	0.02797991	0.121727414	-0.063151497
420	0.071440288	0.03328614	0.078201073	-0.006760785
900	0.112722647	0.00631728	0.073836053	0.038886594
1800	0.13599843	0.016988796	0.096998338	0.039000092
2700	0.165961397	0.004996373	0.108248238	0.057713158
3600	0.154168655	0.018066336	0.111338704	0.042829951
14400	0.144686471	0.018703363	0.050629848	0.094056623
86400	0.380964163	0.003622266	0.088684176	0.292279987
100 nM				
Time (sec)	**Fraction 1° Replaced**	**Standard Error**	**Control Replaced**	**Fraction 1° Displaced by Competition**
0	0	0	0	0
80	0.10376	0.015005248	0.121727414	-0.017967414
465	0.08904	0.125921888	0.078201073	0.010838927
900	0.15649	0.025170952	0.073836053	0.082653947
1830	0.14594	0.008238746	0.096998338	0.048941662
2710	0.14471	0.004701472	0.108248238	0.036461762
3600	0.1637	0.027970552	0.111338704	0.052361296
14400	0.16191	0.014690836	0.050629848	0.111280152
86400	0.48589	0.160675607	0.088684176	0.397205824
1 µM				
Time (sec)	**Fraction 1° Replaced**	**Standard Error**	**Control Replaced**	**Fraction 1° Displaced by Competition**
0	0	0	0	0
60	0.12211	0.078584651	0.121727414	0.000382586
420	0.11259	0.04178086	0.078201073	0.034388927
900	0.17359	0.066873185	0.073836053	0.099753947
1800	0.21391	0.114507029	0.096998338	0.116911662
2700	0.2225	0.105538386	0.108248238	0.114251762
3600	0.20019	0.038847694	0.111338704	0.088851296
14400	0.28154	0.139867793	0.050629848	0.230910152
86400	0.60973	0.096556979	0.088684176	0.521045824
10 µM				
Time (sec)	**Fraction 1° Replaced**	**Standard Error**	**Control Replaced**	**Fraction 1° Displaced by Competition**
0	0	0	0	0
60	0.6542	0.123739921	0.121727414	0.532472586
420	0.68452	0.103304632	0.078201073	0.606318927
900	0.7269	0.130120612	0.073836053	0.653063947
1800	0.76135	0.105075063	0.096998338	0.664351662
2700	0.82074	0.103696743	0.108248238	0.712491762
3600	0.83074	0.088976926	0.111338704	0.719401296
14400	0.85826	0.08346294	0.050629848	0.807630152
86400	0.9203	0.102990938	0.088684176	0.831615824

Table D.4: Kinetic analysis for **B14** secondary target at all concentrations tested.

B14 2° Target Analysis				
10 nM				
Time (sec)	**Fraction 1° Replaced**	**Standard Error**	**Control Replaced**	**Fraction 1° Displaced by Competition**
0	0	0	0	0
60	0.023215	0.005727547	0.121727414	-0.098512414
420	0.072757	0.013523715	0.078201073	-0.005444073
900	0.068741	0.021908882	0.073836053	-0.005095053
1800	0.076505	0.008830373	0.096998338	-0.020493338
2700	0.13138	0.1102107	0.108248238	0.023131762
3600	0.09257	0.119472395	0.111338704	-0.018768704
14400	0.2144	0.119056893	0.050629848	0.163770152
86400	0.37083	0.077023122	0.088684176	0.282145824
100 nM				
Time (sec)	**Fraction 1° Replaced**	**Standard Error**	**Control Replaced**	**Fraction 1° Displaced by Competition**
0	0	0	0	0
80	0.13438	0.003471868	0.121727414	0.012652586
465	0.32215	0.022830449	0.078201073	0.243948927
900	0.45445	0.094736675	0.073836053	0.380613947
1830	0.62079	0.086299932	0.096998338	0.523791662
2710	0.71698	0.1102107	0.108248238	0.608731762
3600	0.75312	0.119472395	0.111338704	0.641781296
14400	0.83548	0.119056893	0.050629848	0.784850152
86400	0.90058	0.077023122	0.088684176	0.811895824
1 µM				
Time (sec)	**Fraction 1° Replaced**	**Standard Error**	**Control Replaced**	**Fraction 1° Displaced by Competition**
0	0	0	0	0
60	0.58381	0.005727547	0.121727414	0.462082586
420	0.81807	0.013523715	0.078201073	0.739868927
900	0.86116	0.021908882	0.073836053	0.787323947
1800	0.87112	0.008830373	0.096998338	0.774121662
2700	0.88525	0.002702206	0.108248238	0.777001762
3600	0.88707	0.002902765	0.111338704	0.775731296
14400	0.90216	0.000784929	0.050629848	0.851530152
86400	0.94904	0.003742274	0.088684176	0.860355824
10 µM				
Time (sec)	**Fraction 1° Replaced**	**Standard Error**	**Control Replaced**	**Fraction 1° Displaced by Competition**
0	0	0	0	0
60	0.89289	0.013167828	0.121727414	0.771162586
420	0.89439	0.022842484	0.078201073	0.816188927
900	0.90306	0.010270901	0.073836053	0.829223947
1800	0.91033	0.016990274	0.096998338	0.813331662
2700	0.92404	0.00257779	0.108248238	0.815791762
3600	0.93695	0.021803672	0.111338704	0.825611296
14400	0.93853	0.015309156	0.050629848	0.887900152
86400	0.9654	0.038726635	0.088684176	0.876715824

Table D.5: Kinetic analysis for **B16** secondary target at all concentrations tested.

B16 2° Target Analysis				
10 nM				
Time (sec)	**Fraction 1° Replaced**	**Standard Error**	**Control Replaced**	**Fraction 1° Displaced by Competition**
0	0	0	0	0
60	0.163440817	0.014721927	0.121727414	0.041713403
420	0.352672612	0.061017452	0.078201073	0.274471539
900	0.463004955	0.013801165	0.073836053	0.389168903
1800	0.634231484	0.010962358	0.096998338	0.537233146
2700	0.673887379	0.012018727	0.108248238	0.565639141
3600	0.735220626	0.003982128	0.111338704	0.623881922
14400	0.831958661	0.011497777	0.050629848	0.781328813
86400	0.904889496	0.008487382	0.088684176	0.81620532
100 nM				
Time (sec)	**Fraction 1° Replaced**	**Standard Error**	**Control Replaced**	**Fraction 1° Displaced by Competition**
0	0	0	0	0
80	0.5529	0.034272187	0.121727414	0.431172586
465	0.75224	0.009682332	0.078201073	0.674038927
900	0.81617	0.028069403	0.073836053	0.742333947
1830	0.83186	0.034395732	0.096998338	0.734861662
2710	0.84634	0.03277898	0.108248238	0.738091762
3600	0.84994	0.034726805	0.111338704	0.738601296
14400	0.88296	0.011374264	0.050629848	0.832330152
86400	0.92652	0.022720578	0.088684176	0.837835824
1 µM				
Time (sec)	**Fraction 1° Replaced**	**Standard Error**	**Control Replaced**	**Fraction 1° Displaced by Competition**
0	0	0	0	0
60	0.59895	0.05907585	0.121727414	0.477222586
420	0.65276	0.031338945	0.078201073	0.574558927
900	0.64646	0.046100492	0.073836053	0.572623947
1800	0.66957	0.025074793	0.096998338	0.572571662
2700	0.68207	0.027771284	0.108248238	0.573821762
3600	0.69963	0.037677212	0.111338704	0.588291296
14400	0.73735	0.02317023	0.050629848	0.686720152
86400	0.83893	0.039800496	0.088684176	0.750245824
10 µM				
Time (sec)	**Fraction 1° Replaced**	**Standard Error**	**Control Replaced**	**Fraction 1° Displaced by Competition**
0	0	0	0	0
60	0.86954	0.065764163	0.121727414	0.747812586
420	0.88529	0.057924789	0.078201073	0.807088927
900	0.89081	0.055019459	0.073836053	0.816973947
1800	0.89842	0.049684479	0.096998338	0.801421662
2700	0.91092	0.04126007	0.108248238	0.802671762
3600	0.91517	0.039853067	0.111338704	0.803831296
14400	0.92718	0.052847262	0.050629848	0.876550152
86400	0.95687	0.032878636	0.088684176	0.868185824

APPENDIX E

REPLACEMENT RATE GRAPH FOR CASES WITH LOW RATES

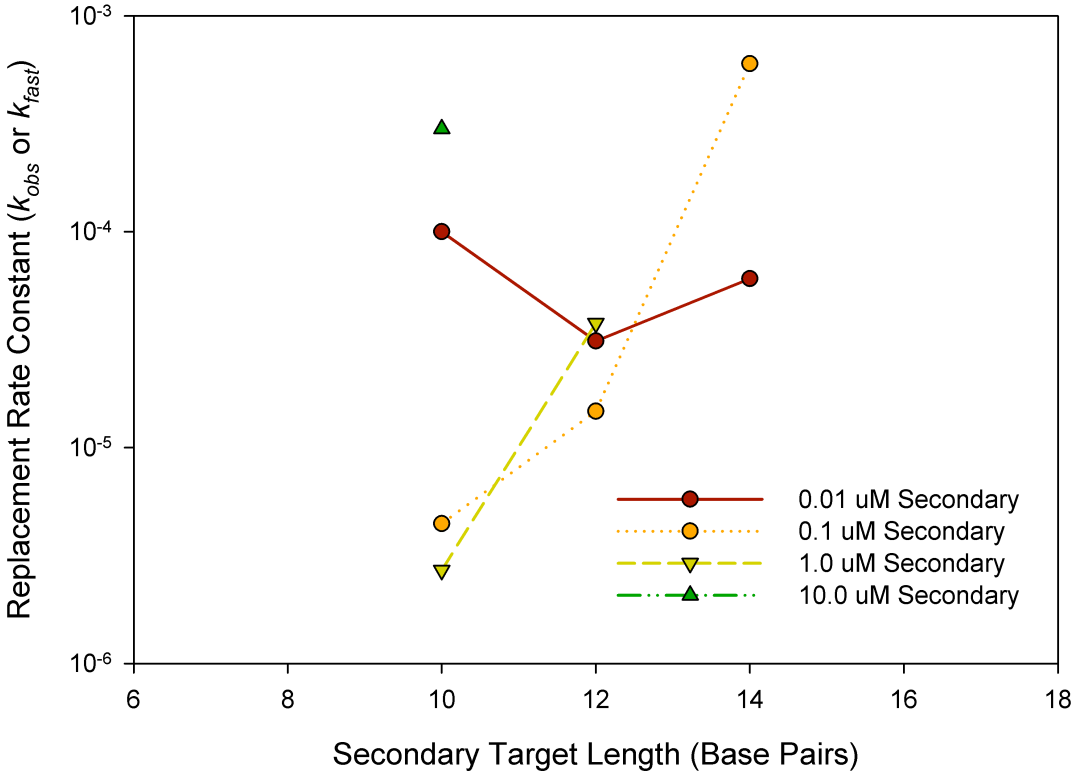

Figure E.1: Replacement rate constant as a function of secondary target length for cases in which the replacement rate, k_{obs}, is less than 10^{-3} s^{-1}.

Christopher Kirby Tison was born October 28, 1981 in Houston, Texas. He won first place in his fifth grade science fair studying the impact of charcoal selection on grilling temperature and time – his future path was set. He later received his B.S. in Materials Science & Engineering from the Georgia Institute of Technology in May 2004 and was a Grassman-Teague scholarship recipient during his undergraduate work. He participated in three years of undergraduate research in Dr. C.P. Wong's group studying polymers for microelectronics packaging. He received his Ph.D. in Materials Science & Engineering from the same Institution in May 2009 as a member of Dr. Valeria Milam's bioinspired colloidal assembly group. As a graduate student he was the recipient of a Boeing Scholarship and two years of funding through a Graduate Assistance in Areas of National Need (GAANN) Grant form Georgia Tech's Center for Drug Design, Development, and Delivery (CD4). His thesis work has been published in several top journals and been presented at over 20 conferences and workshops.

List of Publications

Tison, C.K. and Milam, V.T. *Reversing DNA-Mediated Adhesion at a Fixed Temperature.* Langmuir, **2007**. *23*. 9728-36.

Tison, C.K. and Milam, V.T. *Manipulating DNA Probe Presentation via Enzymatic Cleavage of Diluent Strands.* Biomacromolecules, **2008**. *9*. 2468-76.

Parpart, S.T., Tison, C.K. and Milam, V.T. *Effects of Mismatches on DNA as an Isothermal Assembly and Disassembly Tool*. **Submitted**.

Tison, C.K. and Milam, V.T. *Programming the Kinetics and Extent of Colloidal Disassembly Using a DNA Trigger*. **In preparation**.

Tison, C.K. and Milam, V.T. *Competitive Hybridization for Release of DNA-Linked, PEGylated Protective Coatings.* **In preparation**.